

2008

# Laser Sintering of Nanodiamond Powders on Aluminum Substrate

Rodger Vincent Blum  
*Iowa State University*

Follow this and additional works at: <https://lib.dr.iastate.edu/etd>

 Part of the [Mechanical Engineering Commons](#)

## Recommended Citation

Blum, Rodger Vincent, "Laser Sintering of Nanodiamond Powders on Aluminum Substrate" (2008). *Graduate Theses and Dissertations*. 10938.  
<https://lib.dr.iastate.edu/etd/10938>

This Thesis is brought to you for free and open access by the Iowa State University Capstones, Theses and Dissertations at Iowa State University Digital Repository. It has been accepted for inclusion in Graduate Theses and Dissertations by an authorized administrator of Iowa State University Digital Repository. For more information, please contact [digirep@iastate.edu](mailto:digirep@iastate.edu).

# **Laser sintering of nanodiamond powders on aluminum substrate**

by

**Rodger Vincent Blum**

A thesis submitted to the graduate faculty  
in partial fulfillment of the requirements for the degree of  
**MASTER OF SCIENCE**

Major: Mechanical Engineering

Program of Study Committee:

Pal Molian, Major Professor

Xinwei Wang

Matt Frank

Iowa State University

Ames, Iowa

2008

Copyright © Rodger Vincent Blum, 2008. All rights reserved.

### Dedication

*I dedicate this thesis to my loving parents without their love, and encouragement I would not have made it this far, and to my loving fiancé whom without knowing, keeps me striving to be my best.*

## TABLE OF CONTENTS

<b>LIST OF FIGURES</b>	iv
<b>LIST OF TABLES</b>	ix
<b>ACKNOWLEDGEMENTS</b>	x
<b>CHAPTER 1. Introduction</b>	1
<b>CHAPTER 2. Laser Sintering of Nanodiamond Coatings on Aluminum A319 using a Focused Beam</b>	3
Abstract	3
Introduction	4
Experimental Details	7
Results and Discussion	17
Conclusion	37
Acknowledgements	37
References	38
<b>CHAPTER 3. Synthesis of Nanodiamond Coatings on Aluminum Substrates Using Ring Beam-Configured Laser Sintering</b>	40
Abstract	40
Introduction	41
Experimental Details	44
Results and Discussion	53
Conclusion	75
Acknowledgements	76
References	76
<b>CHAPTER 4. General Conclusions and Future Work</b>	79

## LIST OF FIGURES

Figure 2.1	TEM micrographs of the as-received diamond powder at different magnifications showing the rounded nature of the particles	8
Figure 2.2	Permanent mold casting of A319 rods	9
Figure 2.3	Schematic of the electrostatic spray coating	11
Figure 2.4	Schematic of the laser sintering setup	12
Figure 2.5	Load curve used to flatten surface before making nanoindentation	14
Figure 2.6	(Left) Ball-on-disc friction and wear setup (Right) Close up of the setup near the sample	16
Figure 2.7	Raman spectra of laser-sintered diamond coating; (Top Line) After cleaning (Bottom Line) Before cleaning	18
Figure 2.8	a) Raman spectrum of raw ND powder; b) Raman spectra of coupons processed at 200 W; c) Raman spectra of coupons processed at 1000 W	19
Figure 2.9	Digital photograph of optimally laser-sintered coupon	21
Figure 2.10	Raman spectra of optimally laser-sintered coupon (200 W, 85 mm/s)	22
Figure 2.11	SEM micrographs. a) and b) Electrostatically spray coated coupon; c) Secondary electron image of laser-sintered coupon; d) Backscattered image of laser-sintered coupon	23

Figure 2.12	EDX analysis of (Top) Electrostatically spray coated coupon, (Bottom) Laser-sintered coupon	24
Figure 2.13	SEM image of the transverse section of laser-sintered coupon showing the coating	25
Figure 2.14	Optical images with roughness profiles: a) Bare aluminum surface b) Electrostatically spray coated surface c) Laser sintered surface with (Top) Roughness plot along one of the peaks (Bottom) Roughness plot along one of the valleys	28
Figure 2.15	Chart comparing the different coupons by their surface roughness	29
Figure 2.16	a) (Left) Unacceptable force plot due to surface breakage b) (Right) Example of an acceptable force plot. Both plots are from the optimally laser-sintered coupon	30
Figure 2.17	AFM image of one indentation made on the laser-sintered coupon	31
Figure 2.18	Distribution of nanoindentation values	32
Figure 2.19	Distribution of Young's modulus values	32
Figure 2.20	Friction of 319 aluminum substrate against 440C steel	33
Figure 21	Friction of laser-sintered coupon against 440C steel. (Top) 0-2 minutes (Bottom) 2-5 minutes	34
Figure 2.22	Wear track profile of 319 aluminum substrate against 440C steel	35
Figure 2.23	Wear track of laser sintered aluminum against 440C steel	35

Figure 2.24	Optical micrograph of wear tracks at 50x magnification (Left) Bare aluminum (Right) Laser-sintered coupon	36
Figure 2.25	SEM images of wear tracks on the optimally laser-sintered coupon	36
Figure 2.26	EDX analysis of wear track on optimally laser-sintered coupon showing that there is no iron meaning that particles from the steel ball used in the test did not transfer to the coupon	37
Figure 3.1	TEM image and X-ray diffraction pattern of nanodiamond powder	45
Figure 3.2	Schematic of the laser sintering setup	46
Figure 3.3	Axicon and plano-convex lens combination to produce ring beam	48
Figure 3.4	Load curve used to flatten surface before making indentation	51
Figure 3.5	(Left) Ball-on-disc tribometer; (Right) Close up of the test setup	52
Figure 3.6	Typical Raman spectra of a laser parameter before (bottom line) and after (top line) cleaning	54
Figure 3.7	Raman spectrum of ND powder used in this work	55
Figure 3.8	Raman spectra of coupons processed at 1000 W	56
Figure 3.9	Photograph of laser-sintered coupon (single laser pass in the middle of sample)	57

Figure 3.10	Raman spectra of optimally laser-sintered coupon (1000 W, 4.2 mm/s)	58
Figure 3.11	Phase diagram of ultra- fine carbon	60
Figure 3.12	SEM micrographs of ND coated A319 coupons: a) and b) electrostatically spray coated; c) and d) laser-sintered	62
Figure 3.13	EDX analysis: (Top) electrostatically spray coated coupon; (Bottom) laser-sintered coupon	63
Figure 3.14	SEM image of the transverse section of laser-sintered coupon	64
Figure 3.15	XRD pattern of the laser-sintered coupon	64
Figure 3.16	Optical image and roughness profile of: a) and b) bare aluminum surface c) and d): electrostatically spray coating, and e) and f) laser sintered coating	66
Figure 3.17	Comparison of surface roughness	67
Figure 3.18	a) (Left) Bad force plot due to surface breakage b) (Right) Example of an acceptable force plot. Both plots are from the laser-sintered coupon	68
Figure 3.19	AFM image of nanoindentation on the laser-sintered coupon	68
Figure 3.20	Distribution of nanohardness values in laser-sintered coupon	69
Figure 3.21	Distribution of Young's modulus values in laser-sintered coupon	69
Figure 3.22	Friction of 319 aluminum substrate against 440C steel	70
Figure 3.23	Friction of laser-sintered coupon against 440C steel	70
Figure 3.24	Wear track profile of 319 aluminum substrate against 440C steel	72

Figure 3.25	Wear track of laser-sintered aluminum against 440C steel	73
Figure 3.26	Optical micrographs of wear tracks at 50x magnification (Left) Bare aluminum (Right) Laser-sintered coupon	74
Figure 3.27	SEM images (backscattered and secondary electron) of wear track of laser-sintered coupon	74
Figure 3.28	EDX analysis of wear track of laser-sintered coupon showing that there is no iron meaning that particles from the steel ball did not transfer to the coupon	75

## LIST OF TABLES

Table 2.1	Characteristics of nanodiamond powder used in this work	8
Table 2.2	Nominal composition of alloy 319 used in this work	9
Table 2.3	Test matrix parameters for the focused beam (0.2 mm diameter) experiments	12
Table 2.4	Carbon phase and corresponding Raman peaks [27]	15
Table 2.5	Test conditions for the friction and wear test	16
Table 2.6	Table comparing the coefficient of friction and wear rate of the optimally laser-sintered coupon and the bare aluminum substrate	34
Table 3.1	Nominal composition of alloy 319 used in this work	44
Table 3.2	Characteristics of nanodiamond powder produced by shock explosion	45
Table 3.3	Laser sintering test parameters	47
Table 3.4	Carbon phase and corresponding Raman peaks [27]	50
Table 3.5	Test conditions for the friction and wear test	52
Table 3.6	Aluminum's thermal Properties and laser parameters	59
Table 3.7	Comparison of coefficient of friction and wear rate	70

## ACKNOWLEDGEMENTS

I would like to thank my major professor, Dr. Molian, and Dr. Nair for allowing me the opportunity to work with them on this research project. I appreciate Dr. Molian's support and guidance in completing this thesis. It has been an honor working with Dr. Molian. I would also like to thank Dr. Wang, and Dr. Frank for accepting to serve on my committee.

Special thanks to Dr. Wenping Jiang and Larry Couture for their help in material preparation; Hal Sailsbury, Dr. Warren Straszheim, Vitalli Brand, and In-Seok Seo for their assistance in material characterization. I would also like to thank the other various lab technicians that assisted me with my research. Most of all, I thank my family and friends for their thoughts and support.

## CHAPTER 1. Introduction

The purpose of this research is to develop 10-50  $\mu\text{m}$  thick, strongly adherent nanodiamond/diamond-like carbon (ND-DLC) coatings on aluminum substrates using a novel laser sintering process and demonstrate their tribological properties including hardness, toughness, wear resistance and friction relevant to engine applications. Aluminum is in demand for many engine applications due to its low density and high corrosion resistance. However, due to its low wear resistance, the number of applications are limited. It is hoped that ND-DLC coatings will greatly improve the performance and durability of aluminum engine components by reducing the friction between parts and improving the wear and scuffing resistance of the aluminum substrate. The success of this research will assist in improving the fuel efficiency of all automobiles particularly in a time of rising fuel prices. In another area, the laser sintering of ND particles could be extended to other substrates, such as titanium; this would be beneficial in the medical field, especially in biomedical implants. It could be used on surgical prostheses to prolong the current 10-15 year lifespan of the implant.

### Thesis Organization

This thesis is organized into two papers and an appendix. Chapter 2 describes the first paper, submitted to *Surface and Coatings Technology*, which examines the traditional laser sintering of nanodiamond particles on aluminum substrate. In this paper, a round laser beam was used to produce a composite layer of nanodiamond/diamond-like carbon/aluminum on the aluminum substrate. Chapter 3 describes a unique technique of laser sintering that is in the patent application process. This paper discusses the use of a ring-beam configured laser beam to produce a composite layer of nanodiamond and

amorphous carbon on the aluminum substrate. Chapter 4 summarizes the general conclusions drawn from this research and provides recommendations for future work.

Appendix A shows a thermal model for the ring-beam configured laser sintering process.

## **CHAPTER 2. Laser Sintering of Nanodiamond Coatings on Aluminum A319 using a Focused Beam**

Paper submitted to Surface and Coating Technology, 2008

Rodger Blum and Pal Molian

### **Abstract**

Laser-induced phase transition and sintering of nanodiamond (ND) powders (4-8 nm) was used to produce 50-75  $\mu\text{m}$  thick, strongly adherent composite coatings of nanodiamond, amorphous carbon and aluminum on cast alloy A319. First, ND powders, produced by detonation synthesis, were electrostatically sprayed on the surfaces of aluminum substrates. Second, a continuous wave  $\text{CO}_2$  laser was used to heat the ND powder and aluminum substrate in a controlled fashion to cause liquid-phase nano-sintering that led to a dispersion and phase transformation of ND particles in a molten pool of aluminum. Raman spectroscopy, scanning electron microscopy, optical profilometry, and microhardness, nanoindentation and friction/wear tests were used to evaluate the coating characteristics. Results indicate that the optimum laser parameters were laser power of 200 W, beam travel speed of 85 mm/s, and spot diameter of 0.2 mm. The coatings consisted of peaks and valleys with a surface roughness of about 5  $\mu\text{m}$  Ra. The peaks are amorphous carbon and graphite while the valleys are primarily resolidified aluminum. Microhardness and nanoindentation revealed a hardness varying widely from 200 MPa to 23 GPa. Tribology tests showed that the coefficient of friction was under 0.2 in the beginning and then increased to an average value of 0.39. By comparison, the uncoated substrate exhibited a much higher friction (up to 1.03) despite having the finer surface (1.8  $\mu\text{m}$  Ra). Wear loss is also reduced by over 500% in the laser-sintered

coupon compared to the uncoated aluminum. The potential application of the work is hard and wear resistant coatings for lightweight engine components and biomedical implants to improve the tribological characteristics.

**Keywords:** nanocoatings, diamond, tribology, laser sintering

## 1 Introduction

Fuel economy in automobiles can be significantly improved by reducing the frictional energy loss and using lightweight alloys in engine components. Friction accounts for 15% of the available energy in the fuel [1] and the majority of such friction loss occurs in the reciprocating motion of piston ring in cylinder bore [2]. Under harsh operating conditions such as start-up, steep hill driving and cold weather, lubrication becomes ineffective and scuffing wear occurs significantly. In order to improve the fuel economy, aluminum alloy was substituted for cast iron but the former exhibits poor tribological properties. Often a cast iron liner is used to protect the aluminum cylinder bore. Alternatively, various coating approaches including anodizing, Cr-electroplating, Ni-P electroless plating, sputtering, chemical vapor deposition (CVD) and laser alloying/cladding have been used to improve the friction and wear properties of aluminum alloys [3-11]. Anodizing produces an oxide layer at ambient temperature with hardness close to that of high strength steels but the porosity content can be high as much as 50%. In addition, the coating brittleness and the cracks induced during the process strongly affect the fatigue performance. Furthermore, the low pH-acidic electrolytes used in the process do not meet the environmental regulations. Cr and Ni-P plating processes

suffer from similar problems. Recent innovation in aluminum coating is a controlled oxidation process, designated as microplasmic anodizing, which offers the benefits of environmental benign due to increased pH, less porosity, increased density and much improved hardness of around 1300 kg/mm<sup>2</sup> [3]. However, studies of micro-arc oxidized aluminum alloys have shown that as-deposited and polished alumina coatings have a relatively high friction coefficient >0.7 [4]. A variety of PVD and CVD coatings such as TiN have been applied to aluminum to improve its tribological properties [5, 6]. However, the thinness of coating and thermal/mechanical mismatch of the coating with the substrate did not allow adequate load support in service [7]. Laser surface cladding and alloying of aluminum alloys using different metals and ceramics have shown various degrees of improvements on the surface hardness and wear-resistant properties [8-11].

Diamond-like carbon (DLC) is emerging as ultra-hard, lubricious coating for improving the overall performance of power train components and piston-bore assembly [12-16]. For example, DLC coatings on piston rings significantly reduced the friction energy loss (thus fuel consumption) and increased life and reliability of the engine [12]. Due to inadequate wear resistance and low seizure loads of aluminum, DLC serves to minimize wear, decrease friction, reduce energy consumption, improve fuel efficiency, reduce CO<sub>2</sub> emission and increase acceleration particularly when compared against anodic and plated coatings [13-15]. Quantitatively the following were achieved: ten times longer component service life, five percent greater engine output, four percent lower fuel consumption, three times more stress resistance of transmission surfaces, and nearly 50% lower manufacturing cost [16]. Two problems are confronted with DLC coating when it was applied on aluminum. One is the limited coating thickness (<10 μm)

while the other is thermal expansion mismatch causing poor adherence. We present here a novel method of laser sintering of nanodiamond (ND) powders on aluminum to overcome the above problems while creating a composite coating of ND, DLC and aluminum.

Nanodiamond, also known as ultra-dispersed or nanocrystalline diamond, is emerging as a potential material for tribological applications. Like single and polycrystalline counterparts, NDs have superior hardness, wear resistance, and thermal conductivity. The key benefit of NDs is that they have an increased surface-to-volume ratio which makes them exhibit higher surface reactivity and thereby allows sintering to take place at much lower temperatures. ND powders of 4-8 nm are generally produced by shock detonation synthesis using carbon containing explosives like trinitrotoluene (TNT). In the detonation synthesis process, powerful explosives are mixed with the  $C_aH_bN_cO_d$  in a non-oxidizing medium to yield a condensed carbon phase that consists of ND particles [17]. The result of this process is a ND powder that has 75% purity. A cleaning process is then applied to remove most of the impurities. ND powders are now being commercially produced across the world; these powders are used in various applications including abrasives for the optical and semiconductor industries, durable and hard coatings, polymer reinforcements, lubricant additives for engines and other moving parts, protein absorbent and even medicinal drugs [17-20].

Conventional thermal sintering of ND powders at high temperatures and pressures (1473-2073 K, 2-8 GPa) produced porous diamond structures [21-24]. It is limited to producing small samples and not cost effective. Another technique for creating a ND sample is plasma pressure compaction where the ND powder is subjected to lower

temperatures and pressures (973 K to 1473K, 65 MPa) [25]. The sintered ND pellets contained 50% porosity (density 1.3-1.6 g/cm<sup>3</sup>) and some graphite. The best sintered ND sample, processed at 1173 K, possessed a hardness of 0.2 GPa and a Young's Modulus of 5.5 GPa [25]. It has a structure consisting of graphite linking diamond particles into larger agglomerates. Pressures below 65 MPa are expected to cause excessive phase transformation of diamond to graphite [26, 27]. This process could be used to infiltrate other materials to ND compacts.

In this work, we have developed a novel CO<sub>2</sub> laser sintering technique to achieve ND composite coatings on A319 because ND powders provide active surfaces and enable laser energy absorption and low temperature sintering. Aluminum 319 is a widely-used cast alloy in the production of automotive components due to its excellent mechanical properties and good castability characteristics [28]. Laser sintering technique is the continuous rastering of the laser beam on the sample surface and is widely used for many rapid prototyping processes including selective laser sintering (SLS) [29, 30]. It is based on the principle of layer-by-layer to create parts. The layer of powder can be as thin as the particle size of the powder being used. In our experiments, laser sintering was used to bond a thick (25-35 μm) layer of ND powder to an aluminum substrate.

## 2 Experimental Details

### 2.1 Nanodiamond Powder

The commercially available ND powder used in this experiment was acquired from SPE SINTA Ltd. in Kharkiv, Ukraine. The ND powders have typically a particle size of 4-8 nm encapsulated by fullerene-like carbon shells and aggregated into 20-50 nm particles [31]. The surface is usually covered by various functional groups such as –

COOH,  $-CH_2$ , and  $-OH$  [31]. The ability to control the surface of the ND particles is governing criterion. Table 1 shows the characteristics of ND powder used in this work. Figure 1 shows TEM micrographs of the ND powder that portray the roundness and uniformity of the particles.

Table 1: Characteristics of nanodiamond powder used in this work

External kind	Powder of gray color
Moisture quantity, % not more	0.5
Average size of prime particles (coherent scattering region), nm	2-8
Specific surface, $m^2/g$	250
Density, $kg/m^3$	3000.0
Quantity of metallic impurities, % not more	2.0
Quantity of carbon cubic phase, % not less	90
Quantity of impurity additives, % not more	2.0

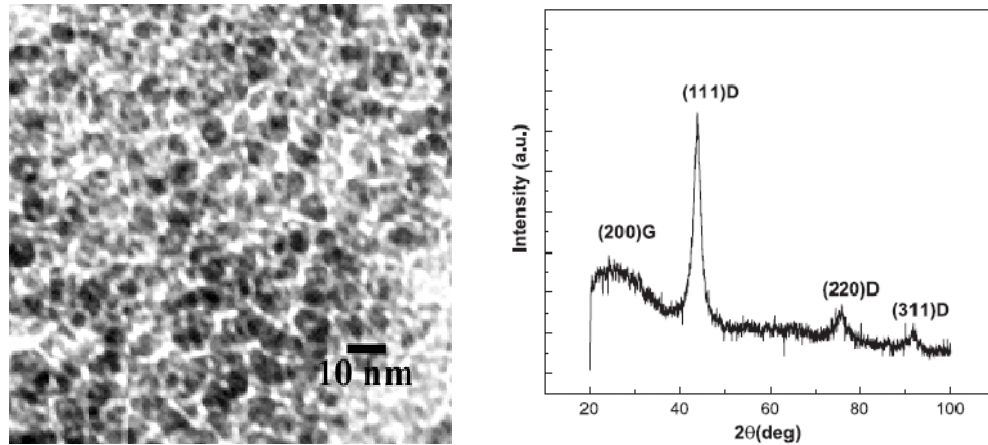


Figure 1: TEM image and X-ray diffraction pattern of nanodiamond powder

## 2.2 Aluminum Coupon Preparation

A319-T6, a precipitation hardened Aluminum-Silicon-Copper alloy, was used as the substrate material. The 25 lb cast ingot of aluminum A319 with a nominal composition shown in Table 2 was acquired from Custom Alloy Light Metals, City of Industry, CA.

Table 2: Nominal composition of alloy 319 used in this work

Element	Si	Fe	Cu	Mn	Mg	Cr	Zn	Ti	Sn	Pb	Ni	Al
Weight Percent	5.860	0.678	3.519	0.246	0.056	0.104	0.901	0.160	0.021	0.032	0.121	87.80

The A319 ingot was then cut into smaller pieces using an industrial band saw, and then these pieces were melted in an electric induction furnace at 1673 K. Permanent mold casting (shown in Figure 2) was then carried out as follows. Two hollow 1020 steel half-pipes were clamped together to make a 25 mm inner diameter hollow pipe, sprayed on the inside with a graphite based non-stick lubricant and then the whole assembly was submerged in a box filled with river sand while the top part of the pipe sticking out. Molten aluminum 319 alloy was poured into the hollow cavity and allowed to cool. The clamps were separated and the two half-pipes were taken apart to reveal a rod of 25 mm (~1") diameter x 250 mm long (~10"). Four A319 rods were produced by this method.

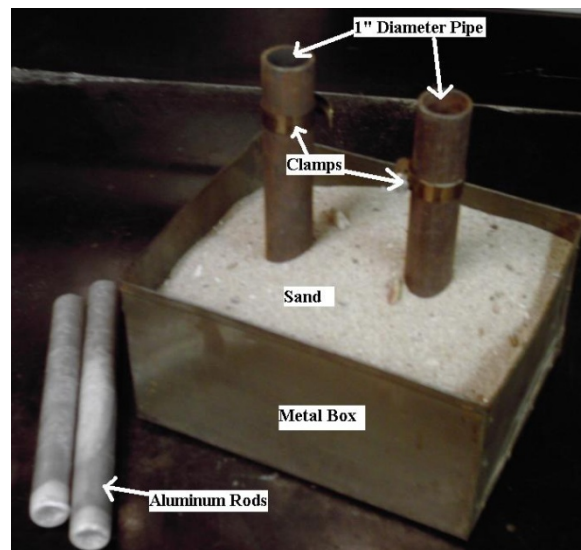


Figure 2: Permanent mold casting of A319 rods

The aluminum cast rods were then heat treated (T6 temper) to cause precipitation hardening. T6 has a higher yield strength (27 ksi to 14 ksi) and ultimate strength (34 ksi to 28 ksi) than as-cast aluminum 319 [32]. The steps involved in the heat treatment are as follows. First, solution heat treatment was carried out by placing the sample in an electric furnace (Lindberg Furnace) at 1208-1218 K for 8 hours and then water quenched. The sample was then artificially aged at 578-588 K for 5 hours. Following the heat treatment, the aluminum was cut into 25 mm diameter, 3.2 mm thickness coupons using an abrasive saw flooded with water. In order to improve the surface finish of the coupon, a Clemco Industries Dry Blast Cabinet with Dust Collector (Model ACDFM) was used to sandblast the surfaces. The sample surfaces were then thoroughly cleaned using acetone to remove any impurities and surface deposits.

### **2.3 Electrostatic Spray Deposition**

ND powder was loosely deposited on the surface of aluminum coupon using a home-built corona-charging based, electrostatic spray gun (Figure 3). The powder was first negatively charged and then allowed to follow the electric field lines toward the grounded substrate (aluminum), forming a uniform coating. The coating is adhered to the substrate by weak electrostatic forces. Since the size of the diamond particles is on the order of nanometers, agglomeration of these particles is a potential issue that has to be overcome to achieve nanoparticle deposition. To prevent agglomeration of the particles, a jet mill was integrated into the electrostatic spray coating setup (the setup without the jet mill is shown in Figure 3). A jet mill is a system that circulates particles through a chamber at high velocity causing collisions between the particles thus keeping the particles from agglomeration. Besides the physical properties of the powder (particle

density, particle shape, average particle size, particle size distribution, and dielectric properties), process parameters including electrode-substrate distance, voltage applied at the electrode, and air pressure were optimized to produce a coating of 25-35  $\mu\text{m}$  thickness.

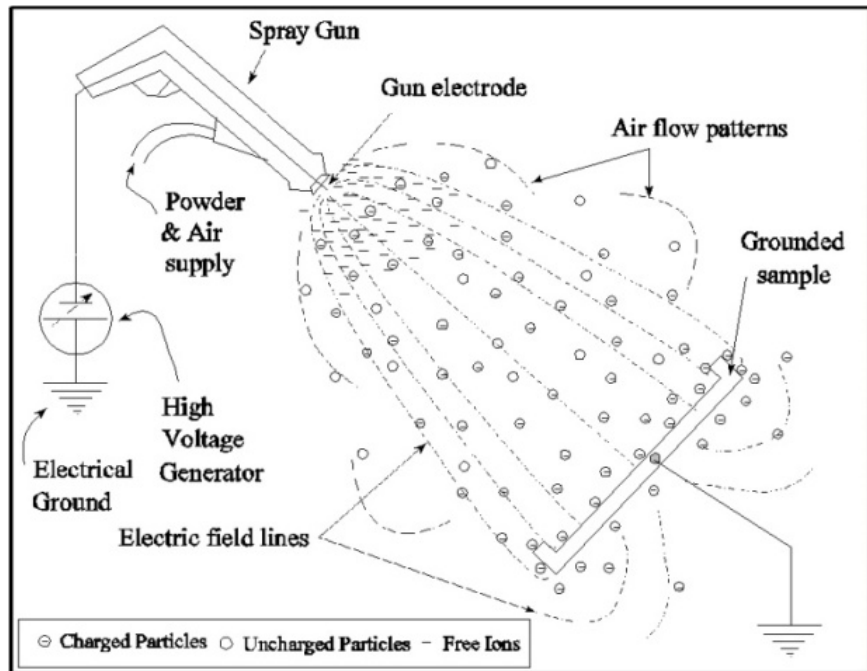


Figure 3: Schematic of the electrostatic spray coating [33]

## 2.4 Laser Sintering Process

A 1.5 kW continuous wave CO<sub>2</sub> laser (Spectra Physics Model 820) of 10.6  $\mu\text{m}$  wavelength with CNC-controlled worktable was used. Figure 4 shows a schematic of laser sintering setup. A standard 127 mm (5 in) focal length, plano-convex lens was used to focus the beam to a spot size of 0.2 mm. Argon gas at a flow rate of  $2.3 \times 10^{-2} \text{ m}^3/\text{s}$  (50 ft<sup>3</sup>/min) was used as an assist gas. The coupons were held in place by a vice clamped on to the CNC controlled worktable. Single-pass laser treatments were ran using a matrix

of parameters shown in Table 3. Multi-pass laser treatment was also performed to cover the entire surface of the coupon using optimized laser parameters (200 W, 85 mm/s) with an overlap of 5%.

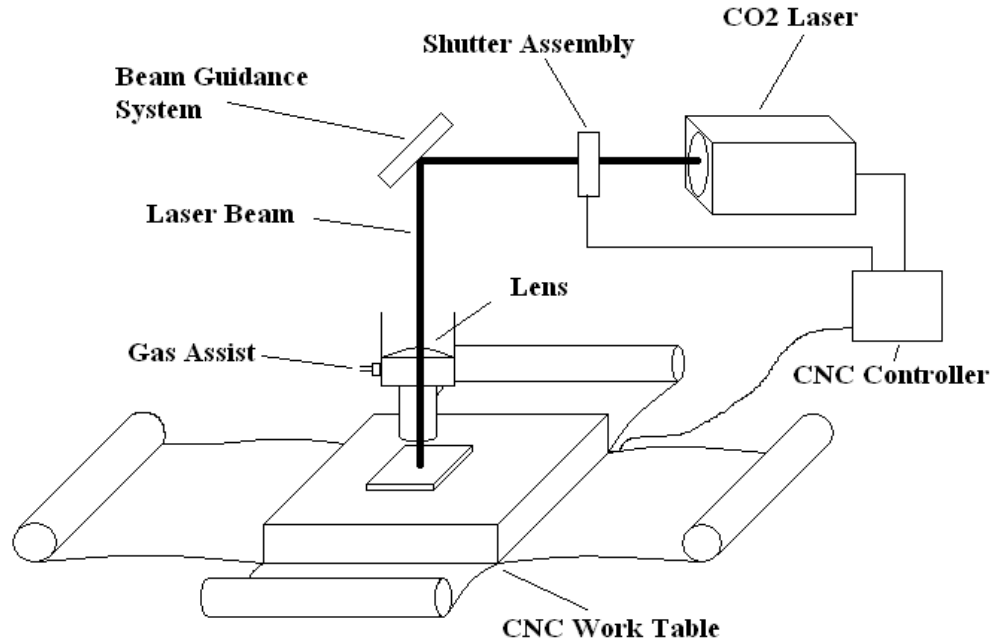


Figure 4: Schematic of the laser sintering setup

Table 3: Test matrix parameters for the focused beam (0.2 mm diameter) experiments

Test Run	Power (W)	Speed (mm/s)
1	200	42.33
2	200	84.67
3	200	169.33
4	200	254
5	1000	254
6	1000	169.33
7	1000	84.67
8	1000	42.33

## 2.5 Characterization and Analysis

The following tests were performed to determine the mechanical and tribological properties of the coatings: Raman spectroscopy using a Renishaw inVia Raman

Microscope (488 nm), thickness and quality using metallography and scanning electron microscope (JEOL JSM-840A), Vickers microhardness using a Wilson Tukon Microhardness Tester (Model 200), nanoindentation using a Hysitron TriboIndenter, surface roughness using a Zygo New View 6k Optical Profilometer and friction and wear using a ball-on-disc tribometer.

The coupon was metallographically prepared by first mounting in Bakelite to help preserve the coating and then sectioning it using a thin saw. The two halves were then polished using a sequence of abrasive papers with grits of 240, 320, 400, 600, 1000, 1200, and then finish polished using 6  $\mu\text{m}$  and 1  $\mu\text{m}$  diamond pastes. The coupons were rinsed in alcohol, dried and then etched using Kroll's reagent (6 ml  $\text{HNO}_3$ , 2 ml HF, 92 ml  $\text{H}_2\text{O}$ ).

In Vickers microhardness tests, a diamond pyramid indenter with a range of loads, usually 10 g to 1 kg, was utilized. However the indentation should be made as large as possible to increase the measurement resolution. Another aspect that yields a better measurement resolution is having a sample with a fairly smooth surface [34]. In this experiment hardness measurements were completed using a 25 gram which is appropriate for thin superficial layers. The Vickers hardness of heat treated aluminum 319 is known to be around 113  $\text{kg}/\text{mm}^2$  (1.13GPa) at ambient temperature [35] and was confirmed in the present work.

Nanoindentation is a recent method of characterization that can measure mechanical properties of nanoscale features. In this test, indentation depth and area are measured using a Hysitron TriboIndenter with Berkovich tip of radius 564.2 nm and are used to calculate the hardness and Young's Modulus of the coating. During this

procedure, the tip is usually driven into the material until a maximum predetermined force is reached, then held for a few seconds, and finally unloaded. However, in this effort, the load was applied, unloaded, applied again, held, and finally unloaded. This was done to help flatten the surface before actually making the indentation. Figure 5 shows the load curve used.

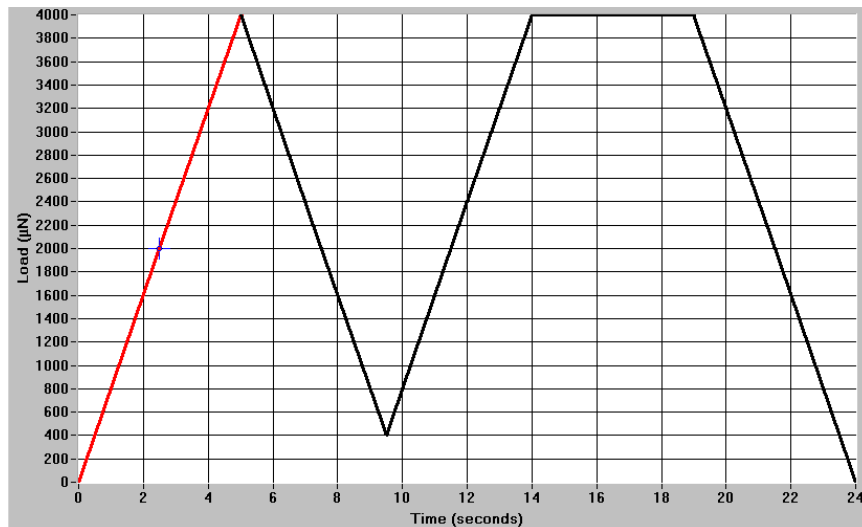


Figure 5: Load curve used to flatten surface before making nanoindentation

Optical profilometer is a non-contact method of finding surface roughness while providing three-dimensional topography measurements and optical images of the surface. It is capable of giving the PV (peak to valley) distance, the Ra (arithmetic average) deviation from the center line, and rms (root-mean-square) deviation from the center line.

Raman spectroscopy relies on the scattering of monochromatic light usually from a laser in the visible, infrared, or ultraviolet range. The energy difference in the scattered light is then measured as the signature of the material, thus allowing Raman spectroscopy to discriminate the different carbon phases. These carbon phases will yield different Raman peaks seen in Table 4. Single crystal diamond will give a definite peak at  $1332\text{ cm}^{-1}$  while ND will yield a peak at  $1325\text{ cm}^{-1}$  [36]. Graphite will yield a definite peak at

1580  $\text{cm}^{-1}$ , while DLC can yield a range of peaks but the main peak is at 1355  $\text{cm}^{-1}$  [37].

Thus Raman data was obtained through the range of 1200-1800  $\text{cm}^{-1}$ .

Table 4: Carbon phase and corresponding Raman peaks[37]

Phase	Raman Peak ( $\text{cm}^{-1}$ )
Single Crystal Diamond	1332
Nanodiamond	1325
Diamond-like Carbon	1350
Amorphous Carbon	1350-1450
Onion-like carbon	1572
Graphite	1580

Ball-on-disc test for evaluating friction and wear is shown in Figure 6. Test conditions are listed in Table 5. In these tests, a ball shaped indenter is loaded onto the sample with a known force. The ball is mounted to a stiff lever that is designed to be a frictionless force transducer. The sample is then rotated at a certain speed. During this test, the frictional forces between the ball indenter and sample are measured by the very small deflections of the lever using an LVDT sensor. The wear coefficients for the ball and sample are then calculated from the volume of material lost during the test using the following equation:

$$k = \frac{V}{F * s}$$

where  $k$  is the wear rate coefficient,  $V$  is the volume of material lost,  $F$  is the normal load, and  $s$  is the sliding distance. The units for the wear coefficient are  $\text{mm}^3/\text{Nm}$ .

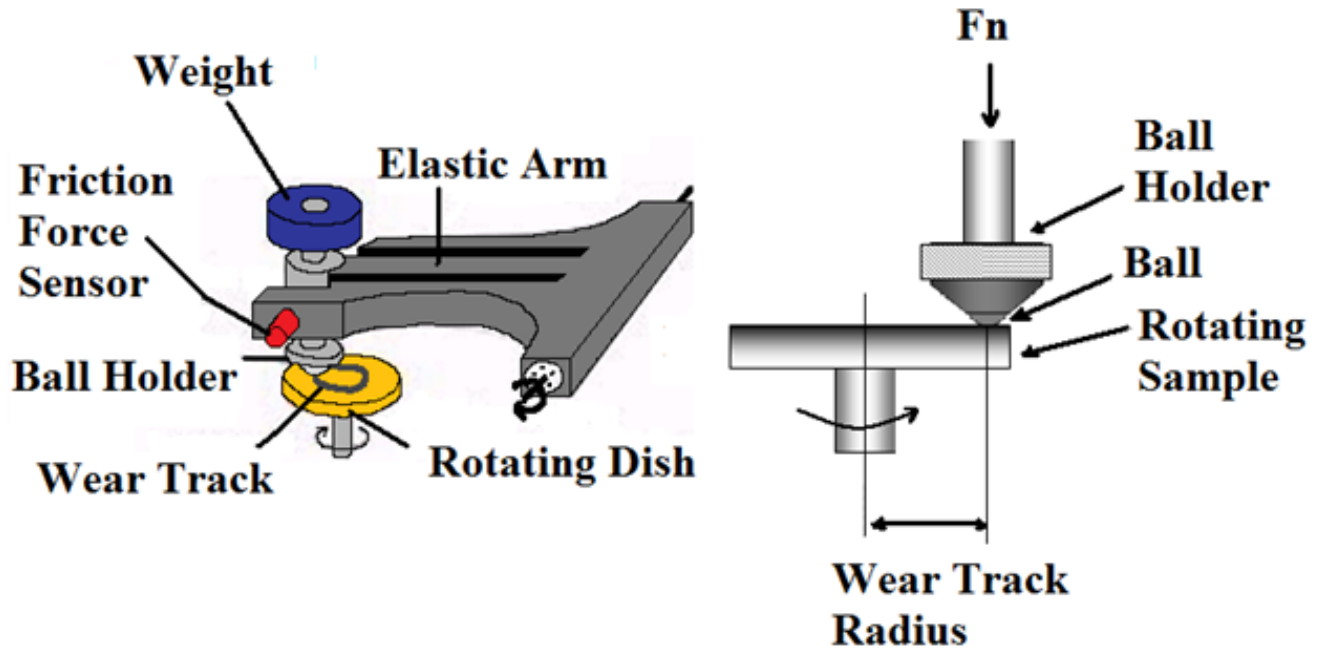


Figure 6: (Left) Ball-on-disc friction and wear setup (Right) Close up of the setup near the sample

Table 5: Test conditions for the friction and wear test

Load	5.0 N
Length of test	5 min
Rate	50 rpm
Radius of track	2.5 mm
Sliding velocity	13.1 mm/s
Sliding distance	1.57 m
Revolutions	250
Lubricant	None
Atmosphere	Air
Temperature	296 K (room temperature)
Humidity	35%
Ball diameter	6 mm
Ball material	Stainless steel 440C

### 3 Results and Discussion

#### 3.1 Effects of Laser Parameters

Laser power in the range 200 W-1000 W was studied. Powers less than 200 W did not provide adequate heat to sinter the ND powder on aluminum substrate while powers at and above 1000 W with varying speeds caused vaporization of the powder and practically cut the aluminum substrate. The change in speed from 42 mm/s to 254 mm/s at 1000 W only decreased the depth of the groove. The optimum power for liquid-phase sintering was found to be 200 W based on the criteria of minimal vaporization and relatively smooth surface. Vickers microhardness test data was used to determine the effect of laser beam travel speed at 200 W but the surface roughness of the sintered coupon made it difficult to get accurate hardness readings. Therefore we decided to use Raman spectroscopy to compare the effect of the parameters.

#### 3.2 Raman Spectroscopy

A black residue on the surfaces of many samples was noted and that residue could be easily removed by blowing off the surface. The black residue is believed to be a layer of soot that has formed in the sintering process. Since this layer of loose carbon could mask the Raman spectra, an ultrasonic cleaning step consisting of immersing the coupon in a deionized water bath for 3 minutes was employed to remove the layer. A comparison of the Raman spectra before and after cleaning (Figure 7) showed that the peaks are more intense for the cleaned coupon.

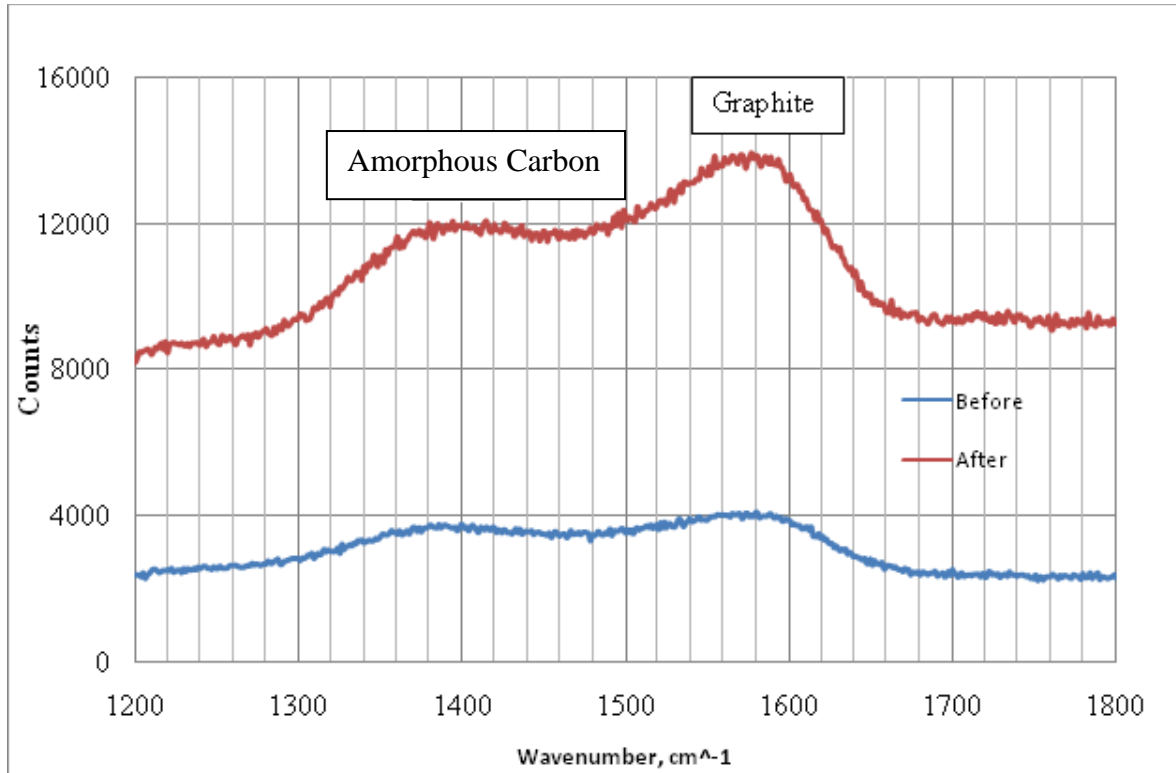


Figure 7: Raman spectra of laser-sintered diamond coating; (Top Line) After cleaning (Bottom Line) Before cleaning

Figure 8a is a Raman spectrum of the raw ND powder that shows a sloping upward line with a diamond peak at  $1325\text{ cm}^{-1}$ ; this is surprising because the impurities and graphite-like  $\text{sp}^2$  bonded carbon often drowns out the diamond-like  $\text{sp}^3$  bonded carbon [36, 37]. Studies have demonstrated the presence of a diamond peak in ND powder using the 488 nm wavelength [37]. Figure 8b and 8c shows the Raman spectra of the coupons processed at 200 W and 1000 W respectively and subsequent ultrasonic cleaning. No diamond peaks corresponding to  $1332\text{ cm}^{-1}$  are seen but it could just be masked by the  $\text{sp}^2$  bonded carbon. However, amorphous carbon and graphite peaks at  $1400\text{ cm}^{-1}$  and  $1580\text{ cm}^{-1}$ , respectively, were observed at both laser powers. At 200 W, the amorphous carbon and graphite peaks exhibit relatively high counts especially for

speeds 42 and 85 mm/s. In the coupon processed at 42 mm/s, higher intensities in both amorphous carbon and graphite peaks were observed but the graphite peak tended to be stronger. In the coupon processed at 85 mm/s, the amorphous carbon peak has slightly higher intensity than graphite and hence it was chosen as the optimum parameter. At 1000 W, a higher graphite count was noted which is primarily due to the high heat. Some amorphous carbon started to appear but the intensity of the peaks did not compare well to the intensity of the peaks found at 200W. After identification of the optimum parameters, a multi-pass laser treatment was used to cover the entire surface of aluminum with composite coatings. This was done using a raster fill motion of the laser beam with a 5% overlap. It took 70 passes for sintering to be completed (Figure 9).

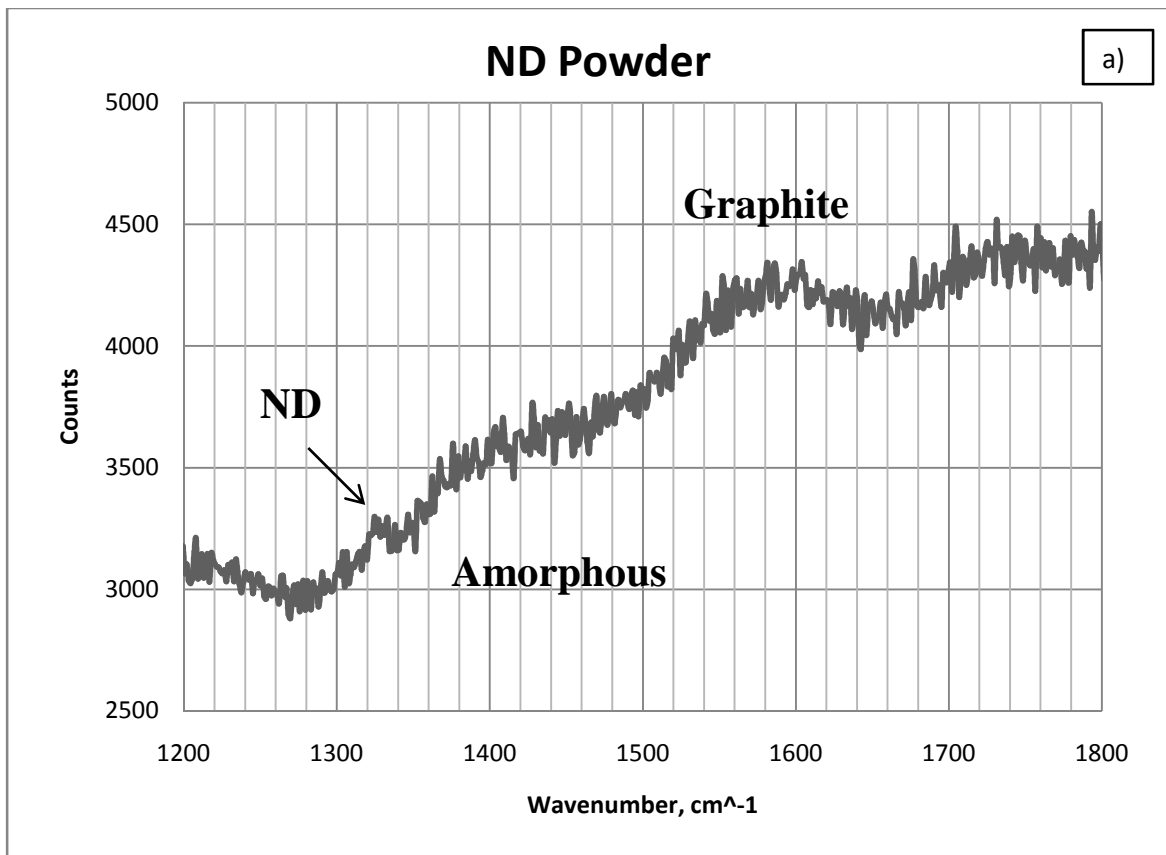


Figure 8: a) Raman spectrum of raw ND powder; b) Raman spectra of coupons processed at 200 W; c) Raman spectra of coupons processed at 1000 W

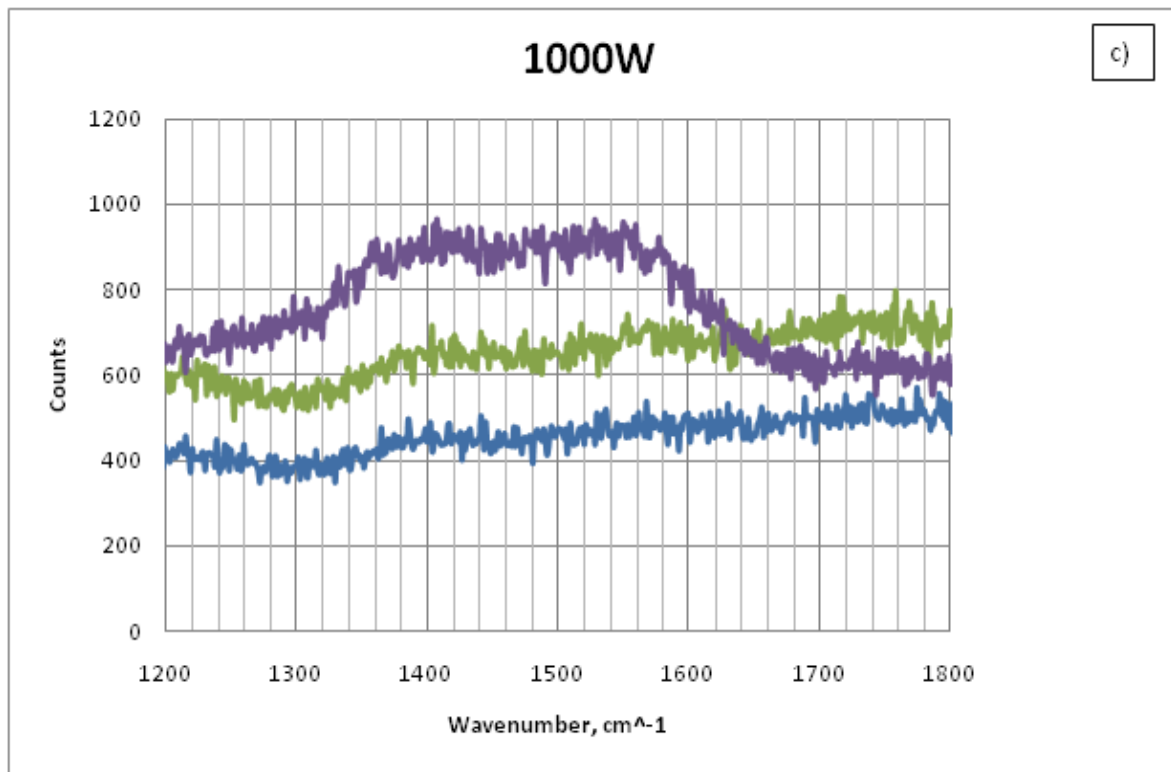
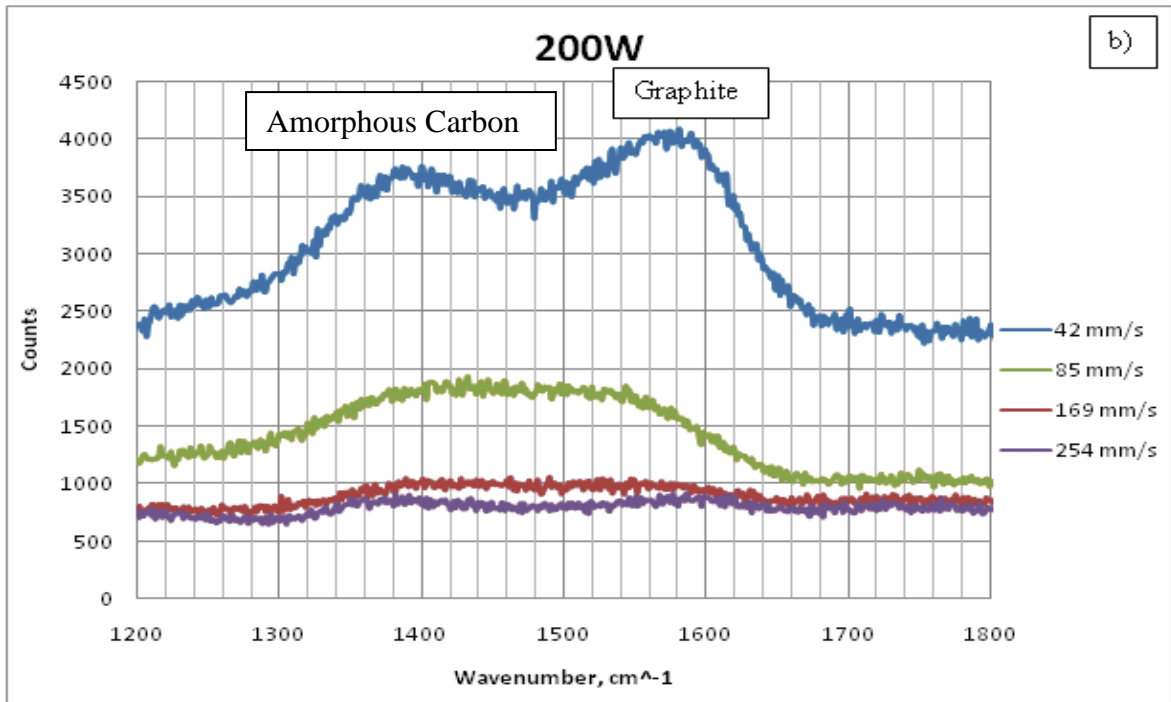


Figure 8: a) Raman spectrum of raw ND powder; b) Raman spectra of coupons processed at 200 W; c) Raman spectra of coupons processed at 1000 W



Figure 9: Digital photograph of optimally laser-sintered coupon

Upon completion of the sintering, a rough surface consisting of peaks and valleys was observed and attributed to the Gaussian energy distribution of the laser beam. The valleys were created by the center of the focused laser beam while the ridges were created by the outer edge of it. Figure 10 shows Raman spectrum of the optimally laser-sintered coupon where amorphous carbon and graphite are observed only at the peaks of the coating. Peaks seen at or around  $1360\text{ cm}^{-1}$  and  $1560\text{ cm}^{-1}$  are known as the D and G peaks, respectively [38]. These peaks are primarily due to  $sp^2$  sites, and are broader than the  $1332\text{ cm}^{-1}$  diamond peak. The G peak is from the bond stretching of all pairs of  $sp^2$  atoms in both rings and chains while the D peak is due to the breathing modes of  $sp^2$  atoms in rings [38]. Diamond-like carbons with the highest  $sp^3$  content have been shown to have a D peak [38].

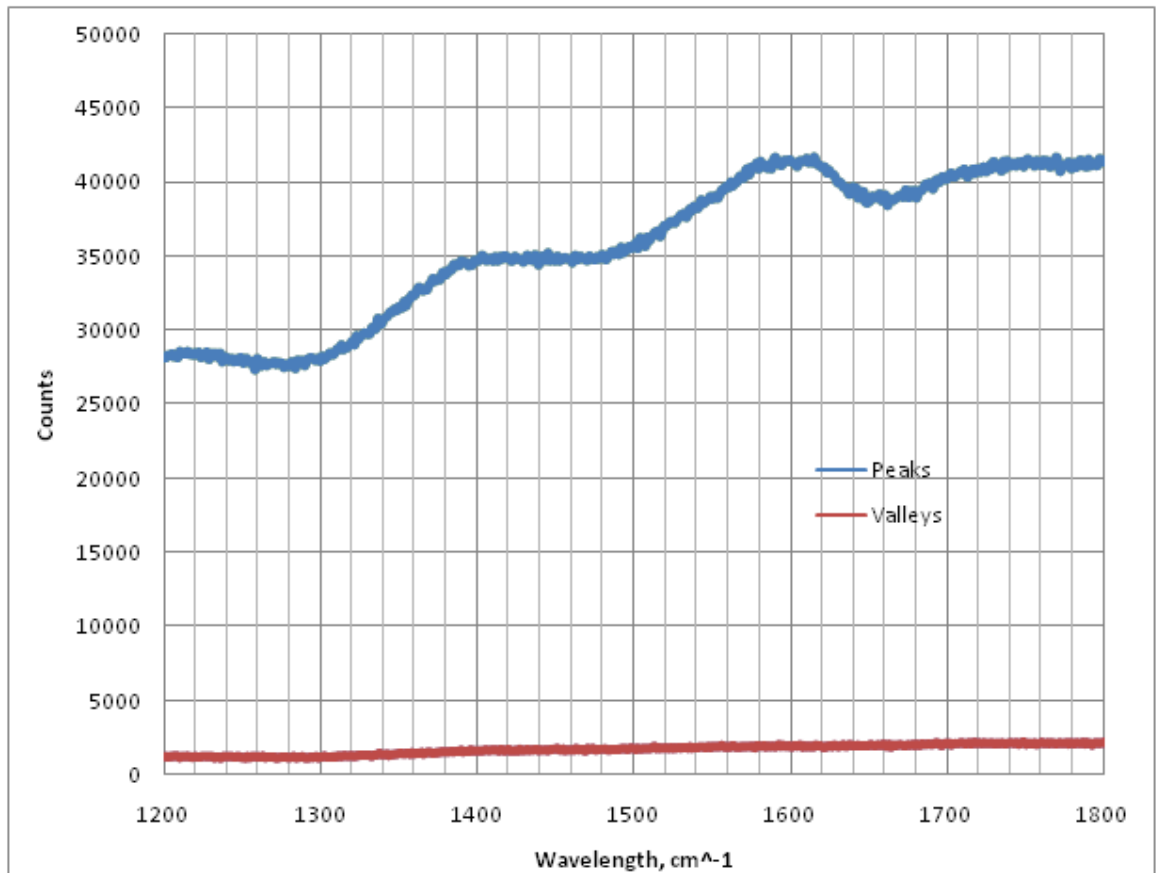


Figure 10: Raman spectra of optimally laser-sintered coupon (200 W, 85 mm/s)

### 3.3 Scanning Electron Microscopy (SEM)

Figure 11 shows SEM micrographs of the electrostatically spray deposited and optimally laser-sintered coupons. Backscattered electron (BSE) imaging was also performed to reveal a sharp contrast between the elements. The images of the electrostatically spray coated coupon show that the surface has agglomerates of 3-6  $\mu\text{m}$ . Laser sintered coupon exhibits two types of features: a smooth, “weld type” of structure

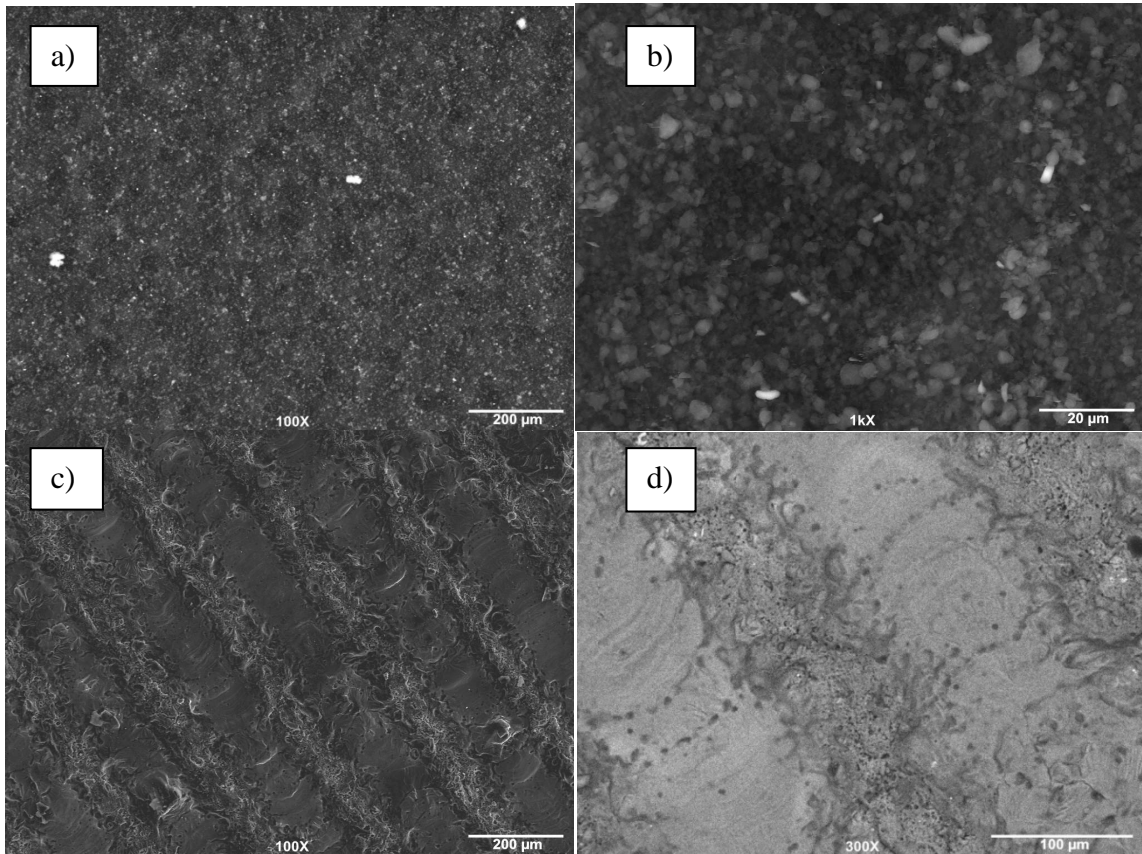


Figure 11: SEM micrographs. a) and b) Electrostatically spray coated coupon; c) Secondary electron image of laser-sintered coupon; d) Backscattered image of laser-sintered coupon

representing the valley and a flaky raised feature representing the peak. The width of each feature is about 100  $\mu\text{m}$ . The chemical makeup of the valleys appears to be resolidified Al-Si-Cu while that of the peaks is a mixture of carbon and aluminum based on the contrast of features in BSE and EDX analysis (Figure 12). As expected, the electrostatically spray coated surface consists of primarily carbon and some oxygen. However, the laser-sintered coupon exhibits a composite of aluminum and carbon. Figure 13 is a transverse section showing the composite coating for a thickness of 50-75  $\mu\text{m}$ .

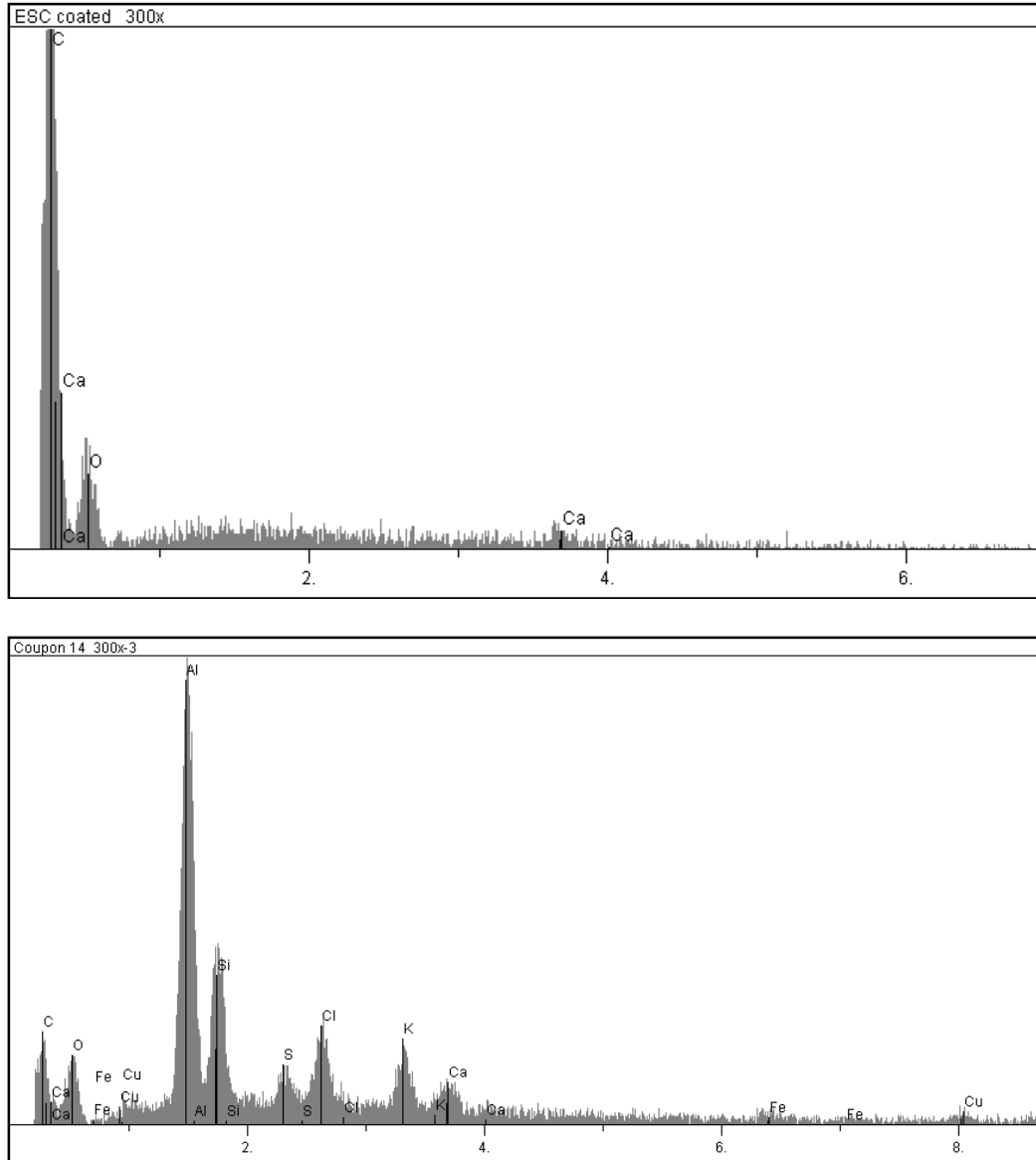


Figure 12: EDX analysis of (Top) Electrostatically spray coated coupon, (Bottom) Laser-sintered coupon

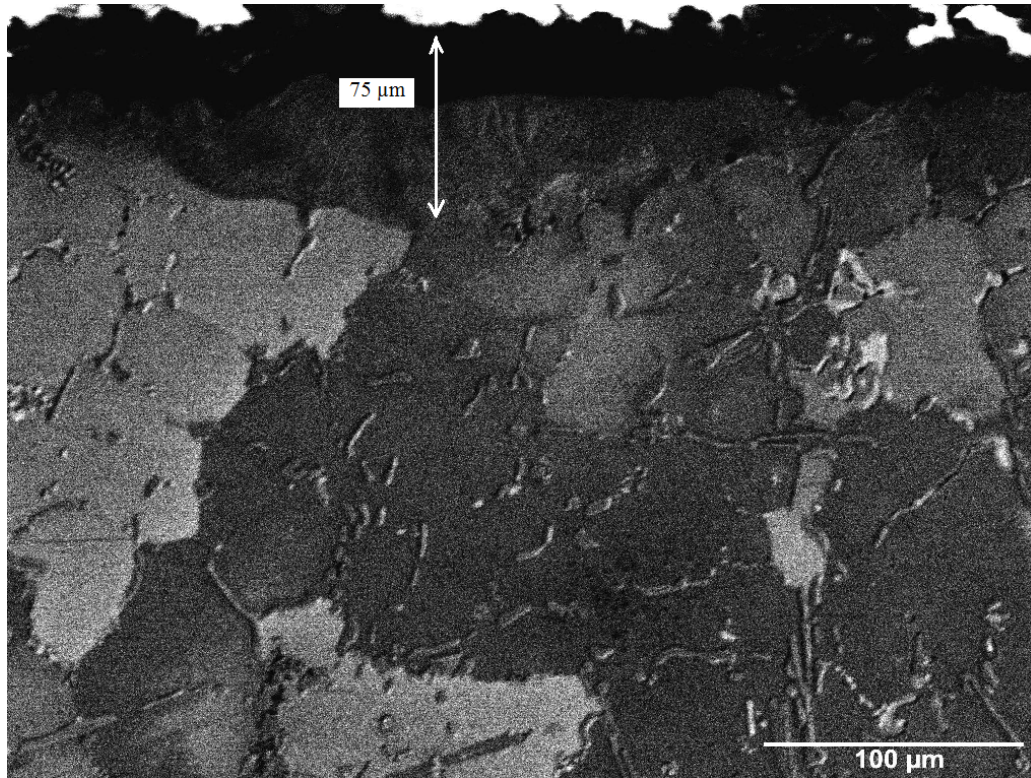


Figure 13: SEM image of the transverse section of laser-sintered coupon showing the coating

Laser sintering of ND powder involves several physical phenomena including energy absorption, heating and densification of the powder, aluminum (binder) melting, and sintering of particles. Laser power, energy distribution, spot size, beam speed, and extent of overlapping control these phenomena. Multiple scattering occurs within the electrostatically coated powder and assists in a nearly homogeneous absorption of the radiation in the powder. Densification is mostly completed in the solid state based on the report that the onset of sintering temperature in laser sintering of nanopowders is 0.2-0.3  $T_m$  as compared to 0.5-0.8  $T_m$  for microscale powders where  $T_m$  is the melting temperature [39]. The process then becomes liquid-phase laser sintering when ND particles are dispersed in a thin molten pool of aluminum. Here the laser energy was

used only to raise the temperature of aluminum binder to melt and flow through the diamond particles by driving forces such as the liquid pressure, viscosity and capillary forces through the pores between the solid particles. With its high surface tension, the molten aluminum wetted the diamond particles and thus the process produced dense layers by the *in-situ* filtration mechanism.

The surface temperature is estimated using the experimental data of melt depth (75  $\mu\text{m}$ ) of optimally sintered coupon and application of the solution to the standard heat conduction in laser melting of aluminum as follows:

$$T(z, t)/T(0, t) = \pi^{1/2} \operatorname{ierfc}(z/2(\kappa t)^{1/2})$$

Where  $T(z, t)$  is the temperature at depth  $z$ , time  $t$ ,  $T(0, t)$  is the temperature at the surface at time  $t$ ,  $z$  is the depth,  $\kappa$  is the thermal diffusivity, and  $t$  is the laser beam dwell time on the surface [40]. This yielded an estimated surface temperature of 1012 K for this process as shown below.

$z = 75 \mu\text{m}$ ,  $T(z, t) = 843 \text{ K}$  (melting point of A319),  $\kappa = 70 (10^6) \mu\text{m}^2/\text{sec}$ ,  $t = 0.2/85 = 0.0024 \text{ sec}$

$843/T(0,t) = \pi^{1/2} \operatorname{ierfc}(75/2(\kappa t)^{1/2}) = \pi^{1/2} \operatorname{ierfc}(0.1) = 0.833$  and so  $T(0,t) = 1012 \text{ K}$

The melting points of diamond and aluminum alloy are 3800 K and 843 K respectively. At temperatures encountered in the laser sintering, ND can potentially undergo phase transition to graphitic phase. For example, studies of the high-temperature transformation of diamond to graphite performed on micro-sized diamond powders revealed that specimens which were heated below 1500 K remained as diamond while

those which had been heated to above 1500 K but below 2300 K transformed into a mixture of diamond, DLC and graphite [41, 42]. However, the conversion of diamond nanopowder into DLC occurs around 940 K [43] at ambient pressure in fast pace due to large surface area of nanoparticles. Consequently laser sintering provided a homogeneous and dense composite coating of ND, DLC and aluminum. Similar to the current study, Dahotre et al [44] sprayed fine FeO powders on aluminum A 319 (engine cylinders) and then subjected them to laser surface treatment with a 1.5 kW continuous wave Nd:YAG laser at 58 mm/sec such that a thin layer of Al substrate melted and mixed with FeO due to the convection currents within the melt zone. This coating exhibited a refined dendritic microstructure (5  $\mu\text{m}$ ) compared to the cast substrate structure (50  $\mu\text{m}$ ). Also there were no cracks or delamination within the laser-melted zone and along the interface between the coating and the substrate implying the existence of a strong metallurgical bond.

### 3.4 Surface Roughness

Surface roughness was measured at three randomly selected sites for each of bare aluminum, electrostatically spray coated and optimally laser-sintered coupons. In the case of laser-sintered coupon, measurements on peaks and valleys were taken. Figure 14 shows the roughness profile plots along with optical images. An average roughness of 5.8  $\mu\text{m}$  along the peaks and 4.5  $\mu\text{m}$  along the valleys was found in laser-sintered coupon. Dahotre et al reported a similar surface roughness of 4.75  $\mu\text{m}$  (Ra) in Nd:YAG laser surface engineered FeO on A319 aluminum [44]. Figure 15, a comparison of the surface roughness data, illustrates that the laser-sintered coupon has the roughest surfaces over electrostatically spray coated and bare aluminum coupons. This would explain why we

had a difficult time in taking accurate hardness measurements. Rougher surface in electrostatically spray coated coupon over bare aluminum is attributed to the varying thickness of the ND powder.

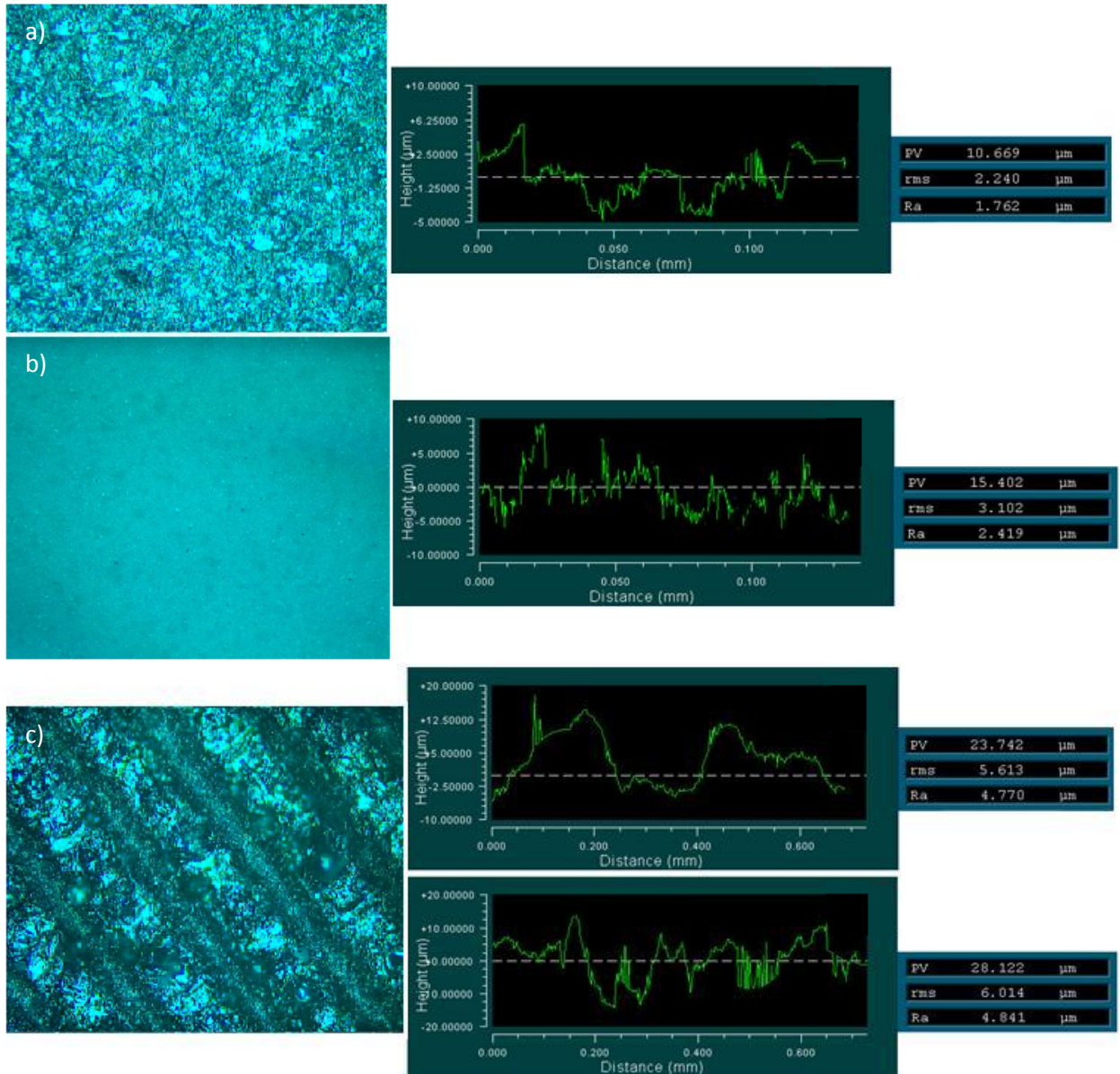


Figure 14: Optical images with roughness profiles: a) Bare aluminum surface b) Electrostatically spray coated surface c) Laser sintered surface with (Top) Roughness plot along one of the peaks (Bottom) Roughness plot along one of the valleys

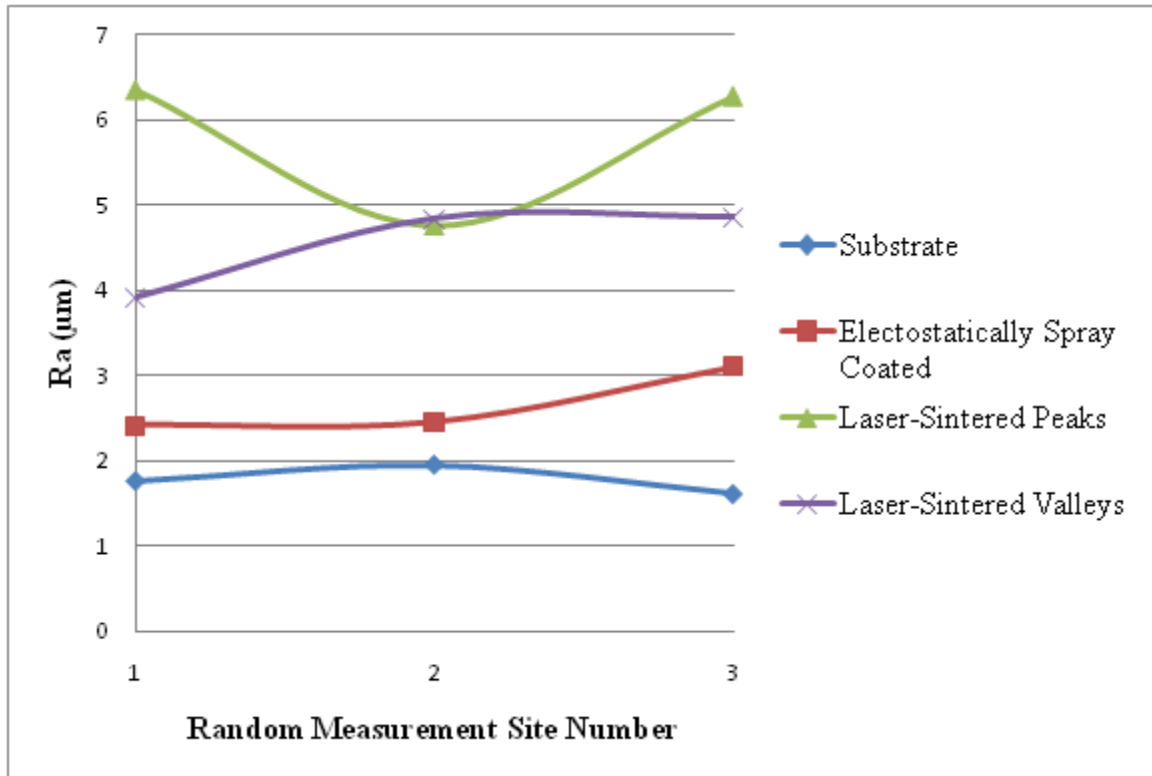


Figure 15: Chart comparing the different coupons by their surface roughness

### 3.5 Microhardness Test

It was difficult to obtain reliable readings in laser-sintered coupon because of the rougher surface profile combined with the higher hardness of the diamond particles. Two measurements were successful with the hardness being 7.3 GPa and 4 GPa on the peaks of the coating. These two measurements are within the range that we found in nanoindentation that will be discussed in the next section. The Vickers microhardness of the substrate was measured as 1.2 GPa. Thus, nearly 3 to 6 times increase in microhardness can be seen; this is attributed to the refined microstructure of aluminum and the presence of ND coatings. Dahotre et al also reported an increase in Knoop microhardness by almost two times that of aluminum substrate in laser surface coated FeO on A319 alloy [44].

### 3.6 Nanoindentation

Nanoindentation data was recorded with several indentations made on peaks and valleys of laser sintered coupon for hardness and elastic modulus measurements. The surface was flattened prior to making the test (see Figure 5) in order to make clear indentation. However some tests led to total fracture of the peak areas through the formation of chips. This type of unacceptable force plot can be seen in Figure 16a and such data was discarded. Figure 17 shows an AFM image of one of the indentations made on the peak of laser-sintered coupon. The contrasting colors in the image are due to change in the topography the surface. Indentations were made using a force of 1000  $\mu\text{N}$  for a depth of 33-413 nm and 8500  $\mu\text{N}$  for a depth of 421-584 nm. The wide range of depths observed at a force of 1000  $\mu\text{N}$  can be attributed to the varying hardness of the surface.

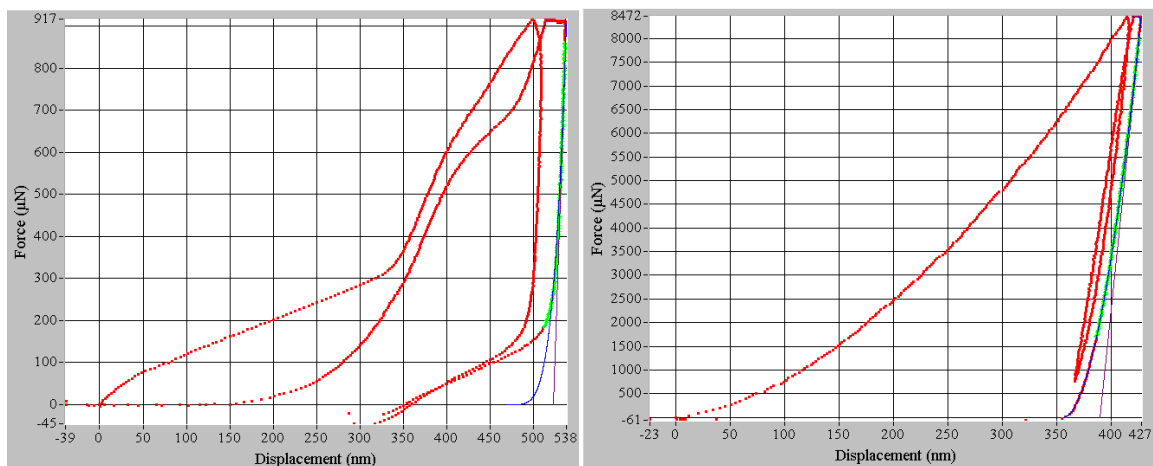


Figure 16: a) (Left) Unacceptable force plot due to surface breakage b) (Right) Example of an acceptable force plot. Both plots are from the optimally laser-sintered coupon

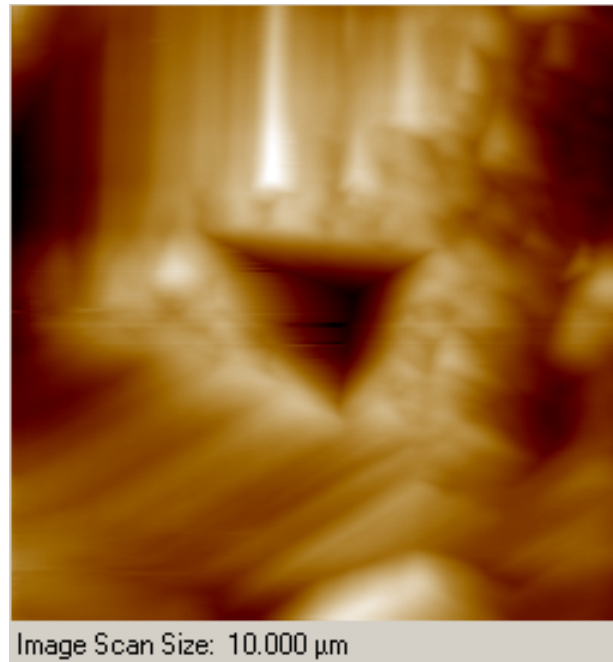


Figure 17: AFM image of one indentation made on the laser-sintered coupon

Based upon a large number of acceptable tests, laser-sintered coating had a hardness range from 0.2 to 4 GPa and Young's modulus range from 20-71 GPa on the peaks. One indentation on a peak yielded a hardness of 23 GPa and a Young's modulus of 217 GPa. The differences in hardness and Young's modulus values are attributed to the differences in chemical makeup and microstructure of the coating. It was difficult to get a good load curve from the valley indentations. Figures 18 and 19 show the distribution of hardness and Young's modulus respectively. Dahotre et al reported an increase in nanoindentation hardness from 1.33 GPa for the 319 aluminum substrate to 1.78 GPa for laser remelted/FeO coated aluminum [44]. However, the elastic modulus remained unchanged at about 80 GPa, implying that the hardness was only sensitive to microstructural and chemical changes. Similarly laser surface melting and subsequent rapid solidification of 700  $\mu\text{m}$  layers of A319 alloy resulted in very fine, cellular dendrite

structure with soft aluminum cells and intercellular hard Si phases that led to an increase in nanoindentation hardness from 0.8 GPa to 1.22 GPa [45]. However the Young's modulus remained same at 75 GPa for both unmelted and laser-melted substrates.

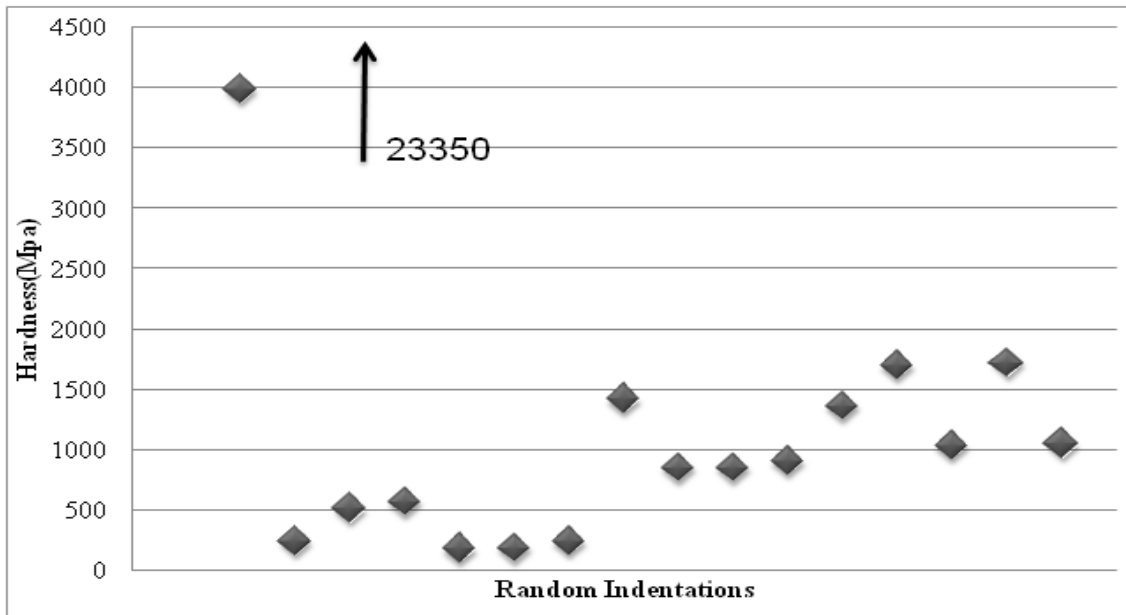


Figure 18: Distribution of nanoindentation values

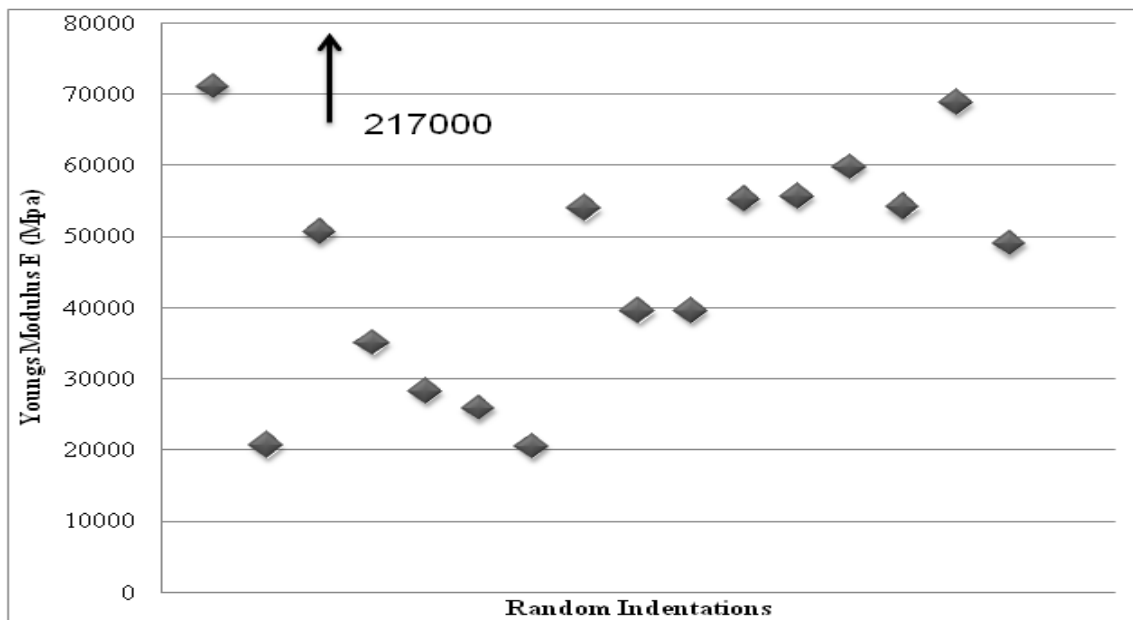


Figure 19: Distribution of Young's modulus values

### 3.7 Friction and wear

Figures 20 and 21 and Table 6 present the results of friction and wear of bare aluminum (uncoated) and laser-sintered aluminum (coupon # 14). For the bare aluminum, the frictional coefficients are much higher and remained steady throughout the duration of tribotest. The “break-in” period was not observed for the bare aluminum. For laser-sintered coating, the friction was very low during the “break-in” period and then reached to a high value afterwards. During the “break-in” period, the presence of ND layers prevented the friction from reaching high values despite a rough surface. Subsequent exposure of the aluminum to the steel counterface increased the friction. The friction could have been less if the counterface material was other than steel because there is a chemical affinity between diamond and steel. Luo et al deposited nanocrystalline diamond on WC using a cathodic arc deposition process and then rubbed against different counterface materials [46]. The resulting frictional coefficient was much higher for steel counterface which was attributed to the attraction of graphitic dangling bond by 3d orbitals of Fe. Malaczynski et al examined DLC coatings for A390 and found a coefficient of friction of about 0.4, which is similar to the 0.39 obtained in this work [47].

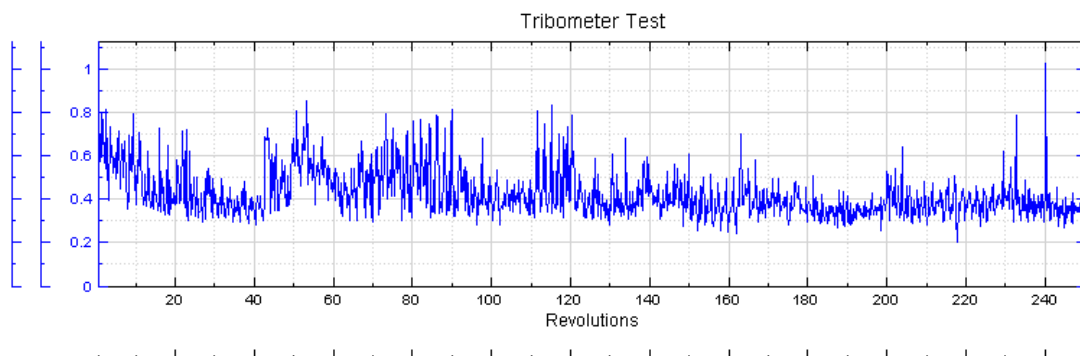


Figure 20: Friction of 319 aluminum substrate against 440C steel

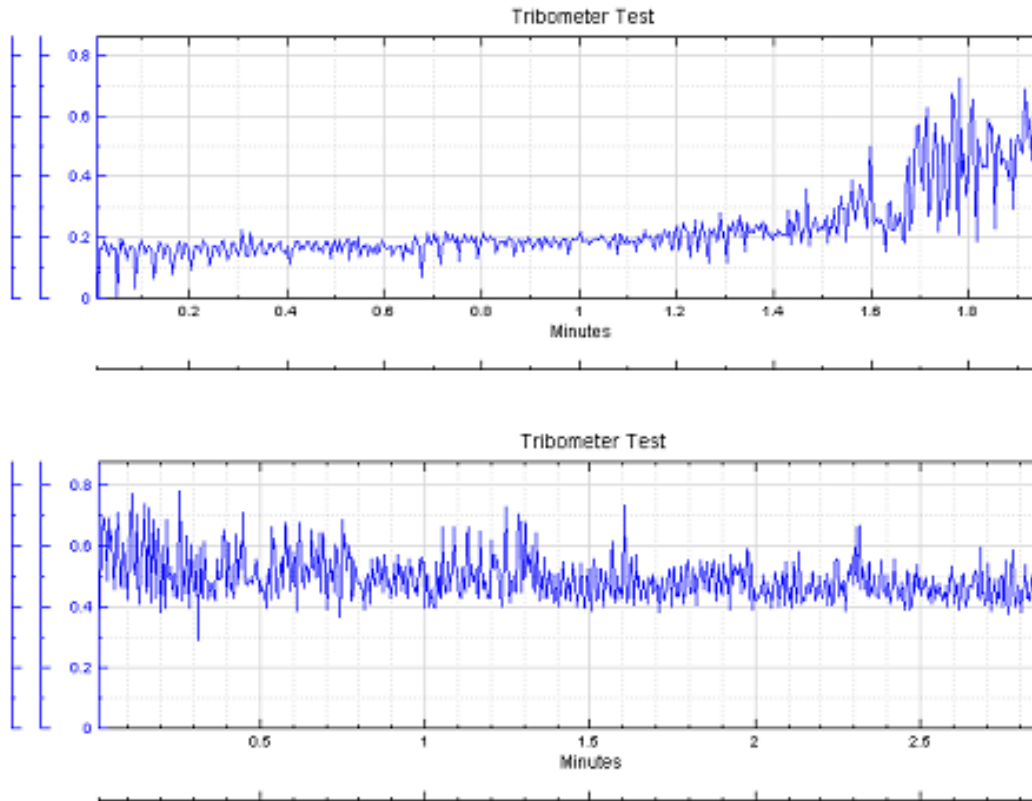


Figure 21: Friction of laser-sintered coupon against 440C steel. (Top) 0-2 minutes  
(Bottom) 2-5 minutes

Table 6: Table comparing the coefficient of friction and wear rate of the optimally laser-sintered coupon and the bare aluminum substrate

	Average COF	Minimum COF	Maximum COF	Area of Wear Track (microns <sup>2</sup> )	Wear Rate (10 <sup>-3</sup> mm <sup>3</sup> /Nm)
<b>Laser-Sintered</b>	0.393	0.000	0.781	2681.75	2.156
<b>Bare Aluminum</b>	0.425	0.200	1.028	14823.0	11.85

Wear data in Table 6 shows that the wear rate is decreased by 5.5 times in laser sintered coatings over the bare aluminum, indicating the beneficial effects of hard coating and microstructure of laser-melted aluminum. Dahotre et al used block-on-disk tribometer tests to evaluate the wear characteristics and showed that laser refined/FeO

coated 319 alloy decreased the wear rate by 71% over uncoated alloy despite only a marginal increase in hardness [44]. Figures 22 and 23 are the profile deviations of wear tracks where the peak-to-valley distance is larger for laser-sintered coupon over bare aluminum. This is in contrast to Dahotre et al's work where worn FeO-coated sample was smoother (3.85 Ra) than worn A319 Al (5.64 Ra) sample surfaces [44]. We believe that the hardness variation in the composite coating as compared to bare aluminum is responsible for the localized wear loss, contributing to the difference in worn surfaces.

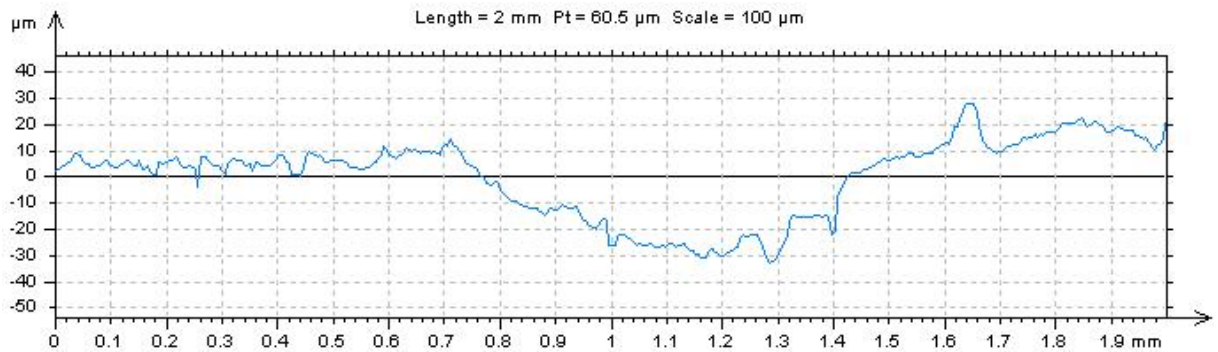


Figure 22: Wear track profile of 319 aluminum substrate against 440C steel

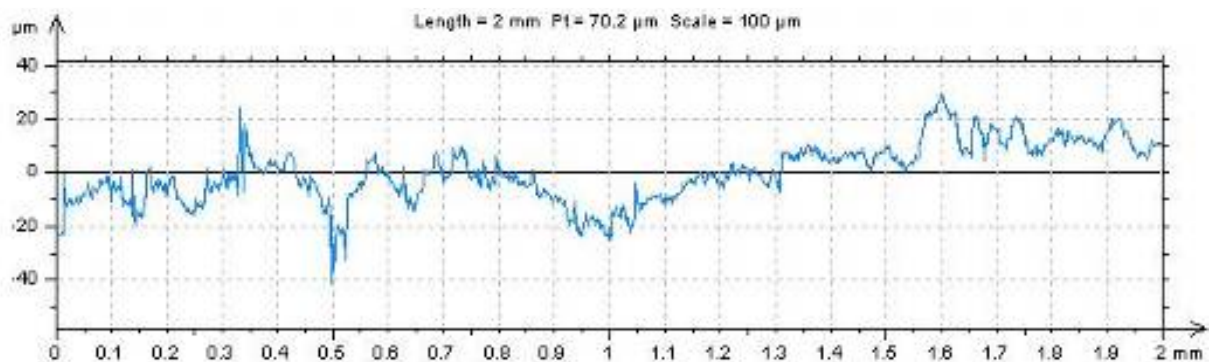


Figure 23: Wear track of laser sintered aluminum against 440C steel

Figure 24 shows the optical micrographs of the wear tracks. The bright regions are reflective of the worn surfaces while the darker parts were either not worn or less worn during the test. The wear mechanism appears to be delamination in both cases. For

the uncoated A319, Dahotre et al [44] proposed that the wear consists of breaking, detaching and falling of hard asperities and hard eutectic mixture from the surface and subsurface regions leaving behind pits/voids followed by the plastic deformation of a highly ductile matrix to generate leaps and folds. Figure 25 shows the SEM micrographs of laser-sintered sample that confirm the delamination mechanism by revealing the slight grooves and the smearing of thin sheets caused by plowing. EDX used to analyze the composition of the wear track (Figure 26) did not show any evidence of the transfer of material from the steel ball to the coupon.

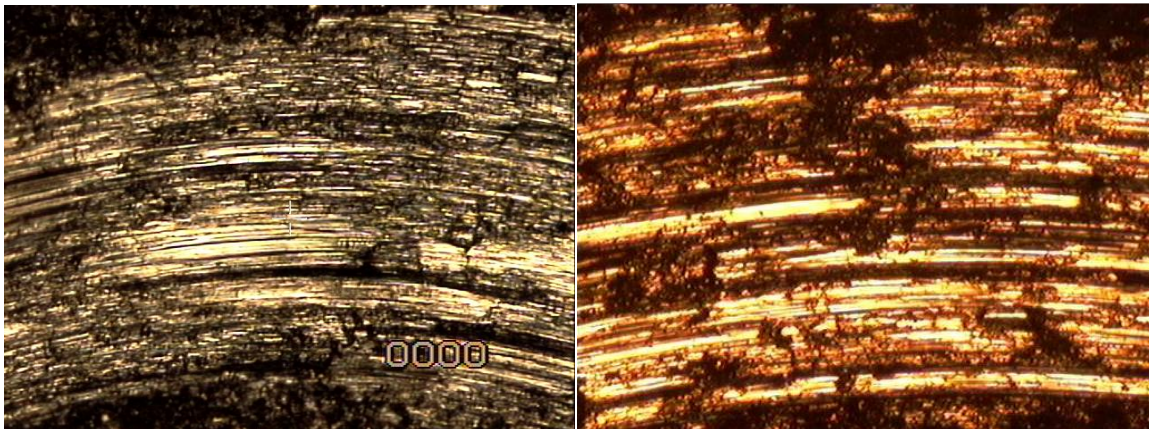


Figure 24: Optical micrograph of wear tracks at 50x magnification (Left) Bare aluminum (Right) Laser-sintered coupon

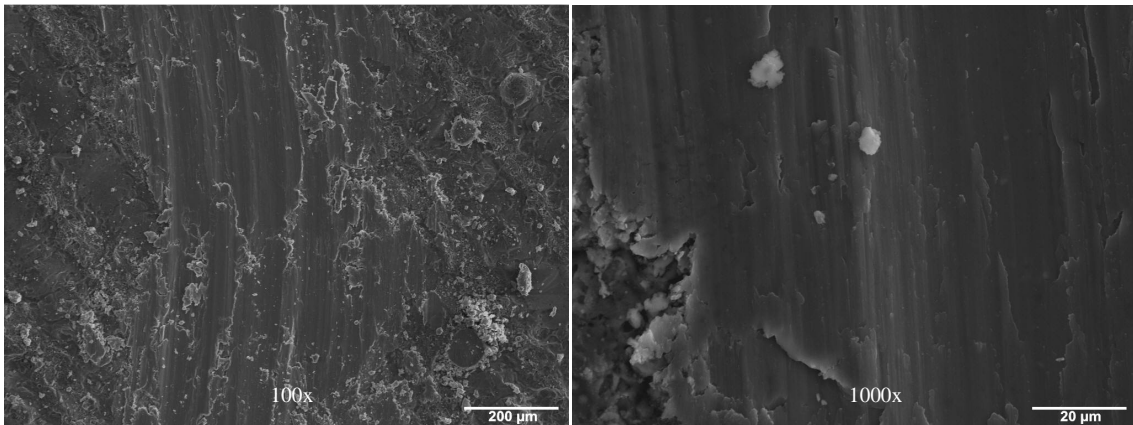


Figure 25: SEM images of wear tracks on the optimally laser-sintered coupon

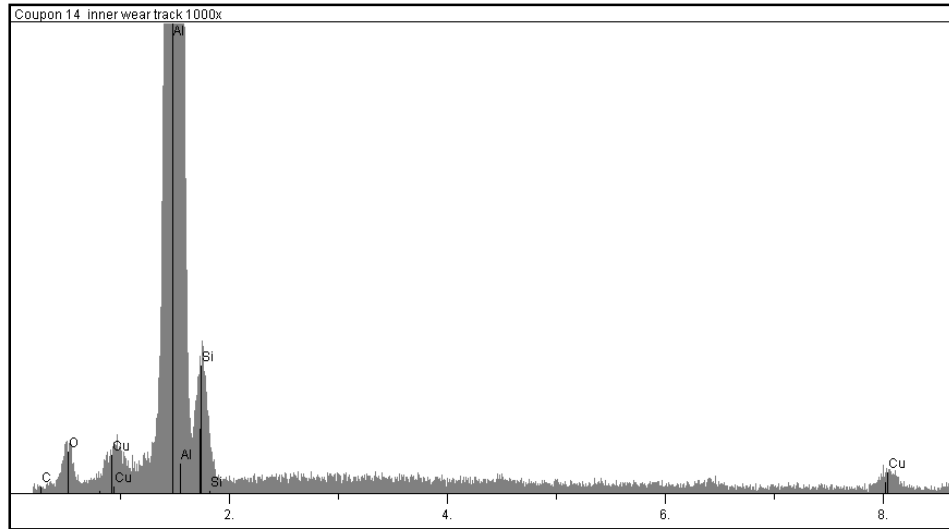


Figure 26: EDX analysis of wear track on optimally laser-sintered coupon showing that there is no iron meaning that particles from the steel ball used in the test did not transfer to the coupon

### Conclusion

A laser-based thermal sintering technique for forming ND composite coatings on aluminum was investigated. This technique is advantageous due to the large surface area-to-volume ratio of nanodiamond enabling better energy absorption and low sintering temperatures. Coatings consisting of nanodiamond, amorphous carbon and graphite phases can be produced. The coating exhibits excellent adherence to the substrate due to a melt layer formed during the process. The friction and wear results seen in this work will allow it to be applied to lightweight components in systems where energy loss due to friction and wear is detrimental. It can be applied to engine components, biomedical implants, polymeric parts and cutting tools.

### Acknowledgements

The authors would like to thank the National Science Foundation for the Grant 0738405. We also appreciate Dr. Anatolli Frishman for providing the ND powders, Dr.

Wenping Jiang for electrostatically spray coating our samples and Mr. Hal Sailsbury, and Vitalli Brand for their help in characterizing the coatings.

### References

1. Priest, M. and Taylor, C.M., *Wear*, 241(2000) 193-203
2. D.A. Parker et al., *IMech E*, C5/82 (1982) 31-33
3. J. Patel, and N.Saka, <http://www.nasatech.com/Briefs/Oct99/ETB10991.html>
4. X. Nie, A. Wilson, A. Leyland, A. Matthews, *Surf. Coat. Tech.*, 131, 1-3 (2000), 506
5. D. Monaghan, K. Laing, P. Logan, P. Teer and D. Teer, *Mater. World*, 1, 6, (1993) 347
6. O. Fuchs, C. Friedrich, G. Berg, E. Broszeit, A. Leyland and A. Matthews, *Materialwiss. Werkst.*, 29, 3 (1998), 141
7. A. Almeida, M. Anjos, R. Vilar, R. Li, M. Ferreira, W. Steen and K. Watkins, *Surf. Coat. Tech.*, 70 (1995) 221
8. K. Watkins, M. McMahon and W. Steen, *Mat. Sci. Eng. A-Struct.*, 231, 1-2 (1997) 55
9. Y. Fu, A. Batchelor, Y. Gu, K. Khor and H. Sing, *Surf. Coat. Tech.*, 99, 3 (1998), 287
10. J. Kelly, K. Nagarathnam and J. Mazumder, *J. Laser Appl.*, 10, 2 (1998), 45
11. H. Man, C. Kwok, T. Yue, *Surf. Coat. Tech.*, 132, 1 (2000) 11
12. S. Zhang, X.L. Bui and Y. Fu. *Surf. Coat. Tech.*, 167, 2-3 (2003), 137
13. H.L. MacLean and L.B. Lave. *Pror. Energy Combust. Sci.* 29, 1 (2003), 1
14. B. Wielage, A. Dorner, *Surf. Coat. Tech.*, 108-109 (1998) 473
15. G. Malaczynski, A. Hamdi, A. Elmoursi, X. Qiu, *Surf. Coat. Tech.*, 93 (1997) 280
16. W. Kimberly, *Automotive Engineer*, London, England  
<http://www.autofieldguide.com/columns/0506euro.html>
17. V.Y. Dolmatov, *Russ. Chem. Rev.*, 70 (2001) 607-626
18. G. Post, V.Y. Domatov, V.A Marchukov, V.G. Sushchev, M.V. Veretennikova, and A.E. Sal'ko, *Russ. J. Appl. Chem.*, 75 (2002) 755-760
19. G.P. Bogatyreva, M.A. Marinich, N.A. Oleynik, and G.A. Bazaliy, *Kluwer Acad. Pub.*, (2002) 111-119
20. G.P. Bogatyreva, M.A. Marinich, and V.L. Gvyazdovskaya, *Diam. Relat. Mater.*, (2000) 2002-2005
21. A.A. Bochechka, *Phys. Solid State*, 46 (4) (2004) 668-671
22. V.F. Britun, G.S. Oleynik, N.P. Sememenko, *J. Mater. Sci.*, 27 (16) (1992) 4472-4476
23. K. Ueda, M. Kasu, A. Tallaire, T. Makimoto, *Diam. Relat. Mater.*, 15 (2006) 1789-1791
24. G.N. Yushin, S. Osswald, V.I. Padalko, G.P. Bogatyreva, Y Gogotsi, *Diam. Relat. Mater.*, 14 (2005) 1721-1729
25. S. Osswald, A. Gurga, F. Kellog, K. Cho, G. Yushin, Y. Gogotsi, *Diam. Relat. Mater.*, 16 (2007) 1967-1973

26. J. Chen, S.Z. Deng, J. Chen, Z.X. Yu, N.S. Xu, *Appl. Phys. Lett.* 74 (1999) 3651-3653
27. Z. Qiao, J. Li, N. Zhao, C. Shi, P. Nash, *Scripta Mater.*, 54 (2006) 225-229
28. E. Cerri, E. Evangelista, S. Spigarelli, P. Cavaliere and F. DeRiccardis, *Mater. Sci. Eng.*, 284 (2000) 254-260
29. J.P Kruth, X. Wang, T. Laoui and L. Froyen, *Assembly Autom.*, 23 (2003) 357-371
30. D.T. Pham, S. Dimov, F. Lacan, *P. I. Mech. Eng.*, 213 (1999) 435-449
31. S. Osswald, G. Yushin, V. Mochalin, S.O. Kucheyev, Y. Gogotsi, *J. Amer. Chem. Soc.*, 128 (35) (2006) 11635-11642
32. B. H. Kear, L.E. McCandlish, *Nanostruct. Mater.*, 3 (1993) 19
33. L.Li, X.Tian, P.Chu, Y.Zhang, X.Cui, H.Zhang, *Nucl. Instrum. Meth. B*, 206(2003) 691
34. Newage Testing Instruments Inc, 6 June 2008, <http://www.hardnesstesters.com/microhardness.htm>.
35. R. Mahmudi, P. Sepehrband and H.M. Ghasemi, *Mater. Lett.*, 60 (2006) 2606-2610
36. S. Prawer, K.W. Nugent, D.N. Jamieson, J.O. Orwa, L.A. Bursill, J.L. Peng, *Chem. Phys. Lett.*, 332 (2000) 93-97
37. A.C. Ferrari, J. Robertson, *Phil. Trans. R. Soc. Lond. A*, 362 (2004) 2477-2512
38. A.C. Ferrari, J. Robertson, *Phys. Rev. B*, 64 (2001) 075414 1-13
39. H. Zhu and R. Averback, *Phil. Mag. Lett.*, 73, 1, (1996) 27
40. P. Batra, *Guide to Laser Materials Processing*, (1993) 243-244
41. M. Seal, *Nature*, 185 (1960) 522
42. T. Evans and P. James, *Proc. R. Soc. Lon. Ser-A.*, 277, 1369 (1964) 260
43. J. Qian, C. Pantea, J. Huang, T. Zerda, Y. Zhao, *Carbon*, 42 (2004) 2691
44. N. B. Dahotre, S. Nayak, and O. Popoola, *J. Met.*, September 2001, 44
45. S. Nayak and N. B. Dahotre, *J. Met.*, January 2004, 46
46. S. Luo, J. Kuo, B. Yeh, J. C. Sung, C. Dai and T. Tsai, *Mater. Chem. Phys.*, 72 (2001) 133
47. G. W. Malacynski, A. H. Hamdi, A.A. Elmoursi, X. Qiu, *Surf. Coat. Tech.*, 93 (1997) 280-286

### **CHAPTER 3. Synthesis of Nanodiamond Coatings on Aluminum Substrates Using Ring Beam-Configured Laser Sintering**

Patent Application, 2008

Rodger Blum and Pal Molian

#### **Abstract**

A novel yet affordable method, *laser-induced phase transition and sintering of nanodiamond powders* (4-8 nm), was investigated to produce tribological coatings of nanodiamond and amorphous carbon on A319 aluminum substrates. A 1000 W continuous wave CO<sub>2</sub> laser with the beam configured in the shape of a ring was utilized. The ring having an outer diameter of 12.7 mm and a width of 0.17 mm in the focal plane was generated by a combination of axicon and planoconvex lens. The laser beam heated the nanodiamond (ND) powder that was electrostatically sprayed on aluminum surfaces and melted a very thin layer of the aluminum substrate in a controlled fashion to form 60 µm thick ND/amorphous coatings. Characterization and evaluation of the coatings was accomplished by Raman spectroscopy, scanning electron microscopy, X-ray diffraction, optical profilometry, nanoindentation and friction/wear tests. Results indicate rapid sintering and phase transition from ND to amorphous carbon at low-temperatures due to the active surfaces of ND and strong adherence of the coating due to the presence of the thin melt layer of the substrate. Raman spectroscopy confirmed the presence of amorphous carbon and graphite phases while energy dispersive analysis revealed a high percentage of carbon in the coatings. The optimum laser parameters were found to be 1000 W and 4.2 mm/sec which provided smoother surfaces than bare and spray-coated coupons. Ball-on-disc tribometer tests showed that laser-sintered coating reduced the

wear rate of aluminum by four times and behaved like a solid lubricant with a coefficient of friction of less than 0.2. The application is targeted towards lightweight components used in internal combustion engines, biomedical implants, magnetic hard disks, cutting tools and polymeric parts for reducing the energy loss associated with friction and improving wear resistance.

**Keywords:** nanocoatings, diamond, tribology, laser sintering

## 1 Introduction

A current challenge for the survival of automotive industry is fuel economy considering the rapid increase in oil price over the past few years. Two factors significantly affect the fuel economy: vehicle weight and frictional loss [1]. Lightweight aluminum alloys such as A319 and A390 drove reduction in vehicle weight enabling fuel efficiency [2]. It is projected that aluminum alloys will substitute cast iron for nearly half of the engine blocks in the next decade; this can reduce the vehicle weight by 30% [3, 4]. However, friction has the most damaging effect on the fuel economy in internal combustion engines, accounting for an energy loss of over 40% [4-6]. Among the friction losses, piston skirt, piston rings and bearings account for about 50% while valve train (tappet/cam journal), crankshaft, transmission and gears cause the remaining 50% energy expenditure [6-8]. Unfortunately, the surfaces of aluminum cylinder bores have poor friction and wear characteristics compared to the cast iron counterparts. Therefore cast iron liners are to be embedded in the aluminum bore; this is in turn detrimental to the measures of weight reduction, rapid heat dissipation and overall increase in power [1].

Hence sleeveless aluminum cylinder blocks with benefits of lightweight and compact design are most preferred [9].

Improvement of the tribological characteristics of aluminum cylinder bores and other engine components is an ongoing, relentless, continuous effort. General Motors has replaced hypoeutectic 319 aluminum alloys with by hypereutectic 390 alloys in Chevy Vega engines with an effort to increase the wear resistance [10]; however, this effort suffered from the difficulty of controlling the distribution of primary silicon in the casting and associated poor castability and machineability. Japanese engine manufacturers evaluated fiber-reinforced composites of aluminum oxide and aluminum for pistons of diesel engines by Toyota [10] and engines bores by Honda [11]. Another attempt is to use a number of thermal spray coating processes to apply different powders and solid lubricants and thereby reduce friction, wear and oil consumption [12-14]. Alternatively, electrolytic coatings such as Ni/SiC electrocomposite coatings were being considered for Honda, BMW, Jaguar and Mercedes Benz engines [1, 5] with superior performance and lower deposition rate over thermal spray coatings [15]. However, none has sparked more excitement than diamond-like carbon (DLC) coatings, which have already been applied to diesel injection systems [8]. The extraordinary properties of DLC include chemical inertness, high hardness, elastic modulus, low friction coefficient and low wear rate [16-19]. DLC coatings have been deposited by various methods including ion beam deposition, magnetron sputter deposition and plasma-enhanced CVD [20].

DLC coatings currently face two challenges: 1) the coating thickness is generally limited to 4  $\mu\text{m}$  or less due to the presence of very high internal stresses caused by thermal expansion mismatch [21, 22]. A recent study by General Motors R&D Center on

<2  $\mu\text{m}$  thick DLC coatings (CVD process) for aluminum A390 alloy showed the beneficial effects of low friction and absence of scuffing wear in the piston bore for automotive engines [23]. However, these thin coatings performed well only for short duration that is unacceptable considering the life expectancy of a modern IC engine. Another consideration is that the coating thickness should be high enough to provide room for polishing, honing and other superfinishing processes; and 2) the coatings have poor adherence causing spallation in service as well as in finishing processes [24]. In order for diamond to strongly adhere to aluminum, thermal expansion of diamond must be increased (for example by incorporating metals in the coating), residual stresses must be reduced and a melt layer of aluminum must be made available. The latter is generally not possible in the traditional CVD/PVD methods. Hence, the focus of this effort is to develop thick ( $>10 \mu\text{m}$ ), uniform and well-bonded nanodiamond/diamond-like carbon (ND-DLC) coatings on cast aluminum substrates using a novel laser sintering process; this will benefit engine components in terms of reduced friction, long-lasting engine and reduced  $\text{CO}_2$  emission and thereby improve the fuel economy and environment.

Nanodiamond (ND) is a new engineering material with properties nearly same as single and polycrystalline diamonds yet possesses special optical properties, higher magnetoresistivity and enhanced friction and wear properties [25]. Unlike their larger counterparts, ND has active surfaces that allow sintering to be achieved at much lower temperatures and cause phase transition to DLC. In this paper, we report a novel laser-based, liquid-phase sintering process of ND powders that enabled deposition of a mixture of ND/DLC coatings on aluminum alloy A319. The rationale for selecting laser sintering is twofold: 1) it is advantageous over furnace sintering in terms of speed, suppression of

the grain growth and particle agglomeration, minimization of the contamination and reduction in the sintering temperature; and 2) the use of nano-sized particles enables increased laser energy absorption and substantially lower temperature sintering; both effects are partly attributed to the large surface area-to-volume ratio of nanoparticles.

## 2 Experimental Details

### 2.1 Materials

In this study, a casting alloy A319 (Al–Si–Cu) well known for its excellent castability, high strength, good corrosion resistance and pressure tightness, was chosen as the substrate. Table 1 lists the nominal composition of A319. The alloy was procured in the form of small ingot from Custom Alloy Light Metals, City of Industry, CA and then cast into 25 mm diameter rods using a permanent molding process and subsequently age hardened to T6 temper. The aluminum rods were then cut into 3.2 mm (1/8”) thick coupons, sand blasted to improve the surface finish and surface cleaned using acetone.

Table 1: Nominal composition of alloy 319 used in this work

Element	Si	Fe	Cu	Mn	Mg	Cr	Zn	Ti	Sn	Pb	Ni	Al
Weight Percent	5.860	0.678	3.519	0.246	0.056	0.104	0.901	0.160	0.021	0.032	0.121	87.80

Nanodiamond powders with particle sizes of 4-8 nm, produced by “shock detonation synthesis” technology, were procured from SPE SINTA Ltd. in Kharkiv, Ukraine. The detonation products typically contain about 50 to 75% diamond and are subjected to a subsequent chemical purification process using nitric acid to obtain 90% or better purity. Table 2 lists the characteristics of ND powders used in this work. Graphitic and metallic impurities account for up to 10%. The 2% metallic impurities are the

elements Ca, Fe, Cu, Al, Cr, and Si. Figure 1 shows transmission electron microscope (TEM) image and corresponding X-ray pattern. The particle surface contains a great number of uncompensated bonds; consequently functional groups (mainly carbonyl, carboxyl and hydroxyl) are adsorbed during the powder synthesis. The ND particles are also prone to agglomeration. The presence of carbon onions surrounding ND particles was also observed in the TEM examination.

Table 2: Characteristics of nanodiamond powder produced by shock explosion

External kind	Powder of gray color
Aggregate Size	20-50 nm
Average size of prime particles (coherent scattering region)	4-8 nm
Specific surface, m <sup>2</sup> /g	250
Density, kg/m <sup>3</sup>	3000
Quantity of metallic impurities, % not more	2.0
Quantity of carbon cubic phase, % not less	90

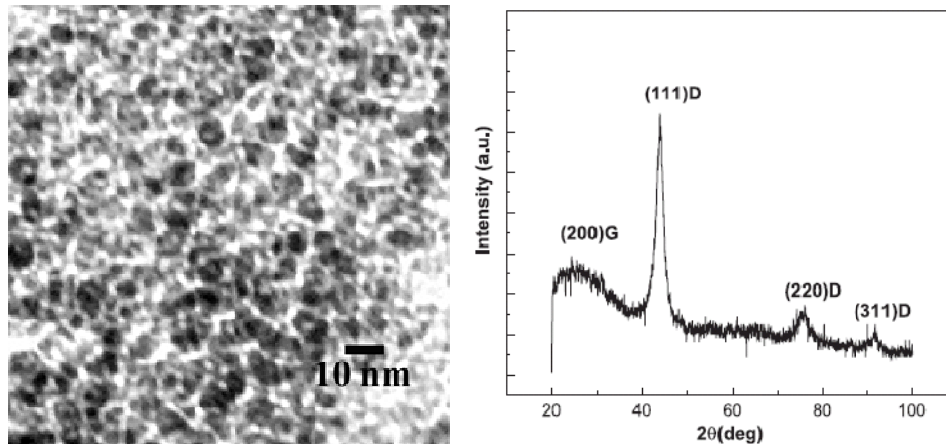


Figure 1: TEM image and X-ray diffraction pattern of nanodiamond powder

## 2.2 Electrostatic Spray Coating

ND powder was electrostatically sprayed on the surface of aluminum coupon for a thickness of 25 to 35  $\mu\text{m}$ . In this process, the ND particles were transmitted through a

spray gun and exposed to an electrostatic field generated by the gun electrode, which is typically at a few tens of kilovolts. The charged powder particles then followed the electric field lines toward the grounded substrate. Certain degree of agglomeration had occurred in the deposited powder.

### 2.3 Laser Sintering

A continuous wave CO<sub>2</sub> laser (Spectra Physics Model 820) of 10.6 μm wavelength with a maximum power of 1.5 kW was employed as the energy source for the sintering process. A three-axis CNC-based controller was used to position the substrate on the worktable. Laser sintering experiments (Figure 2) was performed with a ring beam (12.7 mm diameter, 0.17 mm width), which is described in the next section. The beam was directed in a raster scan pattern to cover the surfaces in which the substrate was moved under the stationary beam. An inert gas (argon) was delivered ( $2.3 \times 10^{-2} \text{ m}^3/\text{s}$ ) at the laser-material interaction zone to prevent oxidation. The laser power and scan rate were varied as shown in Table 3. In addition, some tests were conducted with coupons preheated to 673 K (400°C) to reduce the laser power requirements.

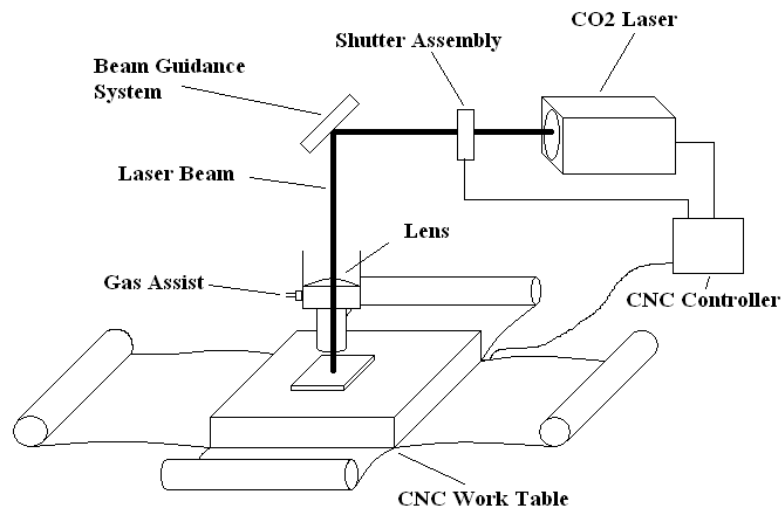


Figure 2: Schematic of the laser sintering setup

Table 3: Laser sintering test parameters

Test Run	Power (W)	Scan Rate (mm/s)
1	200	21.17
2	400	21.17
3	1000	2.12
4	1000	4.23
5	1000	42.33
6	1000	169.33
<b>Coupons preheated to 673 K</b>		
7	200	8.47
8	200	21.17
9	400	8.47

## 2.4 Ring Beam

One of the difficulties in the use of a focused circular beam with Gaussian energy distribution is the coalescence of several nanodiamond particles to form a spherical, ball type of structure as a result of steep temperature gradient developed between the center and edge of the laser-heated zone. The use of a ring beam can prevent this “balling” phenomenon. It is capable of preheating the substrate material and post-heating the sintered zone; both processes are effective in homogenizing the microstructure. Preheating also causes more efficient coupling between the beam and material, thus reducing the required laser power. Unlike the focused circular beam, the ring beam is capable of a more uniform temperature distribution along the scanning direction, leading to reduced thermal distortion. In addition, the ring beam can minimize the residual stress patterns. Furthermore, the degree of convection would be so small that hydrodynamic shear forces will have a negligible influence on the aggregation process. Consequently, the ring beam can facilitate even sintering and reduces residual stresses, thus improving surface integrity and tolerance.

Axicon, also known as a conical lens or a rotationally symmetric prism, was used to convert the parallel laser beam into a ring. Axicon optical systems can transform a Gaussian beam into a diffraction-free Bessel beam (a beam that does not spread as it propagates). In this work a  $2^\circ$  degree Axicon combined with a 127 mm focal length, planoconvex lens was designed (Figure 3) to provide a laser spot with a ring shape of inner diameter of 12.36 mm and outer diameter of 12.70 mm in the focal plane. The Axicon optical system, which forms the annulus, was carefully made to minimize the diffractive effects and optical fabrication errors. The irradiance profile is Gaussian in the annular region. The full-Gaussian annular beam produces smaller melt depths because it generates the maximum temperature inside the annular region and allows heat to be conducted toward both sides (inner and outer circumferences) rather than along the thickness direction.

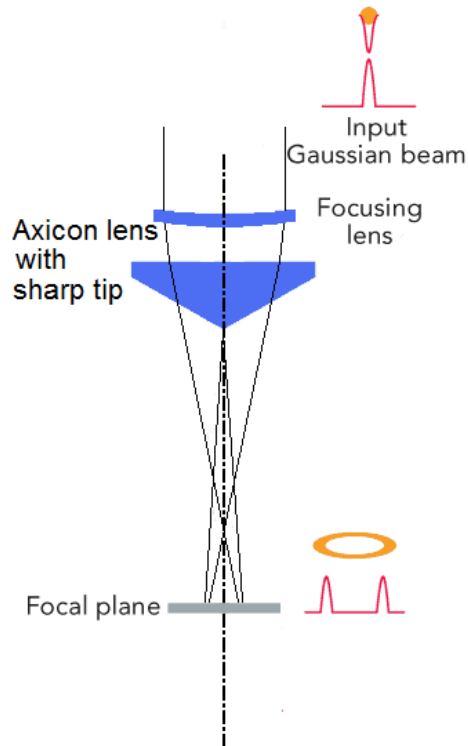


Figure 3: Axicon and plano-convex lens combination to produce ring beam

## 2.5 Characterization and Analysis

Scanning electron microscopy (JEOL Model JSM-840A) was used to characterize the profile, flaws, thickness and microstructures of the sintered layers. Energy-dispersive X-ray and image analysis was used to determine the composition and microstructure transitions. X-ray diffraction (D-8 diffractometer) patterns from a known or approximated crystal data were used to identify diamond and DLC phases. Specifically, peaks corresponding to  $2\theta$  (deg.) of 26.61 (DLC) and 43.62 (diamond, (111)) degrees were examined.

A micro-Raman spectroscope (Reinshaw inVia Raman Microscope) using monochromatic light of wavelength 488 nm was used to identify the diamond structures. When the light hits the surface of the sample, different components of the surface can exchange energy with the light causing Raman scattering. The difference in energy in the scattered light is then measured. Each material has its own Raman shift meaning that the amount of energy it exchanges with the incident light will always be the same, thus allowing Raman spectroscopy to be an important test in characterizing a surface that consists of a mixture of nanodiamond, amorphous carbon, and graphite. These three carbon phases will yield three different Raman peaks. Diamond will give a definite peak at  $1332\text{ cm}^{-1}$  while ND will yield a peak at  $1325\text{ cm}^{-1}$  [26]. Graphite will yield a definite peak at  $1580\text{ cm}^{-1}$ , while diamond-like carbon can yield a range of peaks but the main peak is at  $1355\text{ cm}^{-1}$  [27]. Table 4 shows each carbon phase with its corresponding Raman peak. Thus Raman data was collected through the range of  $1200\text{-}1800\text{ cm}^{-1}$ .

Table 4: Carbon phase and corresponding Raman peaks[27]

Phase	Raman Peak (cm <sup>-1</sup> )
Single Crystal Diamond	1332
Nanodiamond	1325
Diamond-like Carbon	1350
Amorphous Carbon	1350-1450
Onion-like carbon	1572
Graphite	1580

Vickers microhardness (Wilson Tukon Tester) was used to determine the hardness of the ND-DLC coating. In this test, higher loads and smoother surfaces are preferred to increase the measurement resolution. However, in our experiments, the tests on laser-sintered coupons were not successful despite the use of a low load of 25 grams. A Vickers hardness of 120 kg/mm<sup>2</sup> was measured at ambient temperature for the A319 aluminum substrate.

Nanoindentation is a recent method of characterization that can measure mechanical properties (hardness and Young's Modulus) of features less than 100 nm across, and thin films less than 5 nm thick. In this effort, a Hysitron TriboIndenter with a Berkovich tip (three-sided pyramid geometry) of radius 564.2 nm was used with a different process of loading and unloading. In a typical test, the tip is driven into the material until a maximum predetermined force is reached, then held for a few seconds, and finally unloaded. However in our work, a pre-test was performed to flatten the surface before actually making the indentation to eliminate the surface irregularities.

Figure 4 shows the type of load curve used.

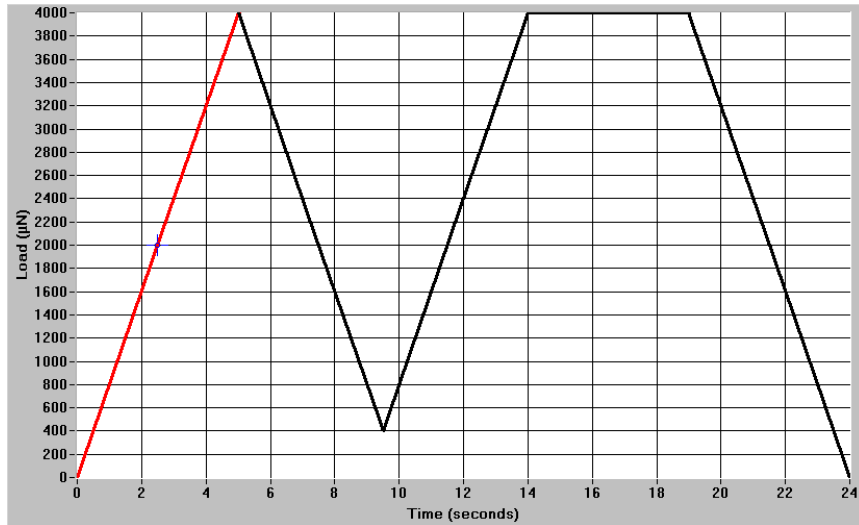


Figure 4: Load curve used to flatten surface before making indentation

An optical profilometer (Zygo New View 6k) was employed to measure the surface roughness of the coupons. It is a non-contact method of finding surface roughness and imaging three-dimensional profile of the surface. It is capable of giving the PV (peak to valley) measurement, the Ra (arithmetic average) deviation from the center line, and rms (root-mean-square) deviation from the center line.

A ball-on-disc tribometer, shown in Figure 5, was used to evaluate the friction and wear characteristics. Test conditions are listed in Table 5. In this test, a ball-shaped indenter is loaded onto the sample with a known force. The ball is mounted to a stiff lever that is designed to be a frictionless force transducer. The sample is then rotated at a certain speed. During this test, the friction forces between the ball indenter and sample are measured by the very small deflections of the lever using an LVDT sensor. The wear coefficients for the ball and sample are then calculated from the volume of material lost during a friction run using the following equation:

$$k = \frac{V}{F \cdot s}$$

where  $k$  is the wear rate coefficient,  $V$  is the volume of material lost,  $F$  is the normal load, and  $s$  is the sliding distance. The units for the wear coefficient are  $\text{mm}^3/\text{Nm}$ .

Table 5: Test conditions for the friction and wear test

Load	5.0 N
Length of test	2 min
Rate	50 rpm
Radius of track	2.5 mm
Sliding velocity	13.1 mm/s
Sliding distance	1.57 m
Revolutions	100
Lubricant	None
Atmosphere	Air
Temperature	296 K (room temperature)
Humidity	35%
Ball diameter	6 mm
Ball material	Stainless steel 440C

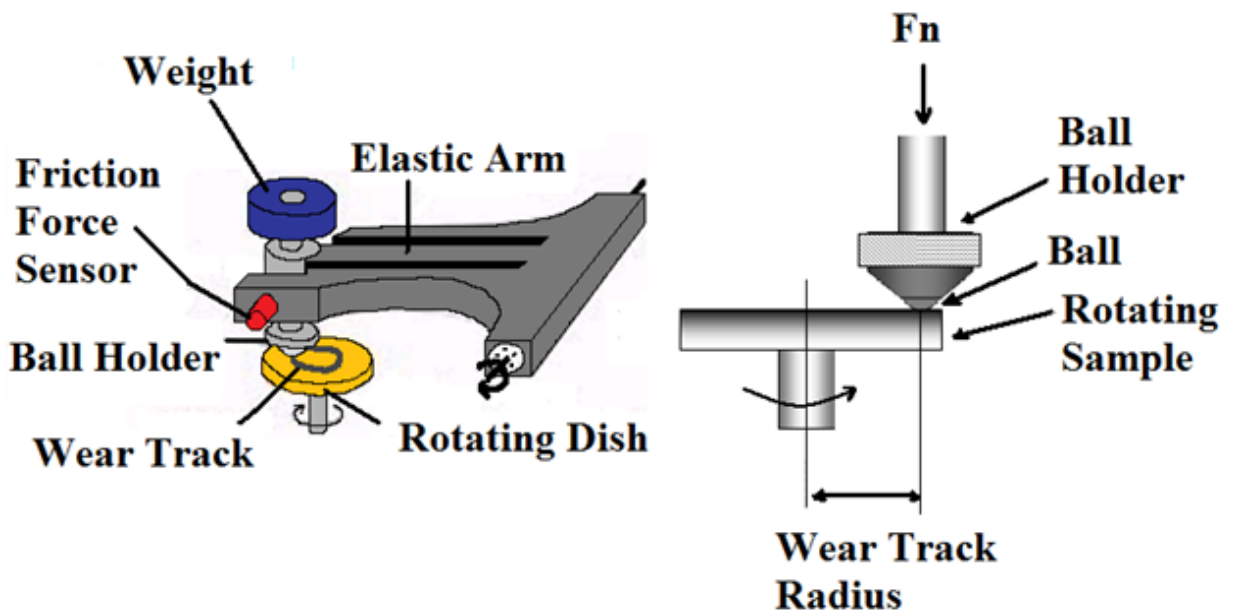


Figure 5: (Left) Ball-on-disc tribometer (Right) Close up of the test setup

### 3 Results and Discussion

#### 3.1 Effect of Laser Parameters

Laser powers in the range of 200 W-1000 W were studied. All powers instantaneously turned the electrostatic sprayed, gray powders into black layers implying the possible phase transition to graphite. However, cleaning in an ultrasonic bath or by simply blowing air easily removed the black layers for those coupons processed at powers less than 1000 W. After removal of the black layer, no effect on the aluminum substrate could be seen. This, along with Raman data, confirmed that laser powers under 1000 W, while caused phase transition, did not provide adequate heat to the surface of the coupon to sinter the ND powder to the aluminum substrate. At 1000 W, there was sufficient heat to cause liquid-phase sintering provided the scan rate was less than 42 mm/s. However, scan rates at or below 2.1 mm/s caused severe melting of the aluminum substrate. In an effort to reduce the laser power, some experiments were conducted by preheating the coupon with a heat lamp to 673 K. This, however, did not yield successful results because of the severe agglomeration and poor adherence of the powders and excessive melting of aluminum.

#### 3.2 Raman Spectroscopy

The black residue found on the surfaces of coupons is believed to be a layer of graphite or maybe soot that formed in the laser sintering process. This layer of loose carbon could mask the Raman spectrum. A cleaning process that consisted of letting the coupon sit in a deionized ultrasonic water bath for 3 minutes was employed to remove the layer. A comparison of the Raman spectra of a coupon before and after cleaning showed that the loose carbon layer was decreasing the intensity of the peaks (Figure 6).

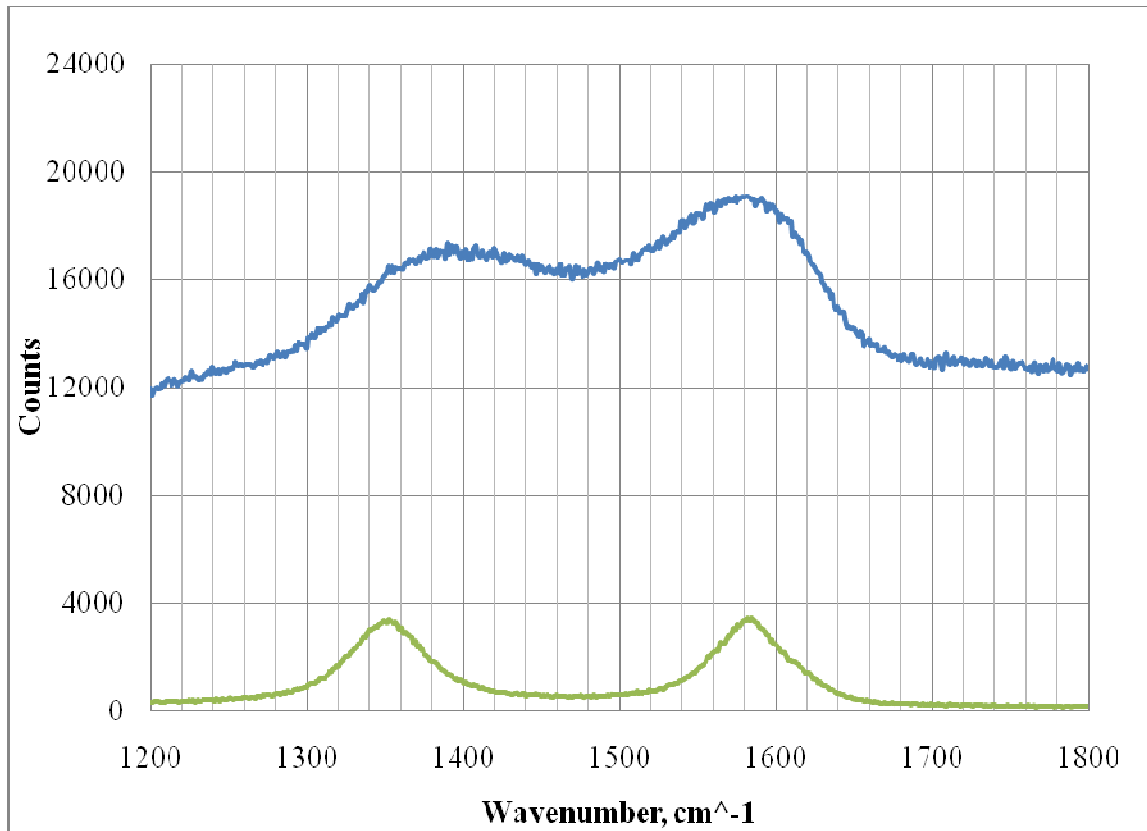


Figure 6: Typical Raman spectra of a laser parameter before (bottom line) and after (top line) cleaning

Figure 7 is a Raman spectrum of the raw ND powder that shows a peak at  $1325\text{ cm}^{-1}$  which can be attributed to nanocrystalline diamond. Other studies have shown a similar peak in a highly purified ND powder using the  $488\text{ nm}$  wavelength at  $1325\text{ cm}^{-1}$  [27]. The Raman analysis of the ND powder in the previously stated reference showed broad humps at  $1200\text{ cm}^{-1}$ ,  $1400\text{ cm}^{-1}$ , and  $1600\text{ cm}^{-1}$  which is similar to the Raman spectrum of the ND powder used in this work. The peaks at  $1200\text{ cm}^{-1}$  and  $1400\text{ cm}^{-1}$  are attributed to amorphous ( $\text{sp}^3$ ) carbon while the peak at  $1600\text{ cm}^{-1}$  is attributed to carbon onions or onion-like carbon ( $\text{sp}^2$ ). The low intensity of the diamond peak in our study is attributed to significant noise formation in the Raman system and 10% impurities present

in the ND powder. To counter the noise effect, laser power can be increased to remove the noise effect but high power can damage the powder.

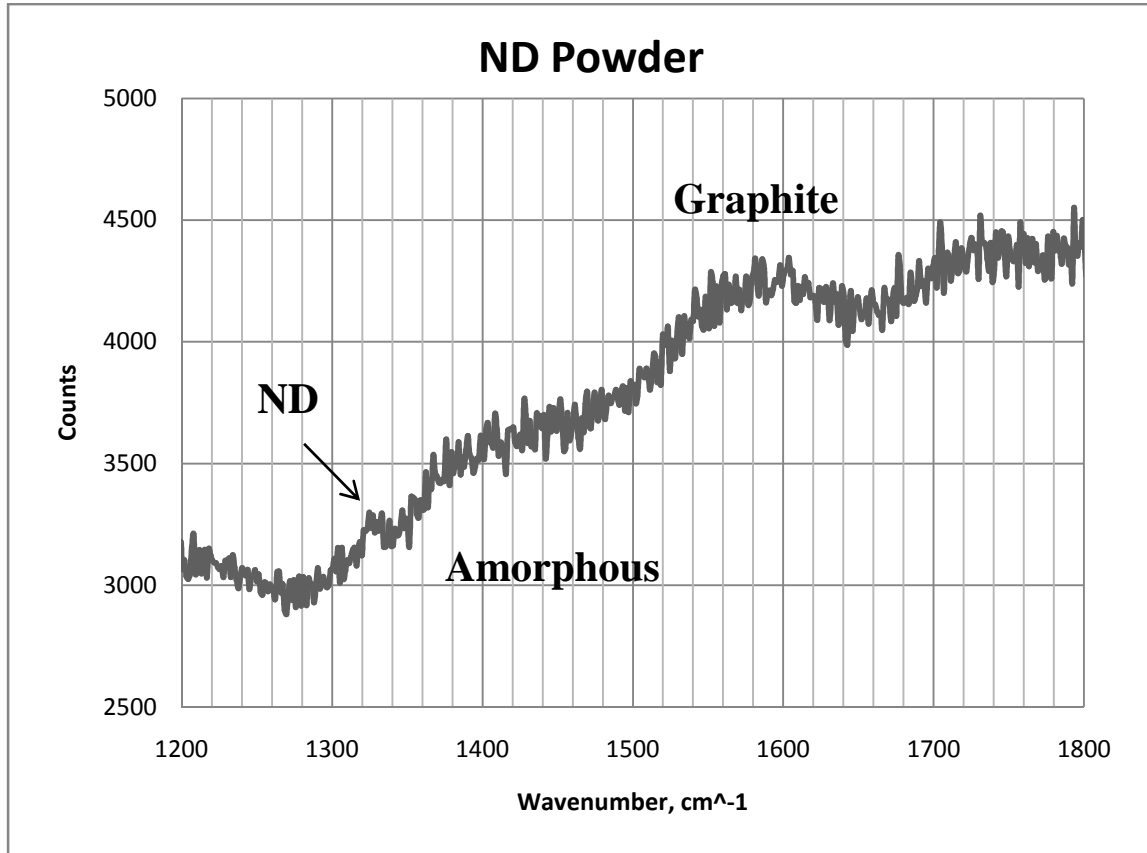


Figure 7: Raman spectrum of ND powder used in this work

Figure 8 shows the Raman spectra of the coupons processed at 1000 W and subsequently ultrasonic cleaned. No diamond peaks corresponding to or in the neighborhood of  $1332\text{ cm}^{-1}$  is seen. However, as described before, it could just be masked by the  $\text{sp}^2$  bonded carbon. Amorphous carbon, and graphite or possibly onion-like carbon (OLC) peaks were observed. DLC occurs at  $1355\text{ cm}^{-1}$ , graphite at  $1580\text{ cm}^{-1}$ , and OLC at  $1572\text{ cm}^{-1}$  [28]. The peak at approximately  $1575\text{ cm}^{-1}$  in our work can be attributed to OLC. OLC consists of closed, concentrically arranged graphitic shells that

belong to fullerenic or curved-layer carbon structures [29]. Its downshift from  $1580\text{ cm}^{-1}$  (pure graphite), is believed to be caused by the curvature of the carbon shell. The combination of amorphous carbon and OLC is believed to have lowered the friction coefficient of the coupon. The variance in scan rate at 1000 W led to a range of unique Raman data. At a scan rate of 169 mm/s (400 in/min), a flat line is observed, suggesting that the ND powder layer was delaminated during laser sintering and coating had been washed away in the ultrasonic bath. At a scan rate of 42 mm/s (100 in/min), the Raman spectrum is identical to that of the raw ND powder. This could mean that there is not enough heat for sintering of ND powder. At a scan rate of 4.2 mm/s (10 in/min), intense diamond-like carbon ( $1355\text{ cm}^{-1}$ ) and graphite ( $1580\text{ cm}^{-1}$ ) peaks are seen. Similar results but with less intensity can be seen in the coupon processed at a scan rate of 2.1 mm/s (5 in/min); this scan rate also caused substantial melting of the coupon.

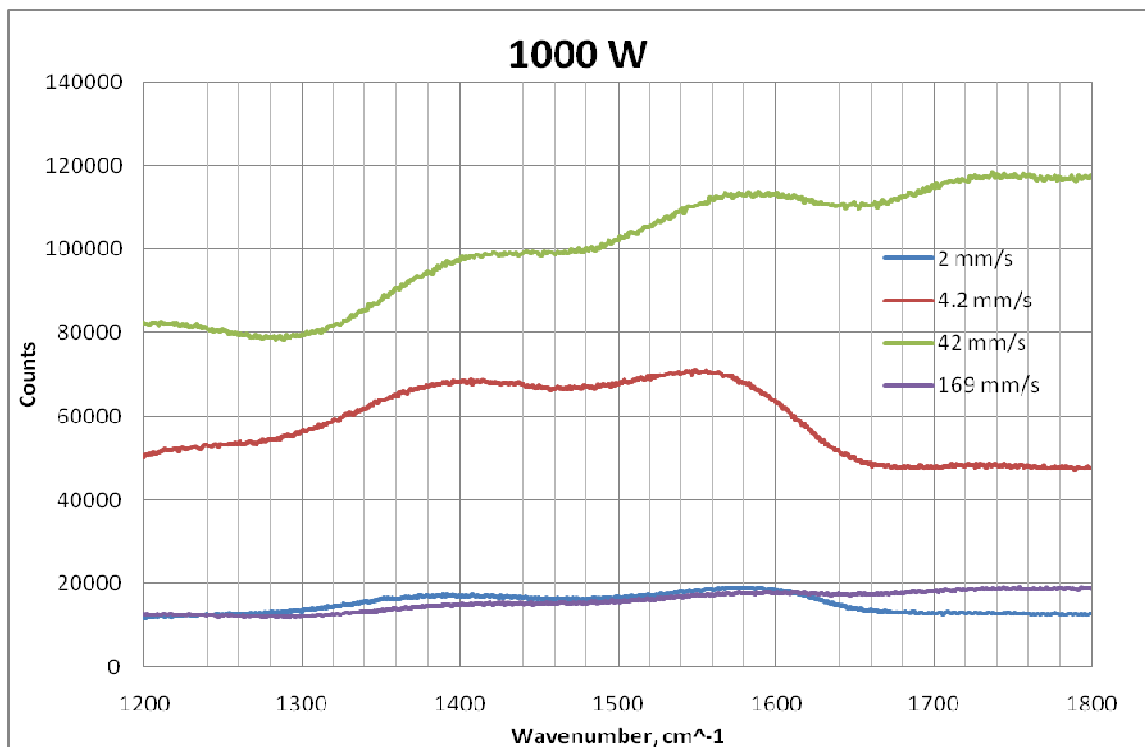


Figure 8: Raman spectra of coupons processed at 1000 W

Figure 9 is a digital photograph of laser-sintered coupon at 1000 W and 4.2 mm/s which seem to be the most optimum in this study. Figure 10 shows the Raman spectra of laser-sintered coupons processed at the optimum laser parameters. Peaks seen at or around  $1360\text{ cm}^{-1}$  and  $1560\text{ cm}^{-1}$  are known as the D and G peaks, respectively [30]. These peaks are primarily due to  $sp^2$  sites, and are broader than the  $1332\text{ cm}^{-1}$  diamond peak. The G peak is from the bond stretching of all pairs of  $sp^2$  atoms in both rings and chains while the D peak is due to the breathing modes of  $sp^2$  atoms in rings [28]. Diamond-like carbon has been shown to exhibit a D peak [30]. The appearance of bands D and G is attributed to the formation of nanocrystalline graphite clusters.

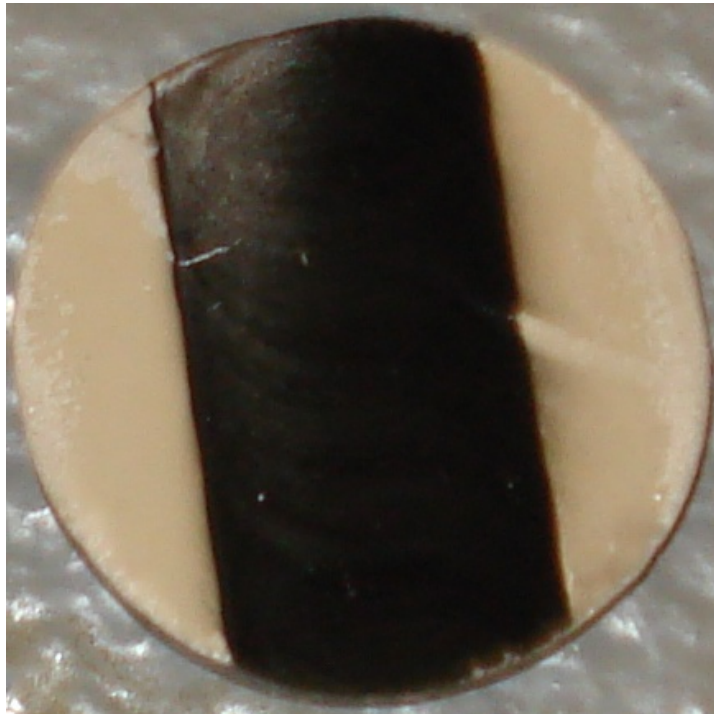


Figure 9: Photograph of laser-sintered coupon (single laser pass in the middle of sample)

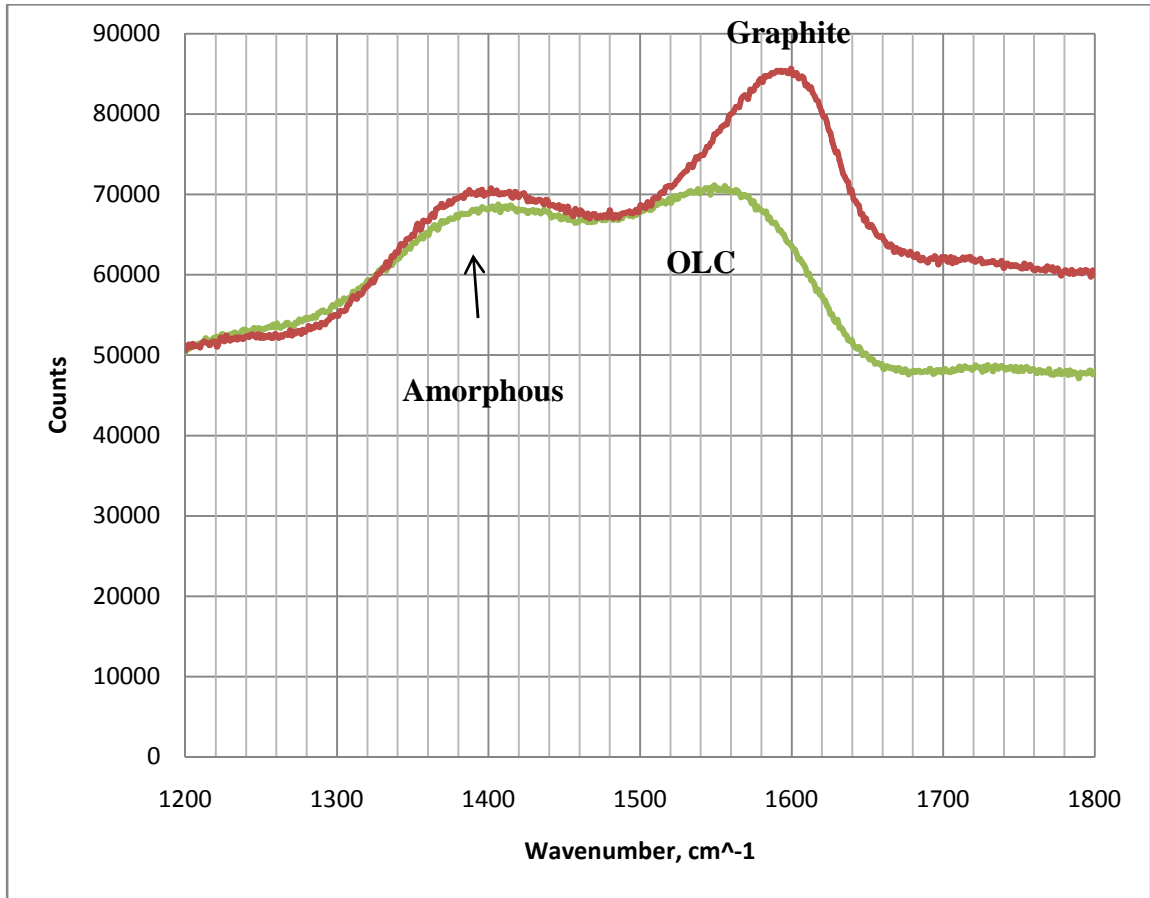


Figure 10: Raman spectra of optimally laser-sintered coupon (1000 W, 4.2 mm/s)

For the optimum laser parameters, the temperature calculations of ring beam showed a maximum surface temperature of about 920 K. The temperature calculation was done using a simple surface temperature calculation for laser radiation as seen below.

$$T_s = \frac{2 * Q_0}{K} * \sqrt{\frac{\alpha * t}{\pi}} + T_0$$

Where  $T_s$  is the surface temperature,  $Q_0$  is the heat source term,  $K$  is thermal conductivity,  $\alpha$  is the thermal diffusivity,  $t$  is the laser interaction time, and  $T_0$  is the initial temperature of the substrate. The heat source term,  $Q_0$ , is equal to:

$$Q_0 = \frac{(1 - R) * P}{\frac{\pi}{4} * (R_o - R_i)}$$

Where R is the reflectivity of the substrate, P is the laser power used,  $R_o$  is the outer radius of the ring beam, and  $R_i$  is the inner radius of the beam. Laser interaction time, t, is equal to:

$$t = \frac{2 * W}{v}$$

Where W is the width of the ring beam and v is the scan rate of the laser. Plugging in the constants seen in Table 6 yielded a surface temperature of 920 K.

Table 6: Aluminum's thermal Properties and laser parameters

Thermal Conductivity, K	1.09 W/cm*K
Thermal Diffusivity, $\alpha$	0.4 cm/K
Reflectance, R	80%
Substrate Initial Temperature, $T_0$	300 K
Laser Power, P	1000 W
Laser scan rate, v	4.2 mm/s
Outer radius, $R_o$	1.27 cm
Inner radius, $R_i$	1.236 cm
Ring beam width, W	0.17 mm

The melting points of diamond and aluminum alloy are 3800 K and 843 K respectively. Studies of the high-temperature transformation of micro- and nano-sized diamond powders revealed a phase transition temperature of 1500-2300 K for micropowders [31-34] and 940 K [25, 33] for nanopowders at ambient pressure. The difference is primarily due to the large surface area-to-volume ratio and the presence of

graphite shell in ND particles. Substantial changes in microstructure and morphology were noted in nanodiamond particles subjected to furnace annealing in argon or oxygen environment [25]. However, according to the phase diagram (Figure 11) of ultra-fine carbon [35], diamond is more thermodynamically stable than graphite particularly when the particle sizes are less than 10 nm.

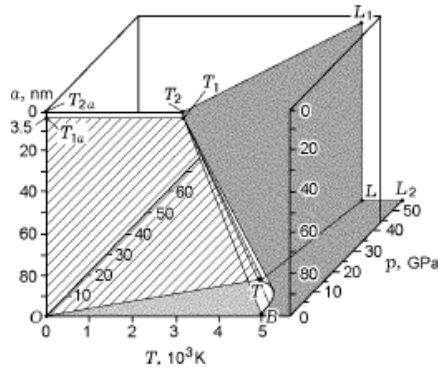


Figure 11: Phase diagram of ultra- fine carbon [35]

The issue of phase transition from nanodiamond to DLC warrants explanation. There are three means by which crystalline diamond can be transformed into DLC: 1) *Melting and rapid quenching of diamond crystals* - Lee *et al.* [36] used molecular dynamics simulations to demonstrate the formation of amorphous structure of carbon by rapid quenching of the melted diamond lattice from 10,000 K at various cooling rates from  $1.25 \times 10^{15}$  K/s to  $6.25 \times 10^{15}$  K/s. This method of phase transition is unlikely in the present work because both temperatures and cooling rates are substantially lower; 2) *Ion beam irradiation* - Reinke *et al.* [37] studied the effects of ion irradiation on the surface structure of polycrystalline diamond using photoelectron spectroscopy and found that a gradual change from diamond to amorphous carbon occurred for certain ion doses. The tendency of diamond surface to amorphize rather than graphitize under ion irradiation is

essentially to do with the type defect structures generated. This type of mechanism is again ruled out in our present work because the laser beam does not exert momentum as ions; 3) *Annealing* – Nistor *et al.* [38] subjected polycrystalline diamond to furnace annealing in vacuum at temperatures of 1623–1723 K and observed the formation of amorphous carbon and/or of well-crystallized graphite layers along the grain boundaries. The diamond-to-graphite transition has occurred in such a way that three (111) diamond planes transformed into two (0002) graphitic sheets. This type of mechanism is probable in our work where the temperatures are quite similar. However, rapid heating and cooling associated with laser sintering will cause diamond transformation to DLC rather than to graphite. Furthermore, the fact that phase transition takes place at the grain boundaries during annealing implies that nanoparticles would provide large number of sites for the formation of amorphous carbon.

### **3.3 Scanning Electron Microscopy and X-ray Diffraction Observations**

Figure 12 shows the SEM micrographs of the top surfaces of both electrostatically spray coated and optimally laser-sintered coupons. Backscattered electron (BSE) imaging was also used to reveal a sharp contrast between the elements in the coating. Electrostatic spray coating consists of significant amount of agglomerates in contrast to

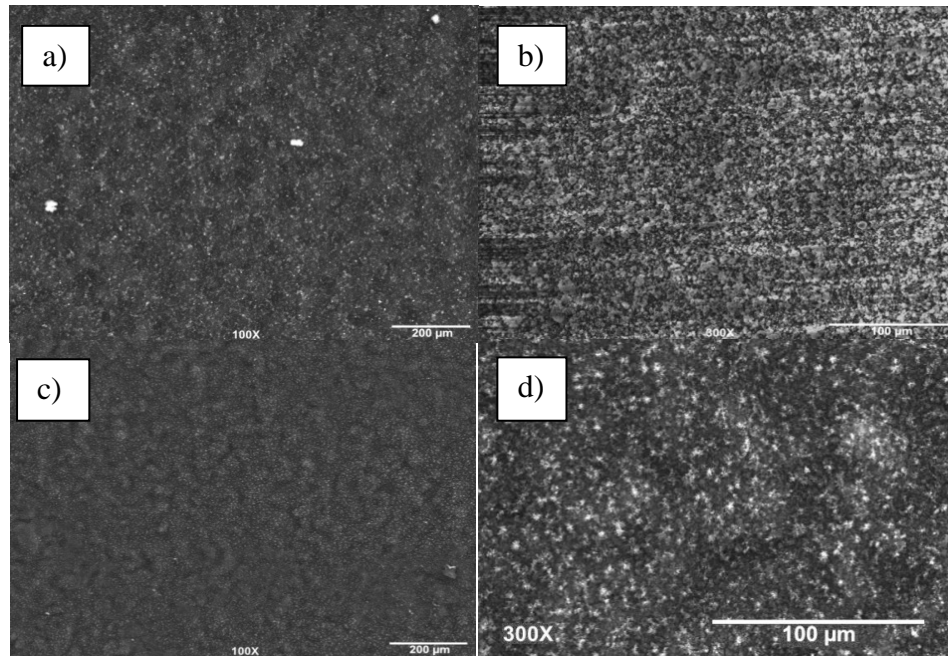


Figure 12: SEM micrographs of ND coated A319 coupons: a) and b) electrostatically spray coated; c) and d) laser-sintered

the laser-sintered coupon. The chemical makeup of the coating is a mixture of carbon and aluminum based on the contrasting features in BSE image and EDX analysis (Figure 13). As expected, the electrostatic spray coating consists of primarily carbon and some oxygen. However, the laser-sintered coupon exhibits a composite of aluminum and carbon. Figure 14 is a transverse section showing the composite coating for a thickness of 60  $\mu\text{m}$ . The creation of this layer is accomplished through three mechanisms. First, the molten aluminum is pulled up through the nanodiamond powder by capillary forces. The capillary forces occur because the molten aluminum dampens the nanodiamond powders making the space between diamond particles act as a capillary. Second, the nanodiamond powder is more dense than the molten aluminum thus allowing the powder to disperse down into the aluminum due to gravity. Third, the impurities within the nanodiamond powder (Ca, Fe, Cu, Al, Cr, and Si) are being sintered together during the laser

sintering process. X-ray diffraction pattern, shown in Figure 15, confirms the presence of DLC at a  $2\theta$  peak  $26.61^\circ$ . Diamond (111) exhibits a peak at  $43.62^\circ$  and cannot be seen in XRD analysis but there is a strong peak at  $44.42^\circ$  that could be ascribed to some disordered form of carbon. The remaining peaks belong to aluminum.

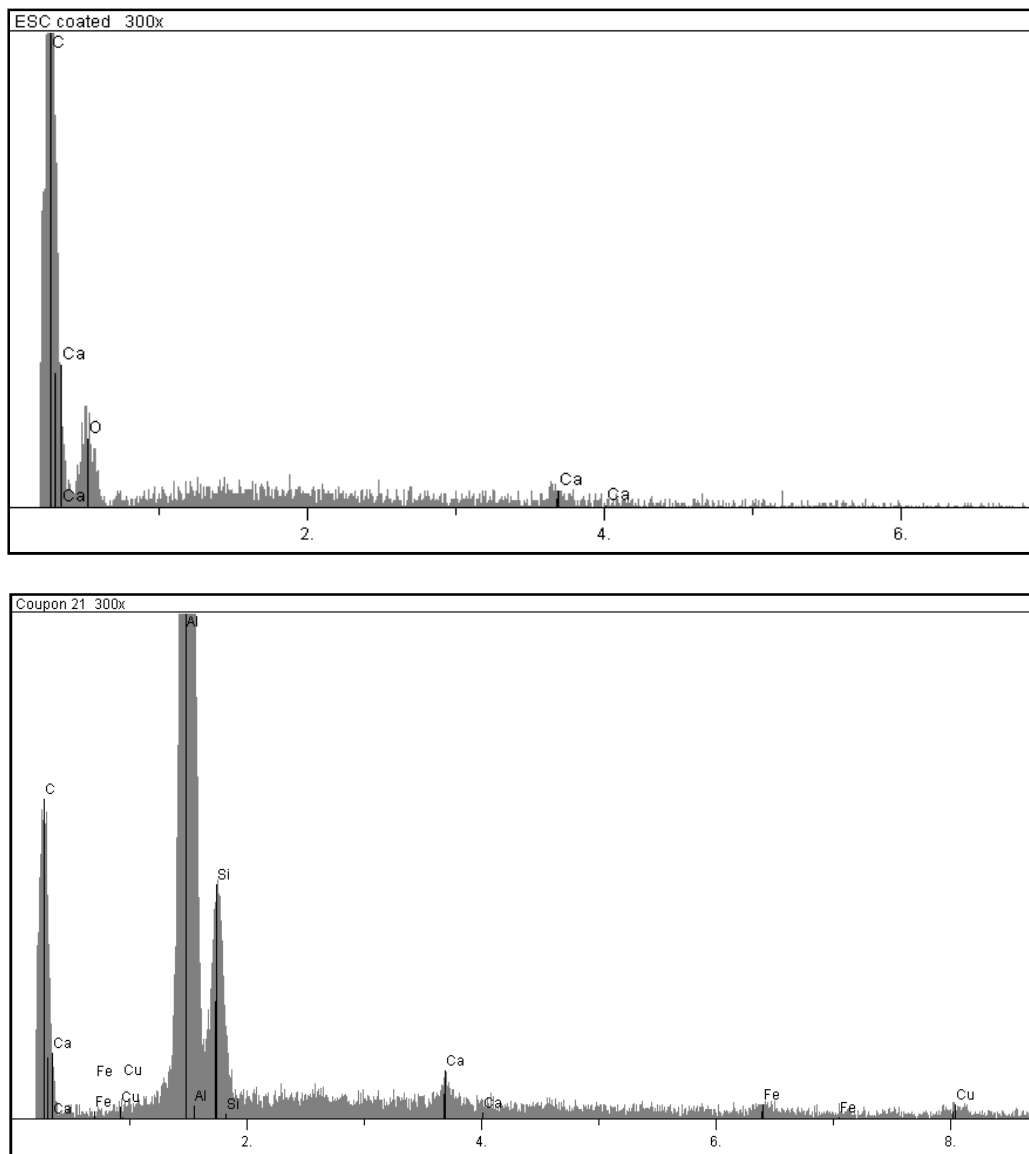


Figure 13: EDX analysis: (Top) electrostatically spray coated coupon; (Bottom) laser-sintered coupon

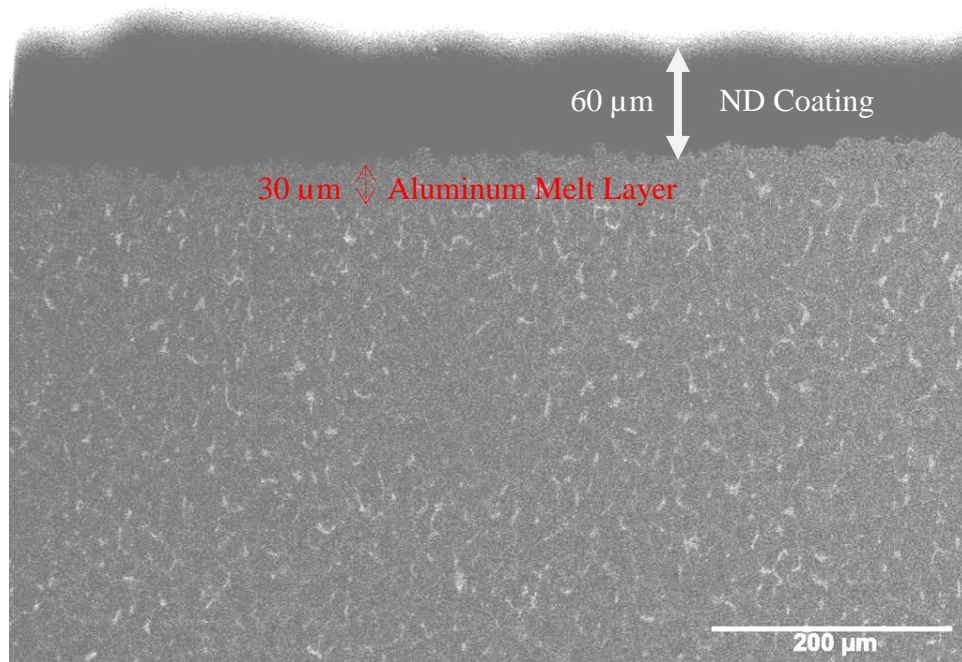


Figure 14: SEM image of the transverse section of laser-sintered coupon

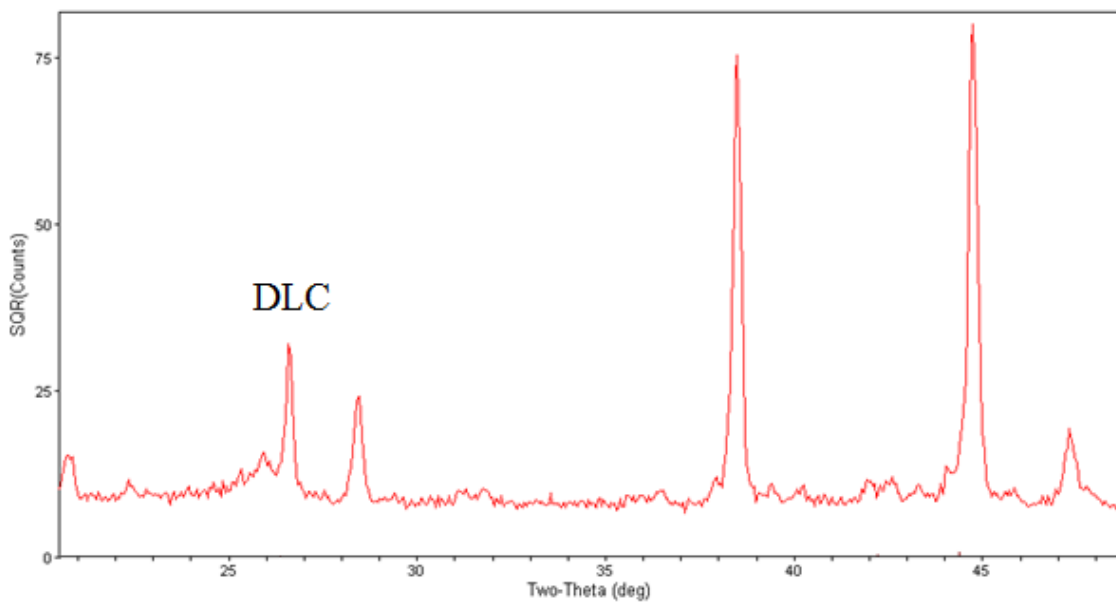


Figure 15: XRD pattern of the laser-sintered coupon

Laser sintering of ND powder involves several physical phenomena including energy absorption, heating and densification of the powder, aluminum (binder) melting,

and sintering of nanoparticles. Multiple scattering occurs within the electrostatically coated powder and assists in a nearly homogeneous absorption of the radiation in the powder. Densification is mostly completed in the solid state based on the report that the onset of sintering temperature in laser sintering of nanopowders is 0.2-0.3  $T_m$  as compared to 0.5-0.8  $T_m$  for microscale powders where  $T_m$  is the melting temperature [39]. The process then becomes liquid-phase laser sintering when ND particles are dispersed in a thin molten pool of aluminum. Here the laser energy was used only to raise the temperature of aluminum binder to melt and flow through the diamond particles by driving forces such as the liquid pressure, viscosity and capillary forces through the pores between the solid particles. With its high surface tension, the molten aluminum wetted the diamond particles and thus the process produced dense layers by the *in-situ* filtration mechanism.

Dahorte et al [40] deposited fine FeO powders on aluminum A319 (engine cylinders) and then subjected them to laser surface treatment with a 1.5 kW continuous wave Nd:YAG laser at 58 mm/sec such that a thin layer of Al substrate melted and mixed with FeO due to the convection currents within the melt zone. The coating exhibited a refined dendritic microstructure (5  $\mu\text{m}$ ) compared to the cast substrate structure (50  $\mu\text{m}$ ). Also there were no cracks or delamination within the laser-melted zone and along the interface between the coating and the substrate implying the existence of a strong metallurgical bond.

### 3.4 Surface Roughness

Surface roughness measurements were taken on bare aluminum, electrostatically spray coated and optimally laser-sintered coupons so that the values could be compared.

Three randomly selected sites were chosen on each coupon. Figure 16 shows the surface morphology of the bare, electrostatically spray coated and laser-sintered coupons along with the roughness profile. A comparison of three surfaces (Figure 17) show that laser-sintered coupon has the smoothest surface with an average roughness of  $1.54 \mu\text{m}$  partly attributed to the ring beam. Dahorte et al reported a surface roughness of  $4.75 \mu\text{m}$  (Ra) in Nd:YAG laser (focused circular beam) surface engineered FeO on A319 aluminum [40].

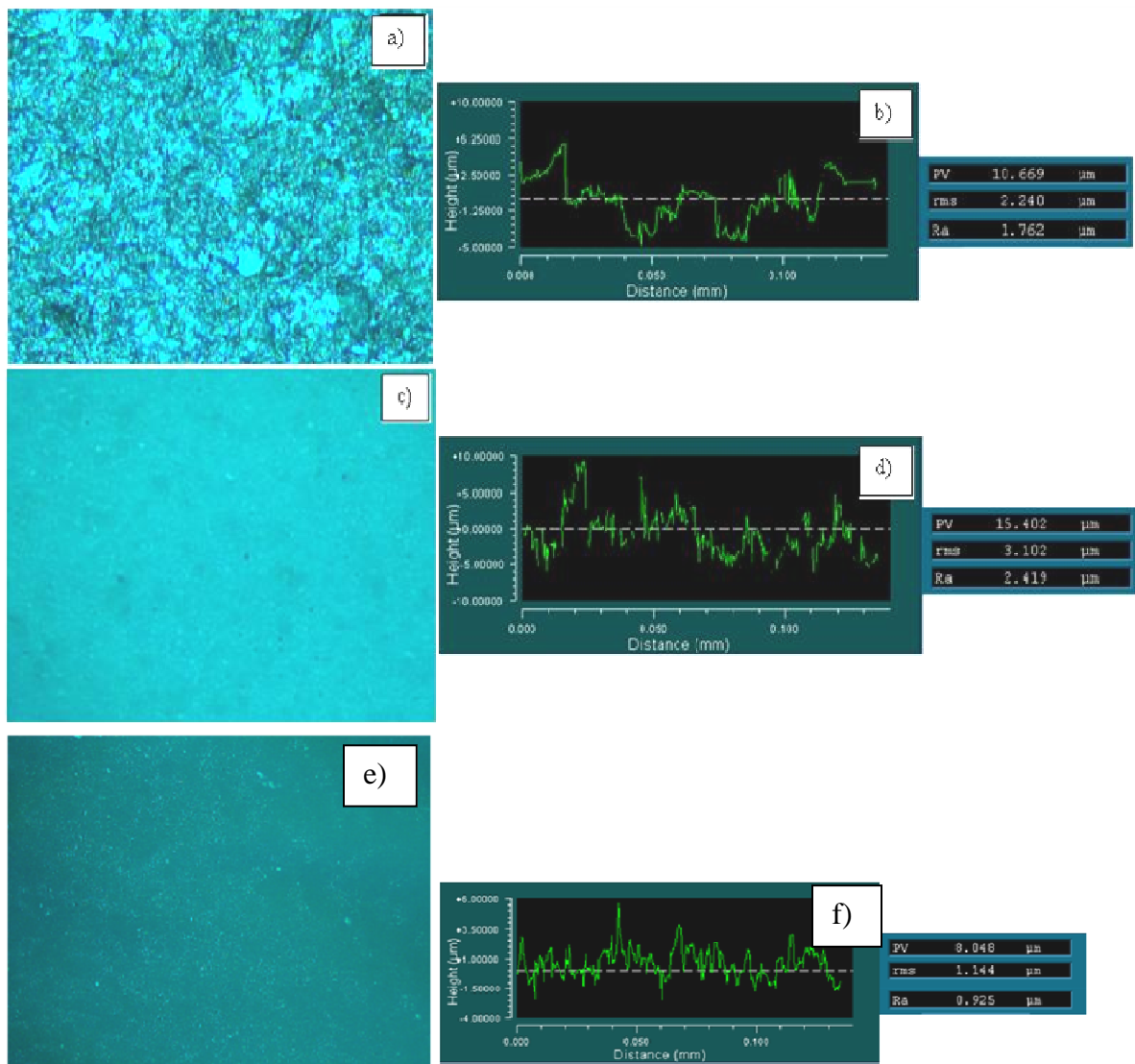


Figure 16: Optical image and roughness profile of: a) and b) bare aluminum surface c) and d): electrostatically spray coating, and e) and f) laser sintered coating

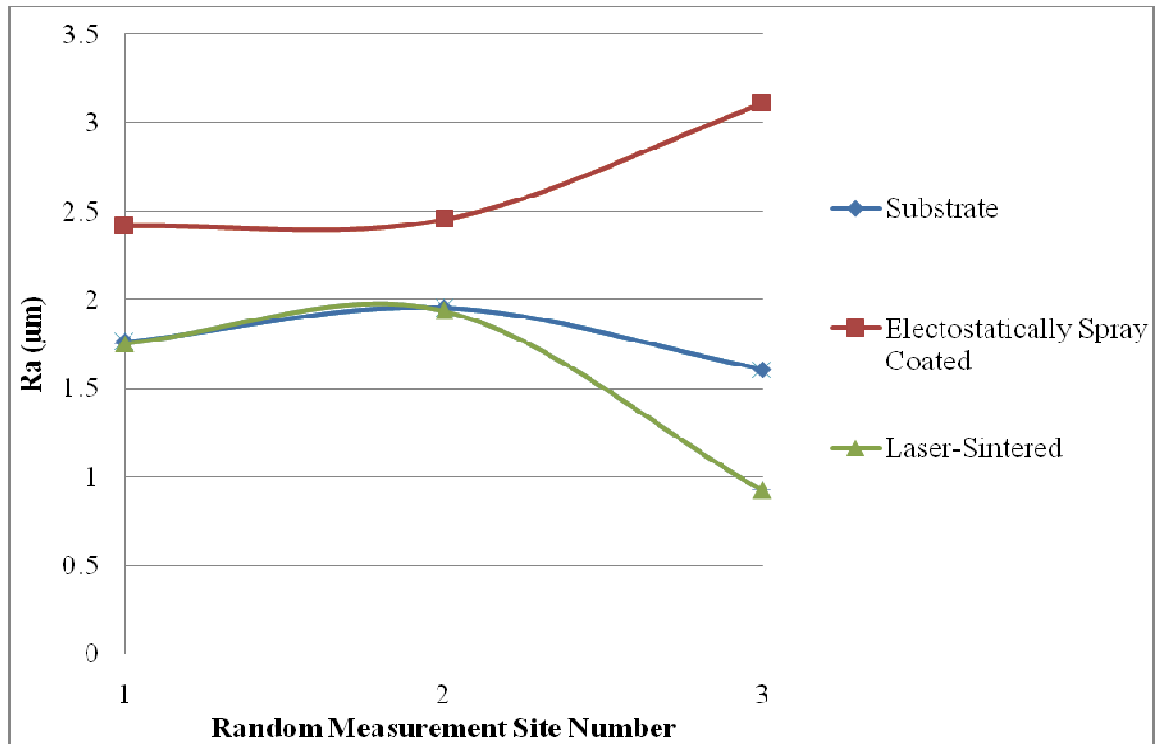


Figure 17: Comparison of surface roughness

### 3.5 Nanoindentation

Nanoindentation hardness and elastic modulus data were recorded with several indentations made on the surface of the laser-sintered coupon using Berkovich indenter tip. Indentations were made using a force of 4000  $\mu\text{N}$  and 8500  $\mu\text{N}$ . These forces made indentation depths ranging from 227-383 nm for 4000  $\mu\text{N}$  and 334-629 nm for 8500  $\mu\text{N}$ . The wide range of depths observed can be attributed to the varying hardness of the surface. Some tests led to the fracture of the some areas through the formation of chips. This type of test giving unacceptable force plot can be seen in Figure 18a. After each indentation, the force plot was evaluated for acceptability. Figure 19 shows an AFM image of one of the indentations made on the laser-sintered coupon. Based upon a large

number of acceptable tests, laser- sintered coupon had a hardness range from 0.8 to 2.7 GPa. Young's modulus also ranged from 30-103 GPa. The differences in hardness and

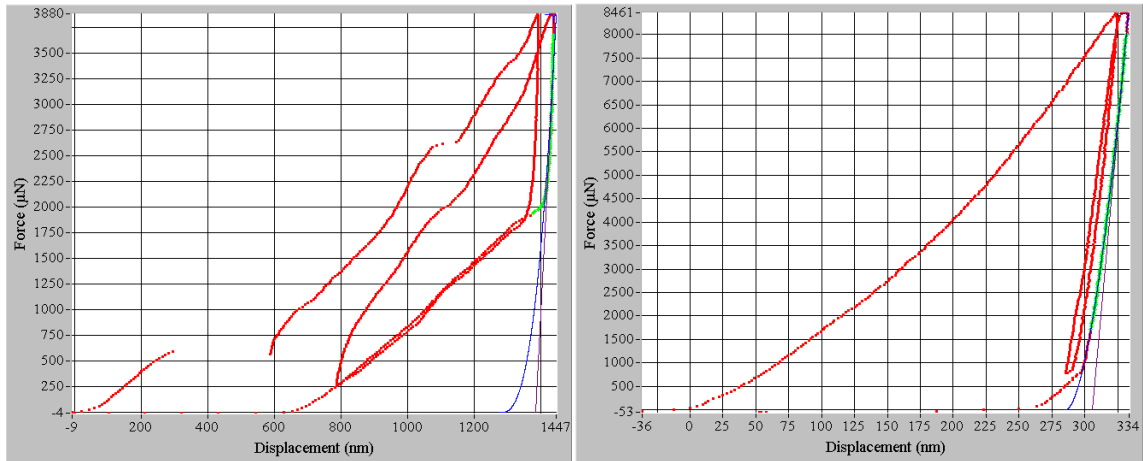


Figure 18: a) (Left) Bad force plot due to surface breakage b) (Right) Example of an acceptable force plot. Both plots are from the laser-sintered coupon

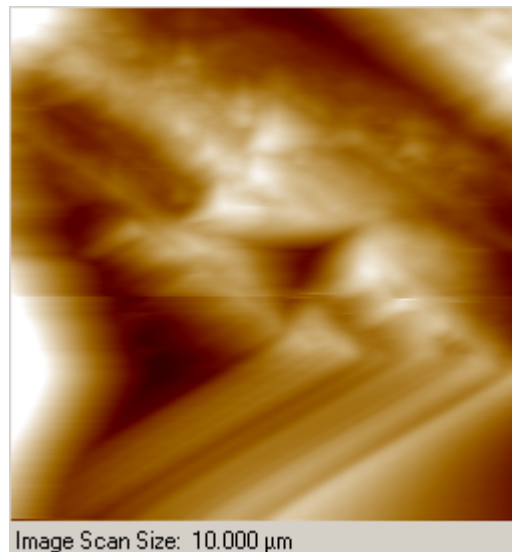


Figure 19: AFM image of nanoindentation on the laser-sintered coupon

Young's modulus values are attributed to the differences in chemical makeup and microstructure of the coating. Figures 20 and 21 show the distribution of hardness and Young's modulus respectively. Dahorte et al reported a nanoindentation hardness of 1.78

GPa for laser remelted/FeO coated aluminum [40]. However, the elastic modulus remained unchanged at about 80 GPa, implying that the hardness was only sensitive to microstructural and chemical changes. Similarly laser surface melting and subsequent rapid solidification of 700  $\mu\text{m}$  layers of A319 alloy led to an increase in nanoindentation hardness from 0.8 GPa to 1.22 GPa [41]. Again, Young's modulus remains unchanged at 75 GPa.

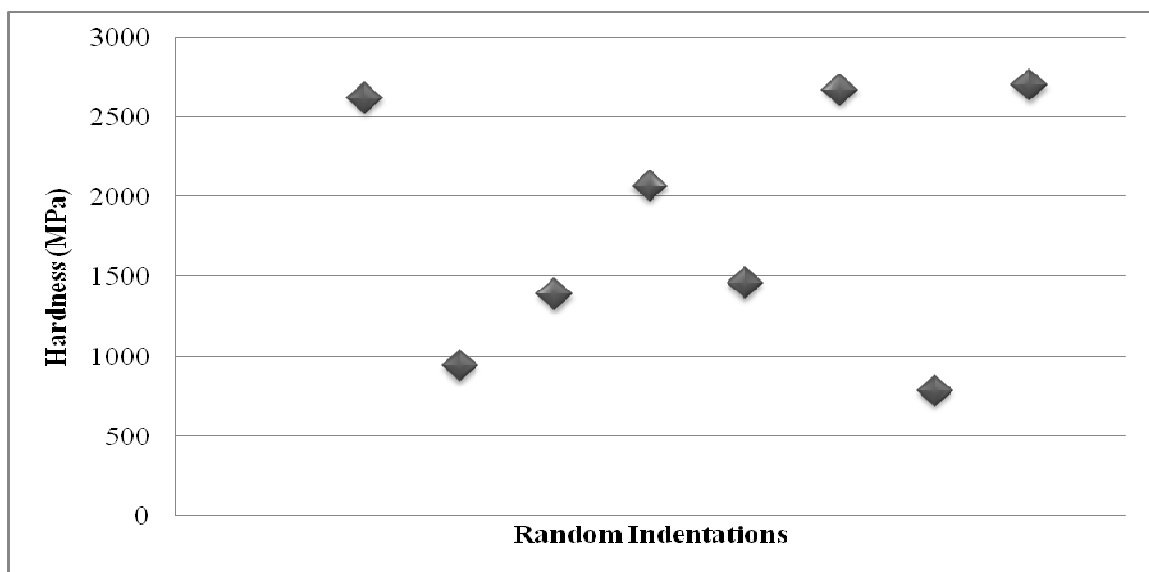


Figure 20: Distribution of nanohardness values in laser-sintered coupon

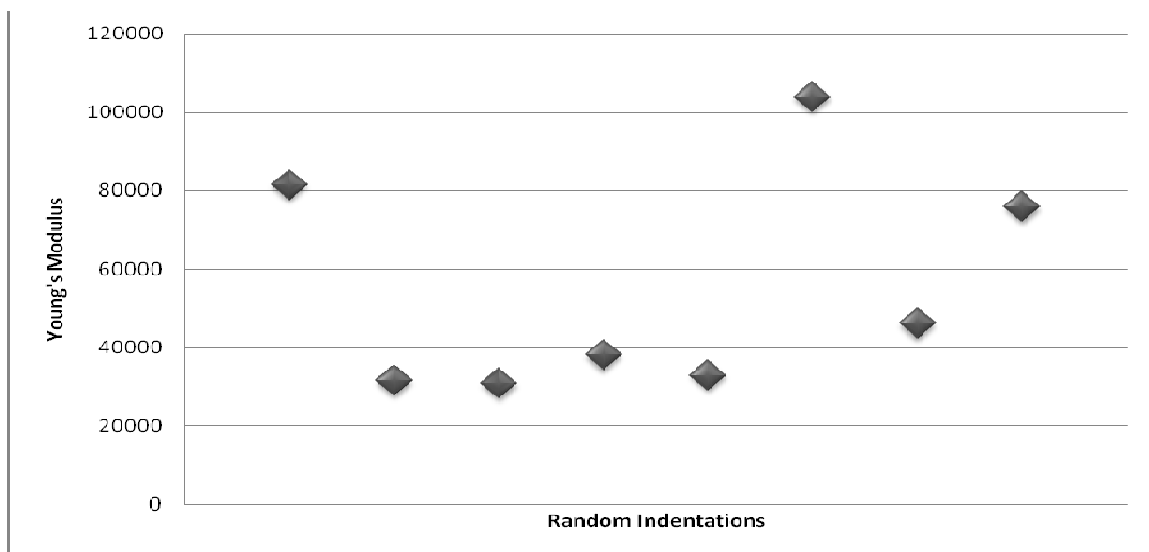


Figure 21: Distribution of Young's modulus values in laser-sintered coupon

### 3.6 Friction and wear

Figures 22 and 23 along with Table 7 present the results of dry friction and wear tests of bare aluminum (uncoated) and laser-sintered aluminum (coupon # 21). For the bare aluminum, the coefficient friction is varying significantly while it remains steady for the laser-sintered coupon.

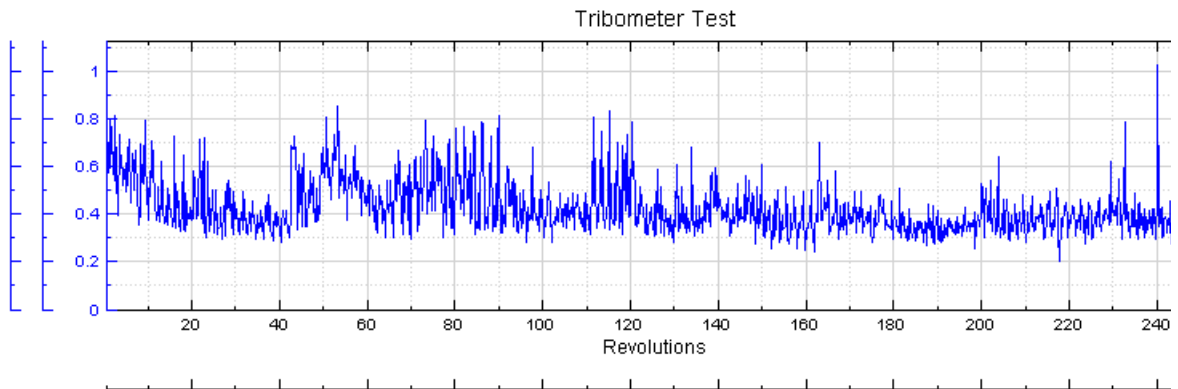


Figure 22: Friction of 319 aluminum substrate against 440C steel

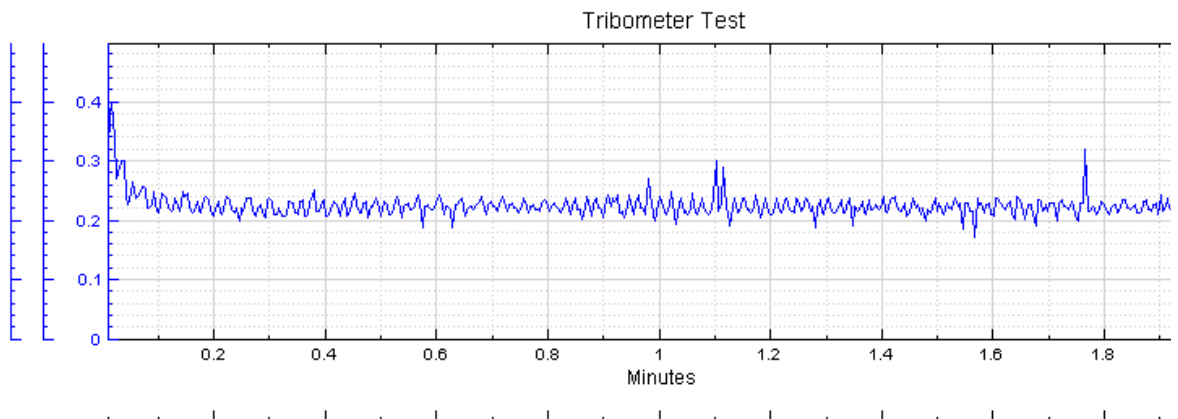


Figure 23: Friction of laser-sintered coupon against 440C steel

Table 7: Comparison of coefficient of friction and wear rate

	Average COF	Minimum COF	Maximum COF	Area of Wear Track ( $\mu\text{m}^2$ )	Wear Rate ( $10^{-3}$ $\text{mm}^3/\text{Nm}$ )
<b>Laser-Sintered</b>	0.226	0.172	0.399	1506.25	3.009
<b>Bare Aluminum</b>	0.425	0.200	1.028	14823.0	11.85

The most remarkable result is the low coefficient of friction that is attributed to the solid lubricating nature of ND coatings. Friction could have been even lower if a counterface material other than steel were chosen because of the chemical affinity between diamond and steel. Luo et al reported that the relatively high frictional force of diamond against steel was attributed to the attraction of graphitic dangling bond by 3d orbitals of Fe [42]. Malaczynski et al found that A390 samples coated with DLC had a coefficient of friction of about 0.4 [43], twice that of the present work. Among many theories proposed to explain the friction and wear behavior of diamond films, the most accepted one is the formation of a friction-induced transfer film on the counterface that acts like a lubricating film [44-46]. For example, in the friction test of DLC against steel under 100% dry nitrogen environment, a carbon rich layer is formed on the steel counterface, reducing the friction coefficient to 0.035 [47]. Similarly Liu et al. reported that the low friction of DLC films in the steady state was due to the wear-induced graphitization [48]. However, in the oxygen environments, the friction-induced chemical reactions among the diamond, steel ball and oxygen would prevent the formation of the transferred carbon rich layer on the steel ball and result in higher friction coefficient (more than 0.2) [47]. Another use of ND powder is that it is added to oil to act as a lubricant. Studies have shown that ND particles in oil do reduce friction due to three mechanisms [49]. The first mechanism is that the ND particles act like ball bearings changing the sliding motion into a rolling motion. Second, the ND particles plow both contact surfaces causing smoother surfaces thus reducing friction. The third mechanism is the ND particles form a film on surface irregularities creating a smoother surfaces thus reducing friction [49]. The reduction in friction observed in this work can also be explained by the first two mechanisms. The

presence of the curved shells of OLC could act like ball bearing creating a rolling motion instead of the sliding motion, reducing the friction between the coupon and ball in the test. The ND particles on the surface of the aluminum could be plowing at the surface of the ball causing a reduction in friction. However, the images of the wear tracks (Figure 26) do show some deformation on the surface of the coupon.

Wear data shows that the wear rate is decreased by four times in laser-sintered coatings over the bare aluminum, indicating the beneficial effects of the hard coating and microstructure of laser-melted aluminum. Dahorte et al used block-on-disk tribometer tests to evaluate the wear characteristics and showed that laser refined/FeO coated 319 alloy decreased the wear rate by 71% over uncoated alloy despite only a marginal increase in hardness [40]. The wear tracks (Figures 24 and 25) show that laser-sintered coupon has a much smoother (peak-to-valley distance) surface as compared to the bare aluminum coupon. This is similar to Dahorte et al's work who reported that the worn FeO-coated sample was smoother (3.85 Ra) than the worn A319 Al (5.64 Ra) sample surfaces [40]. Lee et al investigated the effect of ND addition on the tribological behavior of polytetrafluoroethylene (PTFE) film and reported that the coefficient of friction and width of wear track changed from 0.21 to 0.16 and 0.85 to 0.44 mm, respectively, when 2 wt.% of nanodiamond was added to PTFE [50].



Figure 24: Wear track profile of 319 aluminum substrate against 440C steel

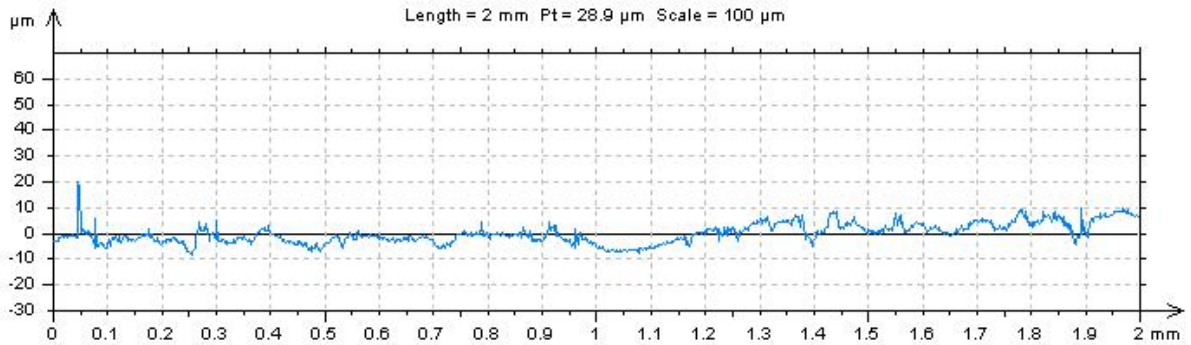


Figure 25: Wear track of laser-sintered aluminum against 440C steel

Figure 26 shows the optical micrographs of the wear tracks. The bright regions are reflective of the worn surfaces while the darker parts were either not worn or less worn during the test. It may be noted that the area fraction of the bright regions is larger for bare aluminum. The wear mechanism in uncoated A319 was proposed by Dahorte et al [40] as consisting of breaking, detaching and falling of hard asperities and hard eutectic mixture from the surface and subsurface regions leaving behind pits/voids followed by the plastic deformation of a highly ductile matrix to generate leaps and folds. Wang et al conducted wear tests of as-cast Al-20% Si alloys and noted extensive fracture of Si phases and large degree of deformation of the matrix [51]. Thus the wear mechanism in bare aluminum appears to be delamination. In contrast, laser-sintered coupons underwent tribochemical wear. Figure 27 shows the SEM micrograph of wear track of laser-sintered coupon showing some debris on the worn surface. EDX analysis revealed that the debris consisted mostly of C, O, and Al (Figure 28). There is no transfer of Fe from the counterface steel to the diamond coating unlike noted in another study [47]. It appears that wear proceeds mainly by the formation and spallation of chemical layer in the worn surface, suggesting that tribochemical wear is the dominant wear

mechanism. However, X-ray photoelectron spectroscopy analysis is deemed necessary to confirm the wear mechanism.

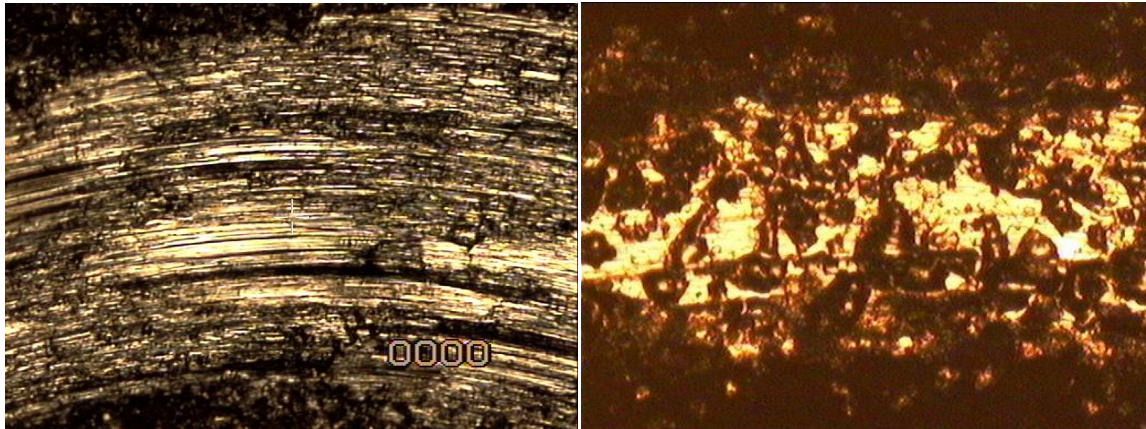


Figure 26: Optical micrographs of wear tracks at 50x magnification (Left) Bare aluminum (Right) Laser-sintered coupon

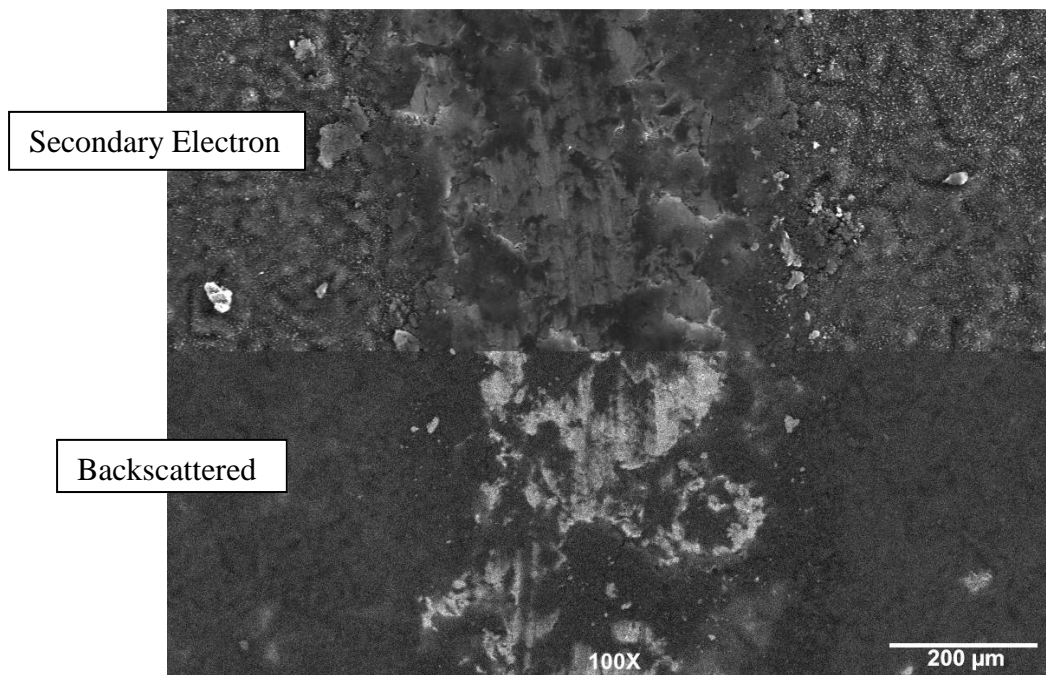


Figure 27: SEM images (backscattered and secondary electron) of wear track of laser-sintered coupon

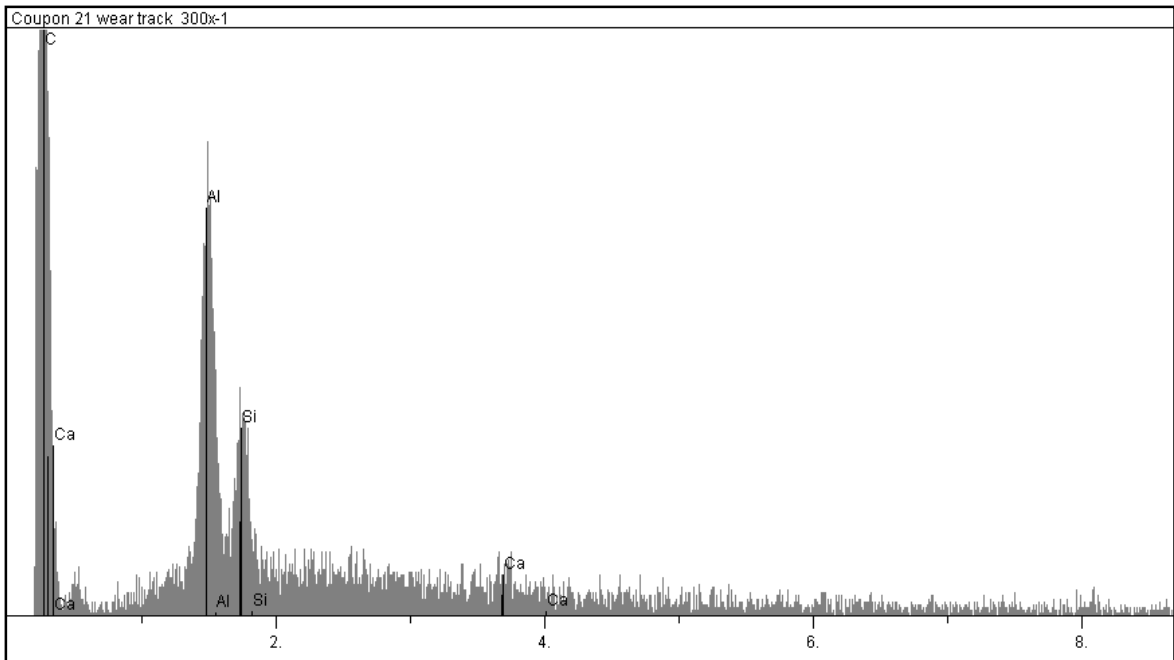


Figure 28: EDX analysis of wear track of laser-sintered coupon showing that there is no iron meaning that particles from the steel ball did not transfer to the coupon

### Conclusion

A novel CO<sub>2</sub> laser sintering method of nanodiamond powder was investigated to enhance the tribological properties of aluminum through the formation of thick, adherent ND coatings. A number of interesting results was obtained. Laser power and beam scan rate critically affect the formation of ND coatings. Ring shaped laser beam provided the thin melt layer of aluminum for bonding ND coatings while generating smoother surfaces than the bare aluminum substrate. The coatings were substantially thicker (60 μm) than achievable by traditional CVD/PVD methods. The wide variation in hardness and Young's modulus and solid lubricating nature of the coating enabled significant reduction in wear and friction of aluminum against steel counterface in dry, ambient environment. This work can be applied to lightweight components used in internal combustion engines,

biomedical implants, magnetic hard disks, cutting tools and polymeric parts for reducing the energy loss associated with friction and improving wear resistance.

### Acknowledgements

The authors would like to thank the National Science Foundation for the Grant 0738405. We also appreciate Dr. Anatolli Frishman for providing the nanodiamond powder, Dr. Wenping Jiang for electrostatic spray coating of our samples and providing the information on the setup, and Mr. Hal Salisbury and Vitalli Brand for their help in characterizing the coated surfaces.

### References

1. K. Funatani et al., *Automot. Eng.*, (1995), 15-20.
2. H.L. MacLean and L.B. Lave. *Pror. Energy Combust. Sci.* 29, (2003), p.1
3. *Automotive News Market Data Book*, 1990
4. I. J. Smith, T. Hurkmans and A. Hieke "The Use of PVD Coatings for Weight Reduction in Automotive Weight Reduction in Automotive Applications" <http://www.iom3.org/divisions/automotive/lwv6/ses3pres6.pdf>, Lean Weight Vehicle Conference , (2003)
5. Funatani, K. et al., *SAE International Congress & Exposition*, (1994), 82-96
6. S.S. Lin, D.J. Patterson, *SAE Paper No.-930794*, (1993), 129
7. V.D.N. Rao, D.M. Kabat, D. Yeager, B. Zizitter, *SAE Paper No.-970009* (1997)
8. W. Kimberly, "Coatings to improve performance," *Automotive Engineer*, London, England <http://www.autofieldguide.com/columns/0506euro.html>
9. S. Kunioka, *Society of Automotive Engineers of Korea*, 2000 FISITA Word Automotive Congress, (2000), 1-6.
10. Y. Wang and S.C.Tung, *Wear*, 225-229, (1999), 1100-1108.
11. M. Kubo, *SAE paper 830252*, (1983)
12. G. Wuest et al., *SAE International Congress & Exposition*, (1997), 33-43
13. V.D.N. Rao et al., *SAE International Congress & Exposition*, (1997), 107-132.
14. V.D.N. Rao et al., *SAE International Congress & Exposition*, (1997), 57-67
15. D.R. Marantz et al., *29th International Symposium on Automotive Technology and Automation*, 1, (1996), 723-729
16. L. Li, X. Tian, P. Chu, Y. Zhang, X. Cui, H. Zhang, *Nucl. Instrum. Meth. B*, 206, (2003), 691
17. J. Liao, L. Xia, M. Sun, W. Liu, T. Xu and Q. Xue, *Surf. Coat. Technol.*, 183, (2004), 157
18. Y.Oka, M.Tao, Y. Nishimura, K. Azuma, E. Fujiwara, M. Yatsuzuka, *Nucl. Instrum. Meth. B*, 206, (2003), 700

19. S. Aisenberg and R. Chamot. *J. Appl. Phys.* 42 6 (1971), p.2953
20. K.L. Choy, *Prog. Mater. Sci.*, 48, (2003), 57-170
21. S. Zhang, X.L. Bui and Y. Fu, *Surf. Coat. Technol.*, 167, 2–3, (2003), 137
22. S. Zhang, Y. Fu, H. Du, X.T. Zeng and Y.C. Liu, *Surf. Coat. Technol.*, 162, 1, (2002), 42
23. W. Ni, Y. Cheng, A. Weiner and T. Perry, *Surf. Coat. Technol.*, 201, 6, 4, (2006), 3229
24. N. Dahorte and S. Nayak, *Surf. Coat. Technol.*, 194, 1, (2005), 58
25. N.S. Xu, J. Chen and S.Z. Deng, *Dia. Rel. Mater.*, 11, (2002), 249–256
26. S. Praver, K.W. Nugent, D.N. Jamieson, J.O. Orwa, L.A. Bursill and J.L. Peng, *Chem. Phys. Lett.*, 332, (2000), 93-97
27. A.C. Ferrari and J. Robertson, *Phil. Trans. R. Soc. Lond. A*, 362, (2004), 2477-2512
28. E. D. Obraztsova, M. Fujii, S. Hayashi, V. L. Kuznetsov, Yu. V. Butenko and A. L. Chuvilin, *Carbon*, 36, (1998), 821-826
29. A. V. Gubarevich, J. Kitamura, S. Usuba, H. Yokoi, Y. Kakudate, O. Odawara, *Carbon*, 41, (2003), 2601-2606
30. A.C. Ferrari, J. Robertson, *Phys. Rev.-B*, 64, (2001), 075414-1-13
31. M. Seal, “Graphitization of Diamond” *Nature*, 185, (1960), 522
32. T. Evans and P. James, *Proc. R. Soc. Lon. Ser.-A, Mathematical and Physical Sciences*, 277, 1369, (1964), 260
33. J. Qian, C. Pantea, J. Huang, T. Zerda, Y. Zhao, *Carbon*, 42, (2004), 2691
34. J. Wang and G. Yang, *J. Phys.-Condens. Mat.*, 11, 37, (1999), 7089
35. A. Vereshchagin, *Combust. Explo. Shock +*, 38, 3, (2002), 358
36. S. Lee, K. Lee and J. Lee, *Nanotech, Vol. 2, Technical Proceedings of the 2002 International Conference on Computational Nanoscience and Nanotechnology*, (2002), 466
37. P. Reinke, G. Francz, P. Oelhafen, J. Ullmann, *Phys. Rev. B*, 54, 10, (1996), 7068
38. L. Nistor, V. Ralchenko, I. Vlasov, A. Khomich, R. Khmel'nitskii, P. Potapov and J. Van Landuyt, *Phys Status Solidi A*, 186, 2, (2001), 207
39. H. Zhu and R. Averback, *Phil. Mag. Lett.*, 73, 1, (1996), 27
40. N. B. Dahotre, S. Nayak, and O. Popoola, *J. Met.*, (2001), 44
41. S. Nayak and N. B. Dahotre, *J. Met.*, (2004), 46
42. S. Luoa, J. Kuo, B. Yeh, J. C. Sung, C. Dai and T. Tsai, *Mater. Chem. Phys.*, 72, (2001), 133
43. G. W. Malacynski, A. H. Hamdi, A.A. Elmoursi, X. Qiu, *Surf. Coat. Technol.*, 93, (1997), 280-286
44. C. Donnet, *Surf. Coat. Technol.*, 100–101, (1998), 180
45. E.S. Yoon, H. Kong, K.R. Lee, *Wear*, 217, (1998), 262
46. D.S. Kim, T.E. Fischer, B. Gallois, *Surf. Coat. Technol.*, 49, (1991), 537
47. H. Li et al., *Appl. Surf. Sci.*, 249, (2005), 257–265
48. Y. Liu, A. Erdemir, E.I. Meletis, *Surf. Coat. Technol.* 94–95, (1997), 463
49. M. Shen, J. Luo, S. Wen, *Tribol. T.*, 44, 3, (2001), 494-498
50. J. Lee and D.Lim, *Surface & Coatings Technology* 188–189, (2004), 534– 538

51. F. Wang, Y. Ma, Z. Zhang, X. Cui and Y. Jin, Wear, 256, (2004), 342-345

#### CHAPTER 4. General Conclusions and Future Work

In this research project, we have successfully demonstrated a novel technique, laser-induced phase transition and sintering of nanodiamond (ND) powders, to generate ND/DLC or composite ND/DLC/Al coatings on aluminum substrates. The coatings are strongly adherent due to the formation of a thin melt layer that can be seen in the SEM images of the sample. Helping to form this thin melt layer are the active sites exhibited by the nanoparticles. The active sites enabled better laser energy absorption, low temperature sintering and phase transition. The two laser beam configurations, focused round beam and ring beam, used in this research yielded varying results. The focused round beam created a unique composite coating (75  $\mu\text{m}$  thick) consisting of alternating layers (each layer 100  $\mu\text{m}$  width) of ND/DLC with a diffused interface and microstructure-refined aluminum. The composite coating exhibited two times lower friction, three to six times higher hardness, and a sliding wear resistance over five times greater than that of the aluminum substrate. The ring beam created a ND/DLC coating with a nominal thickness 60  $\mu\text{m}$  and a sharp interface with the substrate. The ND/DLC coating exhibited two to three times lower friction, two to three times higher hardness, and four times higher sliding wear resistance than the aluminum substrate.

The competing processes for our laser coating technology include ion beam deposition (IBD), magnetron sputter deposition (MSD), plasma-enhanced CVD (PECVD), anodizing, electroplating etc. Some of the important characteristics of coatings are coating thickness, adherence, substrate temperature, deposition rate, lubrication, strong affinity for oil, and corrosion resistance. Comparing our laser sintering process to these other processes, we find that the competing process are limited

to less than 4  $\mu\text{m}$  thick while our process created a coating greater than 10  $\mu\text{m}$  thick with strong adherence. Thermal expansion mismatch stresses in the competing processes is a problem that does not allow a strong adherence of the diamond coating to the aluminum where as in our process the thin melt layer eliminates this problem. Another area of difficulty for competing processes such as CVD is that they require high substrate temperature ( $>600^\circ\text{C}$ ), which is not suitable for coating aluminum. Most of the competitors have a deposition rate of less than 1  $\mu\text{m/hr}$  while our laser sintering process can coat aluminum at a rate of several micrometers per second. Due to the characteristics of ND/DLC, our coating process provides better solid lubrication, has a better affinity for oil which helps it disperse oil within the motor, and due to the chemical inertness of ND/DLC our coating is more corrosion resistant.

Thus we have been successful in generating a hard and wear resistant coating for lightweight engine components. The success of the process and coating allows us to consider future work that coats the engine components, such as cylinder bores, pistons, and rings, and thereby improve the fuel efficiency. Component testing program including friction, wear life, and abrasive wear life must be performed to understand the robustness and durability of the coating. Future work could also include using the coating on titanium for biomedical implants and other surgical devices where wear on this lightweight metal is of major concern. Here we could coat an implant, and set up a system that represents its normal usage to test the same characteristics as in the engine components. Thus, ND laser sintering technology can go a long way in enhancing the durability and quality of numerous devices.